EFFECT OF PRINTING PARAMETERS ON THE STRUCTURE AND PROPERTIES OF 316L STAINLESS STEEL

KENNETH SESI HUKPATI

A THESIS SUBMITTED TO THE FACULTY OF GRADUATE STUDIES IN PARTIAL FULFILLMENT OF THE REQUIREMENTS FOR THE DEGREE OF MASTER OF APPLIED SCIENCE

GRADUATE PROGRAM IN MECHANICAL ENGINEERING

YORK UNIVERSITY

TORONTO, ONTARIO

SEPTEMBER 2021

Abstract

The emergence of 3D-printing provides the flexibility of 316L stainless steel alloy parts for various structural applications. Although several studies have been done on the effect of parameters on structure and properties, little attention has been paid to the high-strain rate deformation behaviour of this material. Therefore, in the current studies, the effect of printing parameters and the build orientation on the microstructure and high strain rate properties of 3D-printed 316L stainless steel alloy was investigated. In this study, the effect of the individual printing parameters on the boundaries as well as the spatial distribution of sub grains structures were established. There was anisotropy with the high strain rate behaviour, the perpendicular surface exhibited high maximum flow stress with a low strain whereas the parallel surface had lower maximum flow stress with a high strain. For the individual printing parameters, any combination of parameters that gives a finer microstructure showed higher flow stress with a low strain. Also, printing parameter sets that resulted in a coarse structure exhibited lower maximum flow stress and a higher strain. The observations from this study show that the orientation of the process induced pores affect the high strain compressive load of additively manufactured 316L stainless steel.

Acknowledgements

It is a genuine pleasure to express my deep sense of thanks and gratitude to my professors and advisors, Solomon Boakye-Yiadom and Aleksander Czekanski for the opportunity to be part of their research teams. Their dedication and overwhelming support to me are mainly responsible for me completing my work in a tough period. I am also deeply grateful to the Natural Sciences and Engineering Research Council of Canada (NSERC) for the financial support for the lab. I would like to thank my colleagues at the MTAM labs, IDEA labs and York Graduate fellowship for helping and assisting me through my research. I also want to extend my thanks to the Mechanical Department at Lassonde School of Engineering at York University for providing assistance and facilities to carry out my experiments during the pandemic. The lab technicians David Marcinkiewicz, Norman Nicholls and Armando Azevedo in the Mechanical engineering department for the training sessions and support during my experimentations. Finally, I am extremely grateful to my family for their unwavering love, prayers, and support through my stay in Canada.

Table of Contents

List of Figures

List of Tables

List of Abbreviations

Additive Manufacturing – AM

Metal Additive Manufacturing – MAM

Volumetric Energy Density – VED

Laser Powder Bed Fusion – L-PBF

Electron Powder Bed Fusion – E-PBF

Direct Energy Deposition - DED

Laser Engineering Net Shaping – LENS

Electron Beam Free Form Fabrication – EBFFF

Direct Metal Deposition – DMD

Direct Metal Laser Sintering – DMLS

Selective Laser Sintering - SLS

Selective Laser Melting – SLM

Ultrasonic Additive Manufacturing - UAM

Direct Impact Hopkinson Pressure Bar – DIHPB

Split Hopkinson Pressure Bar – SHPB

Scanning Electron Microscope – SEM

1. Introduction

1.1. Background

Metal additive manufacturing (MAM) technology is becoming an increasingly feasible manufacturing technology for more accurate production of metallic parts for use in diversified engineering applications [1]. The appealing potential of Metal Additive Manufacturing (MAM) technology is being adopted by the aerospace industry for the manufacturing of lightweight turbine components such as vane compressor disks, fasteners and compressor blades among many others [2]. MAM is used in the biomedical and medical industry to produce customizable prosthetics, implants and prototypes for surgeries as well as being used in the other transportations fields to increase part safety and fuel efficiency [3],[4]. However, defects and flaws limit the further application of MAM in these industries. The obstacles experienced in these industries are due to the integrity of the final part. Defects such as porosities and residual stresses weaken the load-bearing capacity and facilitate crack formation [3],[5]. Non-equilibrium phase changes by reason of repetitive irregular thermal cycles during manufacturing contributes to the unpredictable material and mechanical properties of final manufactured components [3],[6]. To better understand the high strain rate (HSR) compressive failure mechanisms in MAM parts, a combination of systematic experimental methodologies is required. Post-deformation microstructure characterization and measurements of the microstructure need to be pursued further.

1.2. Problem statement and Research Objective

In this research, the effect of varying print parameters in laser powder bed fusion of metal additive manufacturing (MAM) processes on 316L stainless steel is studied. The aim is to obtain a range of parameters in MAM that can be adopted by manufacturers for various designs and applications. The complete potential of MAM is not fulfilled because there is a lack of general agreement between manufacturers on the production method and design specifications to be used. Optimized parameters within a range can provide superb performance for several applications. However, parts and specified parameters from different printers provide dissimilar mechanical responses [7], [8], [9]. There are over 130 printing parameters in MAM that influence the structure and morphology of the printed part. Some printing parameters found in L-PBF machines include laser spot size, laser power, scan pattern, layer thickness, hatch spacing etc. [10],[11],[12]. Most studies of MAM are being carried out on how printing parameters influence the part microstructure and defects within the produced part. In this study, laser power, scan speed and hatch spacing were the parameters chosen as they require little expertise to alter and can be changed without voiding the warranty of the MAM printer provided by the manufacturer. Most studies of MAM and altering printing parameters have only been carried out by altering the Volumetric Energy Density (VED) and its effect on the tensile mechanical property of the final part. However, there has been little research on the effect of individual parameters on the microstructure and dynamic compressive properties of additively manufactured parts.

There is a need to evaluate the microstructure and mechanical properties in relation to the varying print parameters to validate and specify the range of parameters for adoption in industries. The quality and mechanical properties of additively manufactured parts are highly influenced by the processing parameters applied [7],[13]. MAM parts are currently being produced in intricate metallic shapes and high-performance parts for use in aerospace, automotive and military industries for high stress applications. However, there is a limited used of additively manufactured parts because of limitations in the process, varying performance metrics and lack of standards for the produced parts [13]. Studies have been conducted to determine the effect of printing parameters on the microstructure and tensile properties, however, an extensive comprehension of the microstructural evolution has not been deeply explored. Therefore, the microstructure of MAM parts can be conformed to for high strain rate impact applications when the formation of specific microstructural features is understood. This study aims to determine the relationship between each printing parameter and the microstructural features as well as its effect on the dynamic compressive properties.

To summarise the objective of this study is listed below:

1. Study the effect of individual printing parameters on the microstructure of AM 316L steel

2. Study the effect of individual printing parameters on the high strain rate deformation behaviour of AM 316L stainless steel
3. Study the effect of build orientation (parallel and perpendicular) on the deformation behaviour of AM 316L Stainless steel

1.3. Research Methodology

The process to accomplish the objectives in this study were grouped into three parts. Firstly, we focused on the Laser Powder Bed Fusion (L-PBF) manufacturing method and its extensive use in manufacturing parts. L-PBF technology can be used to construct a highly dense part with properties engineered to meet specific applications. 316L stainless steel the material selected, which is a material actively used in the aerospace, bio-medical, naval and food industries. Also, 316L SS is part of the most accepted materials to be used in 3D printers by many studies. Furthermore, 316L SS has been certified to be used on most 3D printers without needing approval from the manufacturer of the 3D printer and voiding the warranty of the machine. Coupons of 316L were printed using the DMLS M280 equipment and various printing parameters. A relevant number of printing parameters were applied, activating microstructural and morphological changes, and determining the different conditions against high strain rate deformation. The parameters that were varied are hatch spacing, laser power and scan speed to create 49 different combinations of each sample. The densities of the printed coupons were determined using the Archimedes principle. The hardness of the coupons was determined as a function of printing parameters with a Vickers microhardness testing machine. This was followed by an extensive microstructural characterization and measurements to detect the microstructure and morphology of the printed samples as a result of the varied printing parameters. Techniques used in characterization include metallographic techniques such as grinding, polishing, and etching to improve observations under Optical microscopes and Scanning electron microscopes. Coupons were observed and studied with an optical microscope to determine the size and number of pores on two surfaces of the sample. The volume fraction of pores was further determined using the ImageJ software. Through image binarization and thresholding, the pores are analyzed to determine the size, shape, and volume fraction of pores on the sample surfaces. Images from a scanning electron microscope were used to get comprehensive information of the grain structures on the sample surfaces.

Lastly, a Direct Impact Hopkinson Pressure Bar (DIHPB) was used to methodically impact the MAM coupons at a fixed high rate loading condition as a means of mimicking high strain rate impact conditions. Metallographic techniques and microstructural characterization were used to document the deformation modes in the impacted coupons. To reveal the microstructure observed within the pre-impact and post-impact specimens a state of the art Scanning Electron Microscope (SEM) was adopted. These modern techniques and equipment were employed to further capture and understand the evolution of microstructure and mechanism of deformation within this material. This would increase our understanding of the mode of deformation of additively manufactured structural materials and provide the knowledge to modify materials to be resistant to failure during dynamic loading.

1.4. Thesis Organization

This dissertation is structured into six chapters. The following are summaries of the chapters:

- Chapter 1 introduces metal additive manufacturing, the need and applications, the defects and disadvantages and the need for extensive study on its high strain rate failure mechanism to help with improve the design for aerospace applications
- Chapter 2 reviews metal additive manufacturing, the advantages and challenges, and material properties of MAM
- Chapter 3 describes the experimental procedures used in this research. A thorough description of the procedure and equipment used for characterization are presented.
- Chapter 4 provides a comprehensive observation of the microstructure before and after impact
- Chapter 5 discusses the main findings in this study based on the microstructural observations from the specimens

- Chapter 6 presents a summary of the results, conclusion, references, and research contributions

2. Literature Review

2.1. Metal Additive Manufacturing

Manufacturing technologies have advanced due to the high interest in 3D printing technology. The rapid rise of 3D printing technology is attributed to the advantages in the manufacturing processes and the final product. Additive manufacturing technology has advanced from using plastics and polymers to metals and alloys for use in mechanical and load-bearing applications [14]. In the 1980s, a computer-aided design (CAD) model was first printed with plastic and polymeric materials thereby generating interest in 3D printing technology [7]. As significance in 3D printing grew, studies in the 3D printing technology and manufacturing process influenced the industry. As studies in laser printing grew, metal powders replaced polymers and plastics. Manriquez-Fayre and Bourell produced the first metal printed part in 1990 [15]. The Laser Sintering technique later became the most common 3D printing technology to be widely used across the world due to its capabilities and abilities to effortlessly make complex geometries. In the subsequent years, numerous groups developed different 3D printing technologies with different mechanisms. Some of these companies include EOS with the creation of the first commercialized metal 3D printer which uses the Selective Laser Melting technique [7], [16]. In 2000, instead of using laser sintering technique, Arcam AB industries produced another powder bed technology which uses an electron beam as the source of heat [7], [17]. 3D printing technology, as a result, has gained the necessary attention over the years and has taken the engineering industry by storm. This has empowered manufacturers to develop innovative ideas which have made the production of materials more reliable, faster, and easier.

Many industries have incorporated 3D printing technology since its inception in the 1990's. Demand has grown due to some of the significant benefits that 3D printing technology offers. Comparing the production process of 3D printing to the traditional manufacturing method, it offers a wide range of significant benefits. As a result, this technology has enabled manufacturers to produce wide range of materials as it presents better mechanical properties. Military, dental, medical, and naval industries incorporate 3D printing for rapid prototyping in use as it eliminates the need for tools. Additionally, increased production rate, short lead times, cost effectiveness, improved quality of products are some advantages to these industries [18]. 3D printing cannot totally replace subtractive manufacturing methods because of the length of period it takes to produce in large quantities. It can however be used for customization and in niche markets. Customization can easily be achieved as designs can be shared, altered, and modified. 3D printed parts have reduced cost due to less material usage in the production process and has improved efficiency and performance. Therefore, has a significant impact on the environment [7]. For example, Airbus A350 brackets had less weight due to the of 3D printing process used in manufacturing its complex shape [5], [7]. 3D printing has a rapid change from the product development stage to the manufacture of end products stage thereby reducing the production time. Successfully printing useful parts for defense and military application will be favorable [7], [19]. Implants in the orthopedic industries are getting more customizable to patients needs thereby making work easier for patients and doctors alike.

There has been an evolution in 3D printing technology in the sense that, it has tremendously changed the old ways of producing materials or objects over the half a century, which has made manufacturing more effective and efficient. It is therefore defined as the technology that builds objects by adding layer upon layer of materials [20]. The most used feedstock material in 3D printing is in the form of powder or wire. The powder or wire is fed into the printer, melted, and cooled layer by layer to form a specifically shaped object [5]. The use of 3D printing technology can be beneficial to both individuals and businesses across the world. Some of these enormous benefits include the time reduction for initial product development, the cost-effectiveness of the initial process, the reduction of human risk, creative design freedom, the possibility of infinite shapes and geometry, and faster design to production integration and as a result has been widely adopted in various industries such as the aerospace, biomedical, automotive, manufacturing, robotics, and educational industries to develop products that were previously not easy manufacturable [5], [21], [22].

2.2. Types of 3D printing

Various MAM technologies are constantly being accepted in research and industry based on the method of bonding and material in use. Powder bed fusion (PBF) and Direct Energy Deposition (DED) are the two main types MAM technology currently being easily embraced [5], [23]. DED printing technique works by fusing the powder/wire feedstock when being deposited. Laser Engineering Net Shaping (LENS), Electron Beam Free Form Fabrication (EBFFF) and Direct Metal Deposition (DMD) use either Laser, Electron or Arc heat/energy source and are the most common DED techniques. LENS, the most examined type of DED printing works by depositing molten metal parts to build a 3D object after each layer cools. This method of printing occurs in an argon gas chamber to prevent oxidation or purge trapped oxygen.

2.2.1. Directed Energy Deposition (DED)

Direct Energy Deposition (DED) involves a pointed source of energy which has been established in previous techniques as a laser, electron beam, plasma, or arc. Metallic powders are melted from a wire being pumped or pushed from a nozzle, using the source of energy [8]. A schematic diagram in Figure [2-1], illustrating the set-up of a typical DED system has been shown. The laser power is always regulated by a controller where CAD drawing is also fed into. The controller also provides options for setting printing parameters which may include beam diameters and scanning power during the process.

DED technology has greater all-encompassing advantage like higher density, defect-free structure, greater reliability, and superior mechanical characteristics with respect to the products which are produced, regardless of better-manufacturing flexibility in PBF technologies. The principle behind this procedure emanates from the process used for welding. The metal can be sintered outside a build chamber or controlled environment by streaming a shielding gas over the melt pool to prevent or reaction with air which helps maintain its mechanical strength. The most common type of mechanism used in DED systems is a laser source and a powder fed feedstock. Sandia National Laboratories created the first setup and patented this as the first LENS process [24]. Presently, multipass welding processing is being explored for the DED process because it has the ability to create and fabricate components with large spatial arrangements and makes use of lower heat input values. However, a high percentage of pores are produced in the sample [25]. The setup of the DED system has a nozzle connected with the powder feeder and a gas supply system to slowly distribute the powders at a regulated deposition rate on the workpiece. The controller is connected to the laser head and CNC platform. The controller regulates the laser energy released and the position of the CNC platform. Powder hoppers must be brought to capacity and the powders are supplied to the nozzle. In order to develop and build complex shape, a rotary 5-axis stage or a stationary 3-axis build system can be used to position the substrate. The substrate is used in a sealed chamber to cancel any interaction with the environment when working.

To increase resistance to oxidation a shielding gas is aimed at the melt pool during the printing process although noble gases are not automatically required. However, the printing chamber is filled with either Nitrogen or Argon when printing reactive metals such as Titanium. Post-processing methods are used to clear away attached substrate and relieve residual stresses thereby, improving the mechanical properties of the 3D printed part. Further research conducted on mechanical properties of DED methods presented 3 types of crack initiation during fatigue tests [26], [27]. Experiments were conducted on DED printed titanium alloy and results presented cracks initiating from inner pores, internal lack of fusion discontinuities initiating cracks as well as external surface-initiated cracks. With the advancement in DED and Hot Isostatic Pressing (HIP), technology porosity and lack of fusion defects will reduce substantially. However, pores can not be eliminated and is the main factor in the mechanical performance of a DED printed metal.

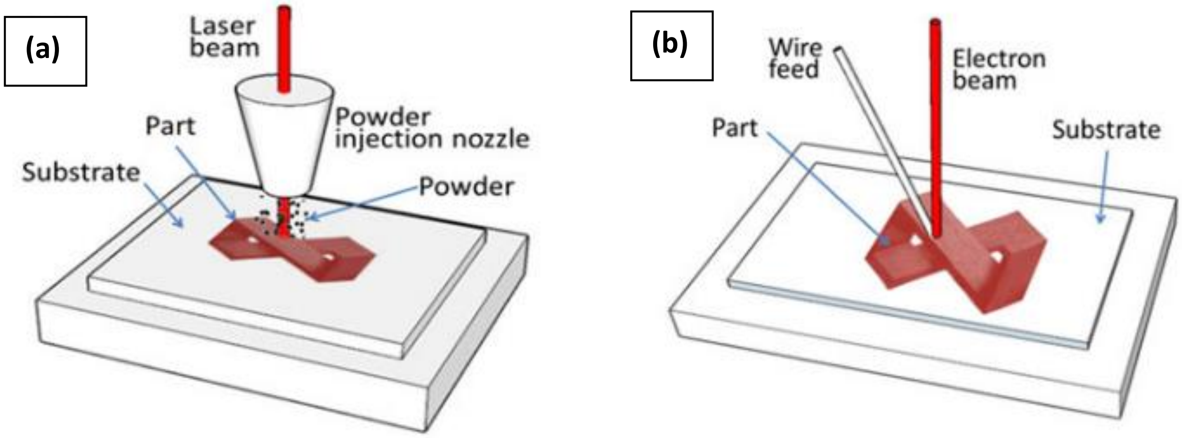

Figure 2-1. Schematic of (a) powder-fed DED process; (b) wire-fed DED process[28]

2.2.2. Powder Bed Fusion (PBF)

There are two types of PBF techniques being used. These are differentiated by the heat source applied. The heat source for the PBF technique is either Electron Beam (E-PBF) or laser (L-PBF) along with a powder bed feedstock material [29]. Laser sourced techniques such as Direct Metal Laser Sintering (DMLS), Selective Laser Sintering (SLS) and Selective Laser Melting (SLM) are popular in the industry. In DMLS, the laser sinters the powders directly without using a binding agent for particle merger. Whereas the SLS technique adopts the use of a binding agent and achieves mixture by heating the particles to half their melting temperature. SLM technique, on the other hand, heats the material to its melting point to obtain a liquid pool. SLS and SLM techniques are noted for their different consolidation methods. SLM employs liquid state fusion at high temperatures whilst SLS employs solid-state fusion at lower temperatures.

Electron Beam (E-PBF) also known as EBM uses high energy electrons in preference to a laser beam. The powder bed material is completely melted by the high heat generated from the high energy electron beam [15]. Contrary to most L-PBF methods, EBM generates and positions the electrons from filaments and a collimator respectively, concealed in column [15]. However, like L-PBF techniques, a focused energy source (electron beam gun), powder hoppers and powder rake transfer and disperse the powder across the powder bed [30]. A vacuum-sealed chamber is used to inhibit oxidation whilst the 60KV electron beam melts the powder. EBM technology has been tagged as a major manufacturing tool in outer space as it can be used to create functional and replacement parts [7]. Printing parameters such as scan speed, pattern, laser parameters affect the printing process and product. Figure [2-2] presents the schematic of L-PBF and E-PBF printing process.

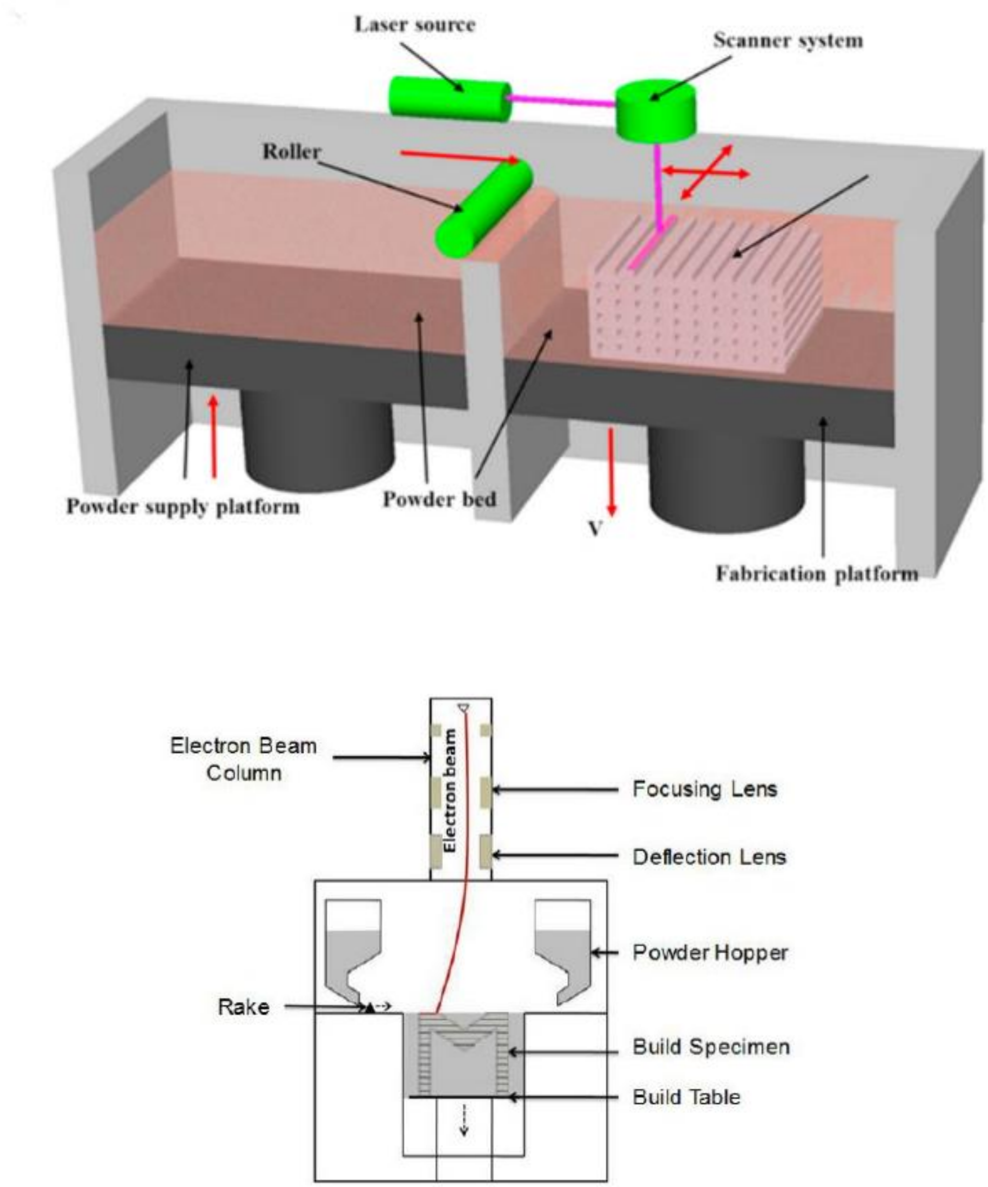

Figure 2-2. Schmematic of PBF a) L-PBF b) EBM, i.e E-PBF process[31]

2.2.3. Sheet Lamination

Sheet Lamination techniques work by stacking 2D sheets into 3D objects. Brazing, diffusion bonding, welding and ultrasonic strengthening are used in sheet lamination technique to pile and assemble 2D metal sheets into 3D objects [26]. Sheet lamination adopts the techniques used in laser beam and electric resistance welding. Dimensions of the sheets used in sheet lamination process are cut into the sheet before being consolidated or are machined into the 3D printed object [15]. Due to this flexibility, sheet lamination has numerous advantages such as: improved surface finishes, low build costs and great geometric consistency. However, due to the build method anisotropic behavior in the 3D printed object is expected. Higher strength is observed in the stacking direction with reduced strength in the perpendicular direction. A flux is created and acts as a brazing alloy between the 2 joining sheets. Brazing is carried out successfully by coating the sheet with flux and serves as a brazing alloy between the joining sheets [15]. For sheets to stick together appendages are used to generate the resistive force needed when using the resistance welding method. Additionally, different methods of adhering sheet metal are being examined in research to create a tougher joining process. The current joining process is not tough enough. This limitation produced the Ultrasonic Additive Manufacturing (UAM) process as the frequent method for joining [27], [32]. The schematic for Sheet Lamination process is shown in Figure [2-3].

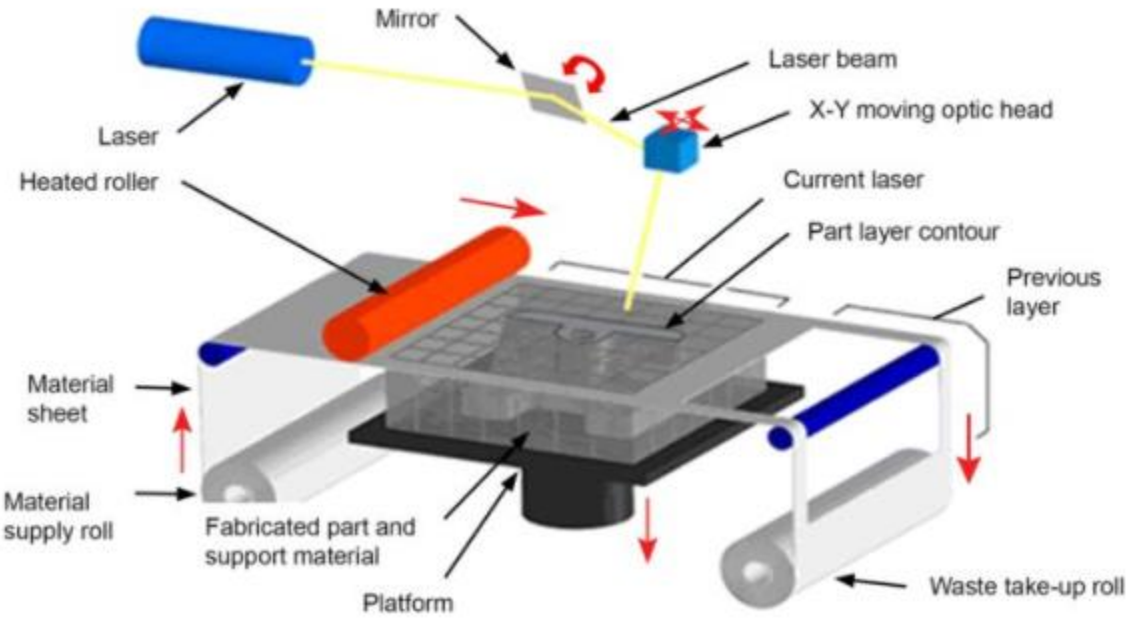

Figure 2-3. Schematic of sheet lamination process[33]

2.3. Advantages of MAM

As a new and disruptive manufacturing method, MAM has many advantages over the conventional manufacturing methods. The reduction in manufacturing lead times beginning from initial design to the creation of the final part is one of the many advantages of MAM. As a result, it has a faster changeover from the design stage to production stage. Time and resources are saved by altering the instrumentation process and mold creation process in the manufacturing chain. Another advantage is, no machining, milling, or tooling is required to manufacture the parts. However, after processing, the support structures used when printing must be detached. In addition, in conventional manufacturing the mold can take up to 60 days to manufacture whereas with MAM the mold can be made within three days to begin the process of injection molding. Thus, MAM technology reduces lead time for the manufacturing process when compared to conventional manufacturing processes [34]. In addition to the previous advantages, MAM aids in reducing the workload for designers, engineers, and manufacturers. MAM technology can be used any complex and exceptional design with little to no constraint on production method. Conventionally, many complex design ideas are altered and eventually changed completely due to manufacturing limitations. However, with MAM the CAD file can be altered and fed to the machine and printed with no additional costs.

Furthermore, materials use in MAM technology are greatly reduced. The product is formed by adding materials in a layer by layer order whereas, in conventional manufacturing the raw solid material is carved and sculpted to obtain the required shape. As a result, MAM uses limited resources in production while conventional methods use a larger number of resources that become waste material. In the printing method, layers as little as 5μm are used in producing the part to reduce the amount of waste material from the production. This is significant for the aerospace, biomedical and automotive industries as they get to produce parts that get the exact fit. Additionally, the automotive and aerospace industries can use this manufacturing method to produce light weight parts by reducing the total mass of the final part. The production of light weight parts is being approved in research and industry to aid in reducing the carbon released into the atmosphere by vehicles and aircrafts. MAM can be used to produce lightweight parts by manufacturing parts with 75% less of the original mass of product created by conventional methods. Also, manufacturing parts with low density and good mechanical properties are possible with MAM technology. With all the factors mentioned above it is true to say that MAM is a manufacturing process that can be very resource efficient and useful for many industries.

Ultimately, MAM printers have been adopted on the International Space Station (ISS) to produce and replace broken parts as well as tools. The maintenance of these complex parts can be expensive using conventional manufacturing. Using conventional manufacturing methods, these parts are manufactured on earth and transported to the ISS which is costly. Hence, the broken parts can be manufactured and replaced on the ISS without a new space mission happening. This idea can also be applied in industries to replace parts of machines. Economists have estimated the global value of the AM industry to reach over $10 billion by 2022. This has fueled governments and investors to fund research projects to further advance and improve the technology.

2.4. Disadvantages of MAM

Although the benefits of 3D printing are significant to industries, there are also some challenges that needs consideration. The challenges faced in 3D printing affects the manufacturing of parts. Hindrances such as porosity, non-equilibrium phase, residual stresses and defects from printing parameters can be found in 3D printed parts. These defects affect the load bearing capacity of the final printed parts. Studies on 3D printing have shown that scanning speed, laser spot size, layer thickness, scan patterns and laser power influence the microstructural integrity of the final product parts [10], [12], [35]. The microstructure of 3D printed samples differs from samples produced by traditional manufacturing methods. The mechanical properties of 3D printed parts are different from the known or recorded properties of traditionally manufactured parts of products. Cracks originate within 3D printed samples as a result of high residual stresses. Residual stresses are caused by high thermal gradients and high thermal stresses within the sample thereby reducing the structural integrity and increasing chance of failure [36], [37]. A further description of the challenges and limitations of MAM are as follows:

2.4.1. Porosity

Porosity is a major drawback in the final manufactured products of MAM. Porosity occurs due to lack of fusion of the metal powder during the process or as a form of trapped gas not being able to escape because of solidification. These voids in most scenarios have negative effect on the mechanical and load bearing capacity of metal parts. Porosities occur due to the reduced bonding between subsequent layers, the processing parameters used, the condition of powder, the melting and the cooling features of the metal in question and the conditions of the chamber [38], [39]. Figure [2-4] show pores in parts printed with MAM technology. Furthermore, atomisation occurs during the printing process and can result in gas entrapment occurring within the build layers. These trapped gasses stay in the parts during solidification to form spherical gas pores. According to literature, the main causes of porosity are the printing parameters employed. The pores formed by altering parameters such as laser speed, laser power etc. are known as process-induced pores. The effect of powder unification on the powder bed supplement the production of process induced pores [40]. These process-induced pores occur when metal particles larger than the layer thickness are included on the powder bed thereby affecting the consolidation of the particles. When the laser power or energy is too low to induce total melting, spatter ejection occurs. Spatter ejection results in non-spherical pores and keyhole formation of various sizes. Printing the whole material with high power can create a stream of pores and voids. To restrict the effect of spatter or keyhole formation, parameters will have to altered during the printing process. In addition, lack of fusion pores appear during the processing when a reduced amount of powder is provided on the spot and are determined by un-melted powder particles around the pore. Lastly, hot tearing is observed in the final printed part. Hot tearing develops when the molten metal flows imperfectly into a chosen region. This type of porosity is known as the shrinkage porosity [20].

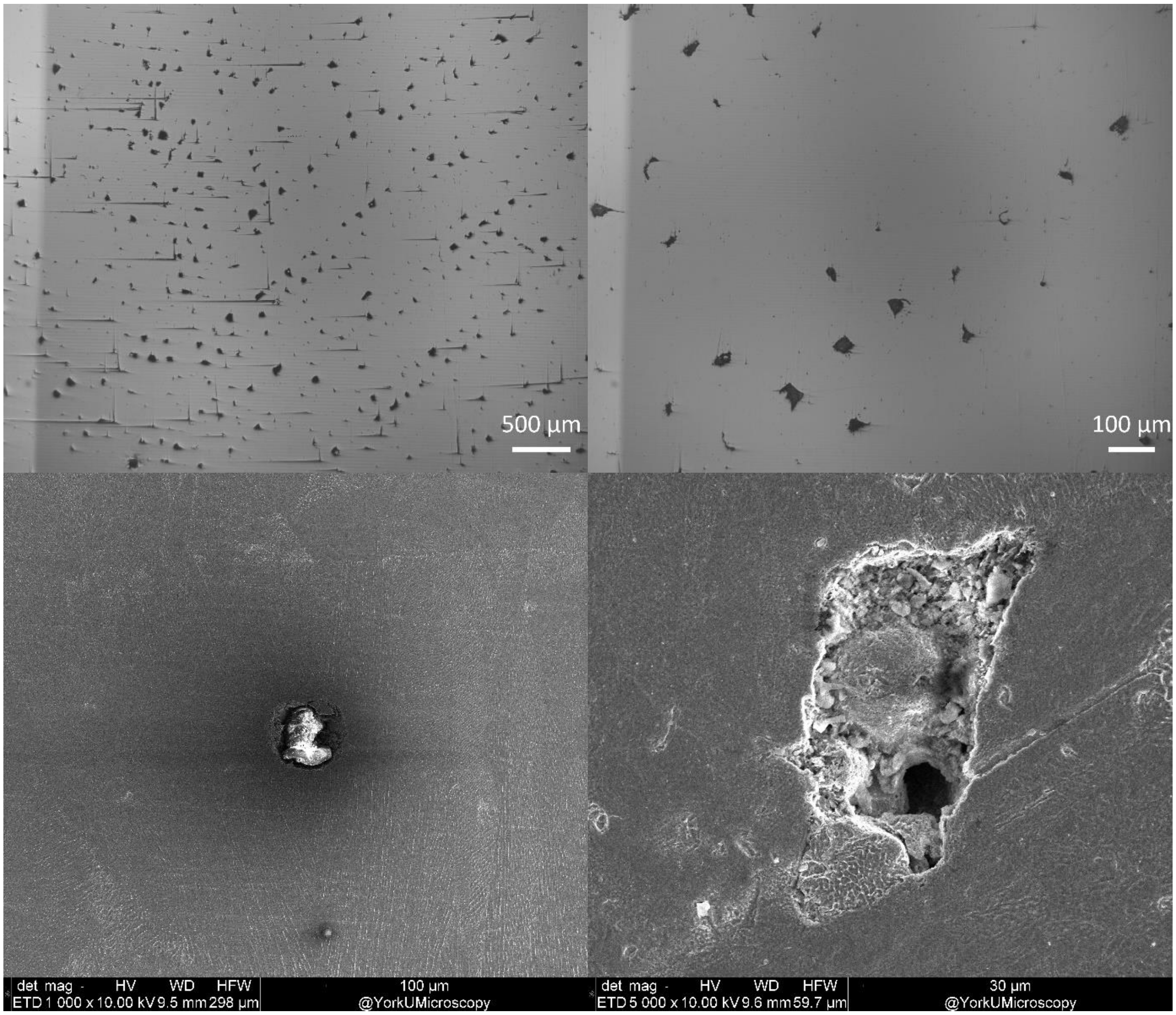

Figure 2-4. Porosities in a MAM part

2.4.2. Residual Stresses

Residual stresses are a common defect observed in MAM parts. It has been demonstrated by several publications that residual stresses are generated from the variable heating, melting, and cooling observed in the material and printing chamber during the printing process. Residual stresses are described as the stresses residing within the printed part after a temperature balance is achieved in the environment. Residual stresses are categorized as Type I, Type II and Type III according to Liu et al [41]. Type I residual stresses occur on a large scale and are characteristics of the shape, orientation, and size of the printed product. Type II and Type III residual stresses occur on a microscale and nanoscale, respectively. Type II residual stresses arise due to anisotropy in material on the grain scale whilst Type III residual stresses develop due to the dislocations present [42]. Further, Type II and Type III residual stresses are more challenging to measure and minimally affect the mechanical properties of the produced part. However, residual stresses influence crack propagation, distortion of the printed part as well as delamination between the layers. These stresses affect the time used in part production, material waste, constant design changes and energy usage. The length of the printed part must be altered as residual stress will lead to warping and delamination if the part is very long.

As stated earlier, residual stresses are generated by the temperature-gradient mechanism. An example is the stresses that are generated between the layers of the material. As the laser interacts with the final layer, heat is concentrated and built around the beam thereby creating a high temperature gradient between the interacting spot and the surrounding areas of the material. As a result, the material loses strength during the printing process. Furthermore, elastic compressive strains occur as the extent of expansion possible is further limited between the layers. Induced plastic compression known as residual stresses arise. In addition, the cooling rate is observed as the second system of inducing residual stresses. Residual stresses have been detected in all MAM samples and is difficult to eradicate. However, much of recent literature is focusing on reducing the amount of residual stresses developed to limit its influence on failure. According to Levy et al [26], residual stresses can be reduced or relieved by heat treating the samples after the printing procedure. They further suggested reducing the temperature gradient within the material by increasing the temperature of the print chamber. Another suggestion was to print support structures to allow for even temperature distribution and dissipation in the material and prevent failure.

A considerable amount of literature has been published on relieving residual stresses in MAM products [43], [44]. Experimental methods and finite element models have been suggested to measure and lower residual stresses. Altering the printing parameters have been suggested to influence the laser power and reduce the residual stresses. According to Wu et al, centralized residual stresses are compressive whereas tensile stresses are observed towards the surfaces in SLM produced 316 stainless steel [43]. Furthermore, Kruth et al, [44] investigated the effect of printing systems on distortion. They deduced that the island/chessboard scanning strategy reduced distortion compared to other scanning designs. It was further concluded that a smaller island size as well as an increased energy density will produce a material with a lower residual stress. Several studies further exhibited a tensile stress along the scan direction in small-scale samples when using the X-ray diffraction residual stress measurement [45].

2.4.3. Non-Equilibrium Microstructures

MAM changes the microstructure when it is used to fabricate parts as compared to structures manufactured with traditional technologies. These microstructural changes are observed in MAM of steel components. New phases and segregation of particles are detected in MAM produced steel parts. However, with the same chemical composition, traditional methods do not produce segregated phases and microstructures. Microstructures formed from MAM technique have different properties as recorded from the traditional manufacturing technology. One alloy which is most researched for MAM parts fabrications is Steel. All other metals and alloys used in AM experience the same microstructural differences. As a result of the manufacturing process, AM process incorporates a high cooling rate which induces fine and grainy structures [5], [28]. Changes in temperatures during manufacturing can cause alteration in the microstructure. Super-structures are observed on the melt pool boundaries, secondary phases in addition to cellular and lath sub-structures [46]. Furthermore, anisotropic characteristics as well as texture has been recorded in MAM parts due the specific orientation of grains and particles. The parameters that were used in the fabrication processes causes the texture to develop [47]. In many MAM types, wide microstructures are determined by the slow cooling rates which produce thick melt pool boundaries. These are observed in studies into LMD technologies [5], [28]. Figure [2-5] depicts non-equilibrium phases in 3d printed materials.

Some alloying metals to undergo phase transformations during the MAM process due to the ongoing temperature changes. This gradual switch modifies the characteristics and properties of the microstructure entirely from its initial features. However, different types of AM techniques alter the microstructure of the fabricated part. As studied by Zietala et al, [25] fabricating 316L parts from LENS technology produced intercellular ferrites on the boundaries of the cellular structures. Furthermore, in SLM technique, a second phase microstructure is observed in single phase austenitic steel structures which alter the performance of the material [48]. Studies have shown that 304L and 316L steels contain lath and cellular dendritic structures based on the type of MAM technique used and the chemical composition [49], [50], [51], [52]. The low content of the carbon reduces the formation of precipitated carbide. The precipitated carbides are therefore not common in the final part. Ferrites are produced in martensitic steels and precipitation hardening steels such as maraging steel after they have been additively manufactured.

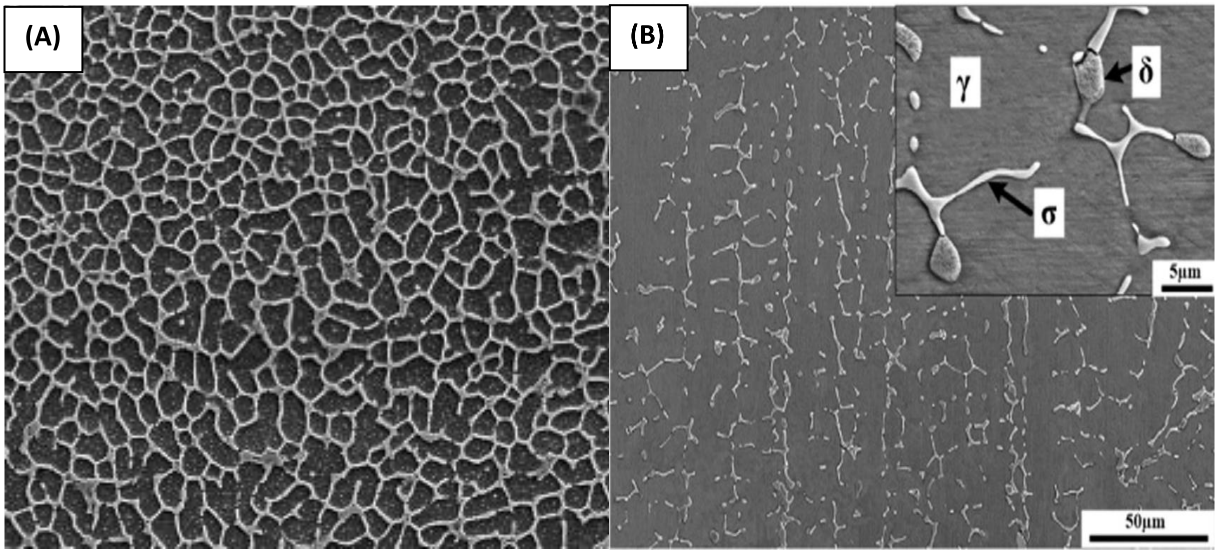

Figure 2-5 SEM depicting non-equilibrium phases (a)nSLM manufactured aluminium alloy[53] (b) Arc manufactured 316l SS alloy[54]

2.5. Printing Parameters

Manufacturing technologies have advanced due to the high interest in 3D printing technology. Some advantages are attributed to the rapid rise of 3D printing technology. 3D printing is a layer by layer additive process of manufacturing objects. A 3D CAD generated drawing is divided into distinct layers of predetermined thickness (t/m) and fed into a 3d printer. The metal powder is deposited on to a build platform at an equal thickness (t/m) as the layers of the CAD drawing. A laser or energy beam at a specified power (P/W) and constant travel speed (v/mms^{-1}) melts the powder on the platform into the desired shape or cross-section. Multiple scans are done per layer depending on the scan strategy with the distance between scan lines referred to as the hatch spacing (h/m). After melting the cross-section, the platform lowers by the specified layer thickness (t/m) and the process is repeated until a complete component is printed. Despite the easy manufacturing method of 3D printing, several discontinuities are realised in the final product. Some such defects include various types of pores, microcracks, residual stresses and denudation [4], [23], [55]. These defects are results of the various factors.

The final 3D printed specimen is dependent on various parameters. Alloying elements, Laser power, laser speed/travel speed, Layer thickness, hatch spacing etc. are parameters that have influence on the microstructure and properties of completed component as shown in Figure [2-6]. Laser power, laser speed, layer thickness and hatch spacing are four major variables in 3D printers during the manufacturing process. These parameters are the easiest to manipulate as well as easiest to determine the final influence on the microstructure. Volumetric energy density is an expression linking these four important printing parameters to classify or evaluate volumetric effects [56]. Volumetric energy density(E) is a function of these parameters and is expressed as:

$$E = \frac{P}{hvt} \ldots\ldots\ldots\ldots\ldots\ldots\ldots\ldots\ldots\ldots\ldots\ldots\ldots\ldots\ldots\ldots\ldots\ldots\ldots\ldots\ldots\ldots\ldots\ldots\ldots\ldots\ldots\ldots\ldots\ldots\ldots\ldots\ldots.(1)$$

Where P is the laser power in watts, h is the hatch spacing in mm, v is the travel speed of the laser in mm/s and t is the layer thickness in mm [44].

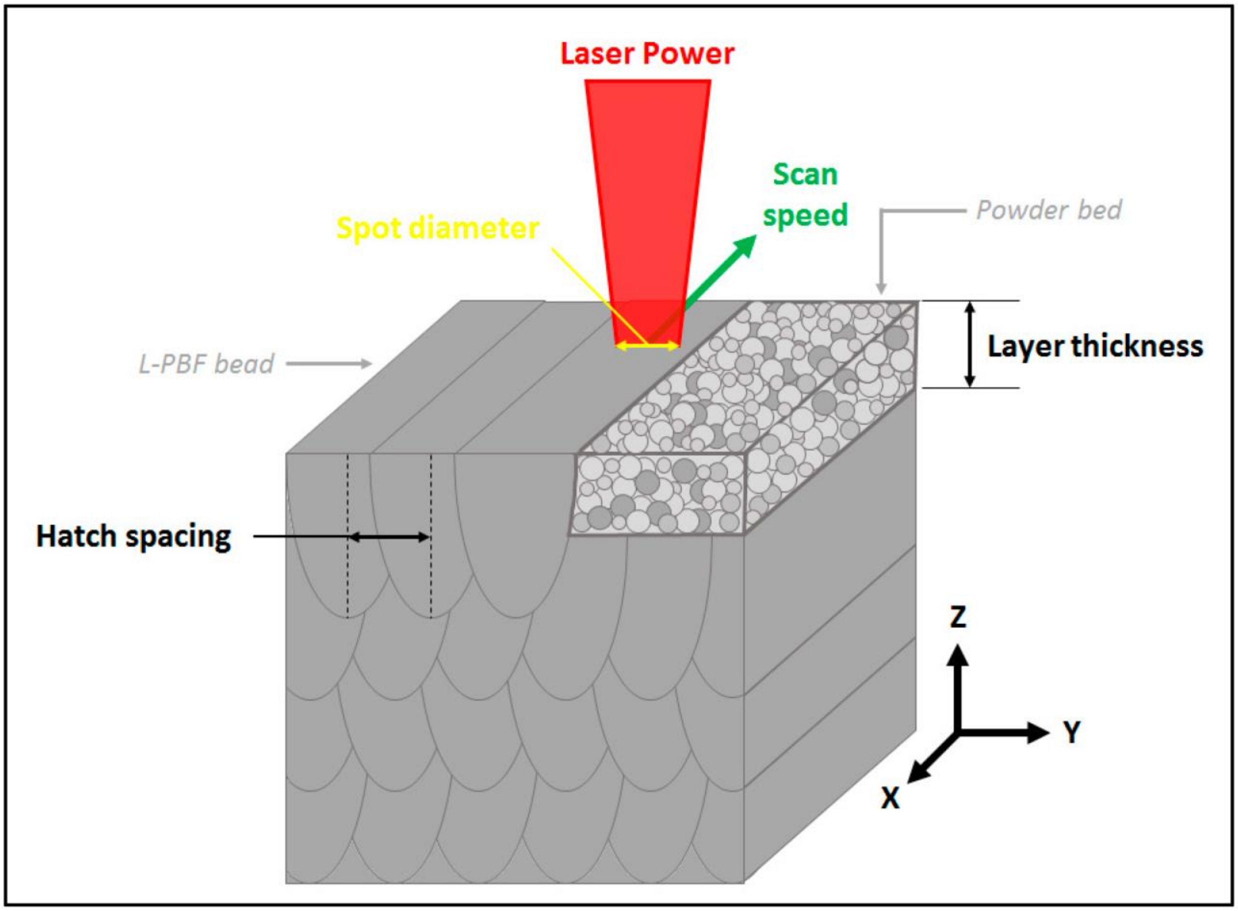

Figure 2-6. Schematic of manufacturing parameters of Laser -Powder Bed Fusion[57]

2.5.1. Laser power

Energy density or specific energy is defined as the energy within a region per unit volume of the system. Therefore, the laser power influences the energy density within a system. Whilst all other parameters are fixed, an increase in laser power, will result in heat build-up within the material. With high enough laser power, the metal can reach boiling temperatures within the melt pool. A high surface tension gradient will form and result in spatter and denudation [58]. Due to the high temperatures realised at the contact point between the laser and the material, a high metal vapor pressure is formed on the molten metal and forces the material out of the way thereby creating keyholes with high aspect ratios [58]. The molten metal tries to fill the pore created after being melted again when the laser passes [59].

Kamath et al, [10] investigated the density of AM 316L parts after altering the laser power. After varying the laser power between 150W – 400W, insufficient melting was caused by the increase in speed with a decrease in laser power. At higher laser power, density was lessened due to the formation of keyholes [10]. Yakout et al, [60] recommended a reliable energy density range between 62.5 - 104.2 J/mm^3 in their study of mechanical behaviour and densification of 316L stainless steel alloy at 200W laser power. Better densification and minimal defects and voids are observed in the AM 316L samples as reported by Yakout et al.

2.5.2. Laser speed

Laser speed impacts the energy density of the completed part. Heat input is reduced or increased depending on the speed of travel of the laser. Reducing the amount of time used to build is possible by increasing the laser travel speed. Increasing the travel speed will result in loss of heat input per area therefore producing voids and un-melted particles [61]. These voids and un-melted particles are products of little laser to material interaction and heat input interaction [61]. According to Qiu et al, [62] the scanned tracks indicate melt flow during melting, suggesting unstable flow at high laser scanning speed. In laser arc welding, stress concentrators are formed from long and narrow melt pools when travel speed is increased [63]. The layers of the material are also affected by a change in the laser travel speed. An increase in laser speed reduces the depth of penetration and reduces the bonding between the previous layer and the current layer [63]. On the other hand, reducing the travel speed decreases the amount of porosity within the sample. Reducing the porosity in the sample will lead to an increase microhardness values but further reducing the travel speed will reduce the microhardness of the sample [64].

According to Qiu et al, [62] , travel speeds below 2700mm/s produce parts with low porosity but had a less significant increase in porosity percentage when speeds were increased to 4250mm/s. They further went on to investigate the effect of travel speed on the surface roughness of printed parts. Evenly parallel lines with regular overlapping were realised at speeds of 2300mm/s whilst irregular shapes and overhangs on the previous layers (resulting in cave-like pores) were realised in the scan tracks at 3500mm/s [62]. It was further concluded the cave-like pores were developed by the unstable melt flow moving away from the laser scan direction and bonding with the prior layer with gas trapped underneath thereby creating a gap [62]. Kamath et al, [10] discovered a relation between laser power intensity and speed sensitivity. Due to the dependency of speed sensitivity on the laser power, there is an insignificant disparity in density of the final part when a high laser power is used with varying travel speeds [10]. Kamath et al, [10] further observed similar densification at high laser power and different scan speeds but a high variation in density at lower laser power at varying scan speeds.

2.5.3. Hatch spacing

Hatch spacing is the distance between the center of two parallel scan tracks. The number of scan lines will lessen for the final product as well as a lower heat input is expected with higher hatch spacing. Heat transfer between melt lines is much less for high hatch spacing thereby leading to incomplete and inadequate bonding between scan lines. As a result, a high percentage of pores are evident in samples printed with high hatch spaces. On the other hand, low hatch spacing results in vertical cracking in the sample due to high thermal stresses [44].

At low hatch spacing, melt pools experience re-melting due to the laser passing over. Rescanning is another parameter that affects the final microstructure and defects in a 3d printed part. Rescanning is known to drastically reduce the porosity within a the part as well as relieve residual stress in one scan [59]. On the other hand, rescanning on multiple occasions significantly drops the density of the part by increasing the porosity in the material [59].

2.5.4. Layer thickness

Thick powder beds or powder layers are more difficultly controlled when compared to the first three parameters due to the powder sizes. However, the layer thickness influences the energy density of the part. The size of the layer determines the amount of energy required to melt the layer. Thin layer thickness will require less energy per unit area whilst a thick layer will require more energy to ensure complete melting of the powder. In high layer thickness, more gases are trapped between the particles and travel longer distances to escape. Hence the gases unable to escape the molten metal before hardening become pores. Therefore, porosity becomes more likely with high layer thickness [63]. Heat and mass transfer are also influenced by layer thickness [63]. The schematic of varying layer thickness is shown in Figure [2-7].

Qiu et al [62], in their study discovered an accelerated drop in density as porosity increases with a layer thickness above 60µm. The pores are irregularly shaped and more elongated with no presence of un-melted or partially melted powders [62]. Whereby, at layer thickness below 60µm, the scan tracks become aligned with the lower layer thickness exhibiting a stable melt flow according to Qiu et al, [62]. This displayed a correlation between the top surface roughness of each and the layer thickness. The surface roughness of each layer increases with an increase in layer thickness [62].

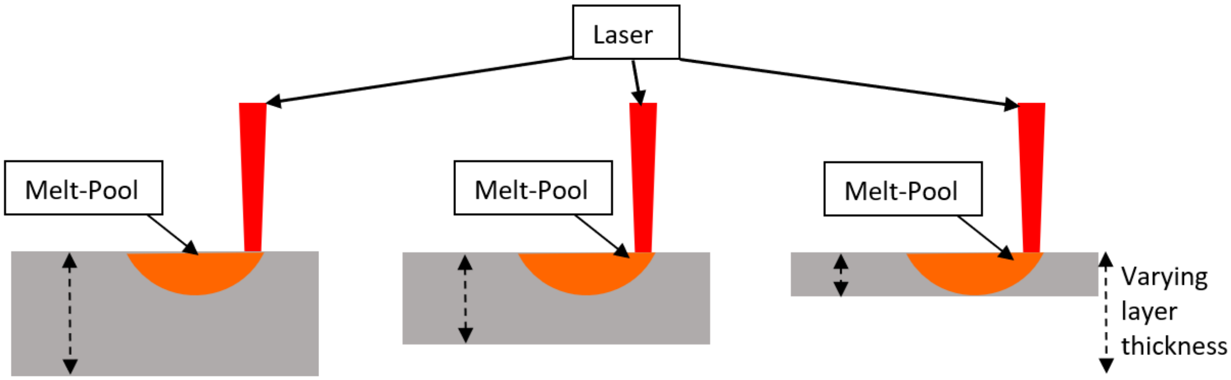

Figure 2-7. Schematic of varying laser thickness

2.5.5. 316L Stainless Steel Alloy

According to the American iron and steel institute, 316L is a low carbon austenitic variation of stainless steel [65]. The low carbon percentage as well as the inclusion of molybdenum in 316L stainless steel give its attractive corrosion resistant performance in hostile environments [65]. Additive manufacturing, welding, and cladding are possible due to the chemical composition which aid in reducing sensitization within the material. In addition, exceptional machinability, favorable ductility, toughness, and weldability are displayed by this material at cryogenic temperatures despite having a propensity to work harden [66], [67]. At elevated temperatures; tensile strength, stress to rupture and creep are higher compared to other chromium-nickel stainless steels is significantly better [65]. As a result of its properties, 316L stainless steel is used in an extensive range of applications; from the marine industry to food industry, medical industry in the form of implants, transportation industry in cars and airplanes as well as being used in onshore and offshore construction industries. 316L stainless steel has a chemical composition consisting of Carbon (C), Manganese (Mn), Silicon (Si), Phosphorus (P), Sulphur (S), Chromium (Cr), Nickel (Ni), Nitrogen (N), Molybdenum (Mo) and Iron (Fe) at varying percentages as shown in Table 1.

The material features of 316L are determined by the different phases, defects, and dislocations. Alloying elements as well as solidification circumstances and post processing treatments determine the structural arrangement at room temperature [68]. Cooling rate, temperature and alloying elements easily affect the phase transformation in austenitic steels. Unlike ferritic steels, austenitic steels do not experience ductile to brittle transition, which cause detrimental effects in ferritic steels [69]. The ferritic transformation is minimized and possibly stopped completely due to the high number of alloys [70]. The austenitic face centered cubic structure is observed at room temperature [70]. However, the formation of ferrite is heightened by the addition of chromium to a pure carbon steel [69]. The addition of nickel to chromium and carbon steel impedes the transformation of austenite to ferrite whilst promoting the corrosive properties of 316L steel [70]. Corrosive properties of 316L are further bolstered by the addition of molybdenum [70].

2.5.6. Influence of alloying elements

All the elements in 316L influence the structure and properties in a specific manner. 316L stainless steel is made of Carbon, Manganese, Silicon, Phosphorus, sulphur, Chromium, Nickel, Nitrogen, Molybdenum, and Iron. Each element has its specific effect on the microstructure and properties of 316L stainless steel. Carbon replaces an iron molecule in the lattice structure. It is also placed in an interstitial position to further improve the strength and hardness of the material. Forged 316L stainless steel has a hardness value of 155V [70]. Manganese is added to 316L for 3 main reasons. These reasons are to provide a stable austenitic structure at lower temperatures, improve ductility at higher temperatures and heighten the solubility of nitrogen within the material. Silicon on the other hand, inhibits the additional unification of carbon (carburising) at higher temperatures whilst increasing the resistance to oxidation. Silicon also aids in the formation of ferrites. Phosphorus and Sulphur added in small amounts enhances the ability to machine the material. However, phosphorus and sulphur reduce the materials resistance to corrosion and the weldability when added in large amounts. Phosphorus further boosts the formation of cracks during welding [70]. On the contrary, Chromium forms a stable oxide layer on the material surface thereby improving the materials resistance to corrosion. Chromium is also a ferrite stabilizer [69], [71]. Nickel helps make the surface of the material less chemically reactive thereby regulating the pitting resistance [72], [73]. Ductility is improved thus improving toughness as well as the formation of austenite with nickel in the material. However, a higher susceptibility to stress corrosion cracking is possible with 10-14% of nickel [70], [73], [74]. Likewise, nitrogen and molybdenum reduce the susceptibility of pitting corrosion within the material. Nitrogen also develops the formation of austenite [70]. As mentioned earlier, molybdenum enhances the resistance to pitting and crevice corrosion [70], [73]. Molybdenum improves the formation of ferrites as well as increasing the mechanical strength of the material [73]. The influence of each alloying element is summarised in Table 1.

Carbon is rejected from the solution when the material is kept within a temperature range of 500-800℃ for extended periods. The rejected carbon are primarily found near the grain boundaries and easily bond with neighbouring metals to form carbides on the boundaries [70]. Due to the repeated heat cycle and layer by layer binding used in 3D printing, the chromium metals bond with the carbon to create $Cr_{23}C_6$ carbides [70]. As a result of the large amounts of chromium bonding with a single carbon molecule, the material becomes susceptible to intergranular corrosive attacks because the corrosive resistance in those regions drops [70], [52].

Table 1: influence of alloying elements of 316l stainless steel

Alloys	**Min.[wt%]**	**Max.[wt%]**	**Effect**
C	-	0.03	Improves the strength and hardness of the alloy
Mn	-	2.00	Provide a stable austenitic structure at lower temperatures, improve ductility at higher temperatures and heighten the solubility of nitrogen within the 316L stainless steel
Si	-	0.75	Helps in the formation of ferrites as well as inhibiting carburising at higher temperatures whilst increasing the resistance to oxidation
P	-	0.045	Enhances the ability to machine the material
S	-	0.03	Enhances the ability to machine the material
Cr	16.00	18.00	Stabilizes ferrite formation whilst improving corrosion resistance of 316L stainless steel
Ni	10.00	14.00	Aids the formation of austenite whilst also improving ductility and toughness
N	-	0.10	Develops the formation of austenite
Mo	2.00	3.00	Improves the formation of ferrites whilst increasing the strength of the material.
Fe	Balance	Balance	N/A

2.6. Strain and Strain rate

Flow stress and dislocation movement play an important role in the deformation characteristics of metallic material. Stress, temperature, and strain rate are properties that firmly influence the flow stress and failure response by changing the dislocation movement and deformability of materials. As strain rate increases, the stress necessary to shift dislocations through the material increases as several deformation mechanisms become active. To summarize, the behaviour of flow stress is dependent on strain rate and can be divided into three systems; the athermal system, the temperature and strain rate sensitive systems and the dislocation drag behaviour due to strain rates above $10^3 s^{-1}$ [75]. Therefore, the material behaviour due to strain rate needs to be examined due to a change in deformation characteristics.

Strain rate, expressed in s^{-1}, is the change of strain with respect to time and is given by the equation:

$$\dot{\varepsilon} = \frac{\delta\varepsilon}{\delta t} \ldots\ldots\ldots\ldots (2)$$

where, Δε is the change in strain within a time interval of Δ*t*. Strain rate sensitivity is linked with the permanent deformation of metals. Furthermore, this signifies a relation between metallurgical mechanisms causing strain rate sensitivity and plastic deformation in metallic materials. According to literature, high strain rate tests of mild steels present higher yield strengths and have different mechanisms of plastic flow when compared to that of low strain rate tests [76]. Further experiments on carbon steel were carried out at high strain rates and low and medium temperature [76]. As presented in Figure [2-8], different mechanisms of plastic deformation were observed at different strain rates and different temperatures. Edge dislocation mobility was detected as the governing mechanism in region 1. In region 2, nucleation and screw dislocation migration are the controlling mechanisms. However, in region 3 the controlling mechanism is twinning. Whereas at high strain rate, viscous drag is the governing mechanism in region 4 [76].

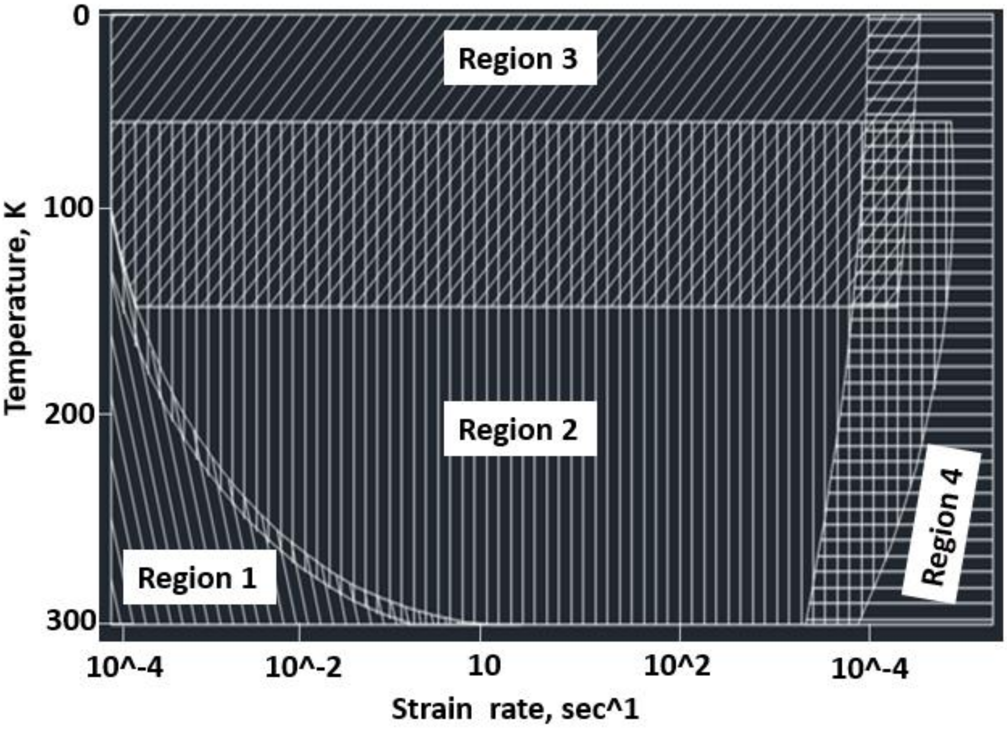

Figure 2-8 Temperature and strain rate spectrum of low carbon steel that reflect the mechanism of yielding [76]

2.6.1. High strain rate

High strain rate loading of materials occurs at strain rates between 10^2 and 10^6 and is realised in applications such as high-speed machining, ballistic impact, and bird strike s[77]. This method of testing is fundamental for validating the strain rate sensitivity and material response under compressive loading conditions at extreme speeds. Distinct inertia and wave propagation are the fundamental difference between high strain rate testing and quasi-static testing. The most used apparatus for high strain rate compression tests are the split Hopkinson pressure bar (also known as Kolsky-Hopkinson bar) and the modified Direct Impact Hopkinson pressure bar (DIHPB).

The split-Hopkinson pressure bar (SHPB) test was invented in its original form by John Hopkinson in 1872 and further modified by Kolsky in 1949 to establish and determine the dynamic properties of materials [77]. The SPHB apparatus consists of an air gun, a striker an incident bar and a transmitter bar as shown in Figure [2-9]. On the other hand, the DIHPB technique was popularized by Dharan & Hauser, revisited by Klepaczko and later modified Gorham [1]. The DIHPB apparatus consists primarily of five elements: (a)the projectile and transmitter bar, (b)a bearing and alignment fixture, (c)strain and velocity gauges, (d)compressed gas fixture and (e)a data collection system to document strain wave data. The DIHPB system is operated without the incident bar. The sample is sandwiched between the transmitter bar and the striker (incident bar or projectile). A predetermined velocity drives the striker to impact the specimen, thereby producing a strain and stress wave transmitted through the specimen. The specimen deforms plastically whiles the bars remain elastic to ensure the easy calculations of the strain and stress from the data obtained from the strain gauges. DIHPB testing influences high strains in the sample as well as recording material response in the form strain and strain rate [78], [79].

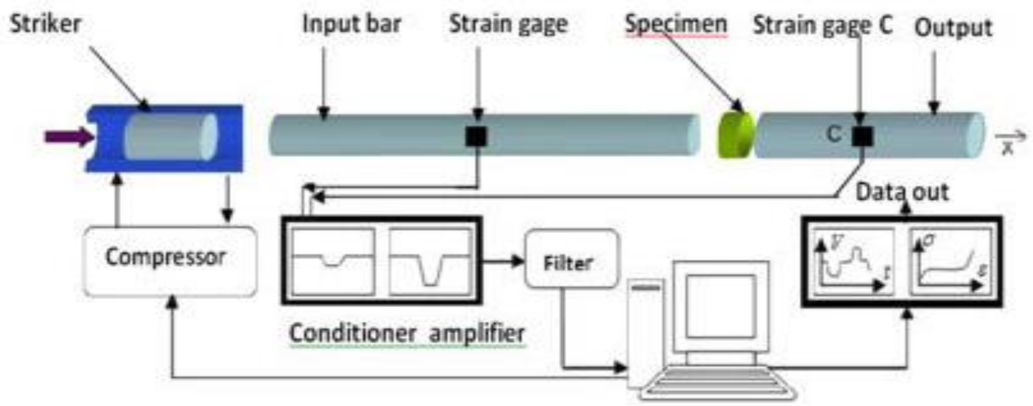

Figure 2-9. Diagram of a Split Hopkinson Pressure Bar[80]

According to Mecking et al. [81] material behaviour can be analyzed by considering the flow stress of a structure and the structural evolution with respect to strain. Their findings revealed strengthening contributions towards a materials flow's stress at constant structure is a systematic consolidation of the following: (a)the strength of dislocations, (b)grain boundaries, (c)interstitial and solute hardening, (d) lattice resistance and (e) hardening due to second phases. These conditions are products of barriers to dislocation motion, lattice structure, strain rate and temperature [81]. George Gray and Follansbee studied the effect of high strain rate deformation on FCC metals. They realised a thermal activation of dislocations with obstacles as the materials with FCC crystal structures underwent tests at $10^4 s^{-1}$, revealing observable flow stress at constant strain [82]. Further test displayed the strain rate sensitivity of FCC metals had relation to the microstructural evolution [82]. Pure FCC metals exhibit strain rate independent yielding when in fact post-yield strain hardening is dependent on rate [82]. Along with the aforementioned reasons, the reliability of strain hardening with decreasing temperature and increasing rate is due to overriding the dynamic recovery process [82]. BCC and HCP metals demonstrate a strong dependency on strain rate and temperature as a result of their high lattice resistance [82],[83]. Further studies revealed strain-hardening feedback after yielding imitate each other with relation to the change in strain rate [83].

2.6.2. High strain rate response of 3D printed metals

There are extensive studies on the dynamic behaviour of metal parts made by conventional manufacturing [84], [85]. However, little attention has been given to a comprehensive study of the high strain rate response of 3D printed 316L stainless steel alloy. It is well known that the fracture response and the mechanical strength of metal additively manufactured parts are greatly affected by the part density, loading rate and chemical composition. Due to the exceptional combination of properties of 316L stainless steel, the aerospace, nuclear, food, automobile, biomedical and defense industries have embraced this alloy for a wide range of applications [86]. Lee et al, [87] studied the effect of strain rate and sintered densities on the dynamic mechanical properties of 316L stainless steel. Their findings showed the mechanical properties of 316L sintered stainless steel changed under different strain rates and loading conditions. Furthermore, they reported an increase in flow stress with increasing strain rate whereas there was a decrease in fracture strain with increasing strain rate and relative density. They further added that the dominant fracture mechanism is intensive localized shearing leading to the formation of shear bands. Further studies were conducted by Kneen et al, [88]. Their findings revealed a transformation of austenite to martensite due to work hardening effect occurring at high strain rates [88], [89]. Kuelper at al, [79] identified the high strain rate response of different process parameters and build angle of additively manufacture 316L alloy. Their findings exhibited an overall variation in performance due to the build angle however, they were unable to confirm a correlation of flow stress with the build angle. Kluczynski et al, [90] studied the effect of each process parameter on the mechanical properties on the manufactured object. They observed different modes and positions for crack formations based on the printing parameters utilised. Lin et al, [91] investigated the effect of temperature and strain rate on the dynamic plastic behavior of conventionally manufactured Ti6Al4V alloy at varying strain rates. Lin et al, showed adiabatic shear banding was the major mode of fracturing leading to crack formation as well as revealing that the thickness and microhardness of shear bands changed at high strain rate and high temperature. Biswas et al, [92] studied the effects of porosity on the deformation and fracture behavior of additively manufactured porous Ti6Al4V alloy with both static and dynamic loadings. Their findings from the study showed adiabatic shear bands (ASBs) were the likely form of failure with ASBs nucleating within the pores. Fadida et al, [93] went further and studied the effect of pore behavior in additively manufactured Ti6Al4V alloy under dynamic loading conditions at high strain rates. This study revealed the dynamic behavior of additively manufactured Ti6Al4V had better strength performance compared to conventionally produced samples. Mohammadhosseini et al, [94] investigated the high strain rate effect of the static and dynamic behavior of Ti6Al4V alloy processed by electron beam melting additive manufacturing process. According to Mohammadhosseini et al, [94] the microhardness of the additively manufactured EBM Ti6Al4V sample was lower after high strain rate compression when compared to the pre-compression microhardness of the sample. Mostafa et al, [95] studied the microstructure and hot compression of selectively laser melted IN718 at strain rates of $0.1s^{-1}$ and $0.01s^{-1}$. In this study it was discovered δ-phase, MC carbides and Laves reduced the softening of the alloy as well as a lower strength being achieved by reducing the strain rate and increasing the deformation temperature.

Since the early 19th century, the military of France detonated cannon balls at specific blasts on metal samples to determine and observe the high strain rate mechanical behaviour and properties materials [77]. Hopkinson did high strain rate tests and concluded the dynamic loading produced higher stresses for materials whilst Tresca determined the heat created in the materials during plastic deformation [77]. As a result, interest in high strain rate deformation and failure has increased since the late 1900s due to the significance in engineering operations. The significance of high strain rate deformation tests is realised during earthquakes, structural impacts, blast loading, vehicle, and airplane accidents and many more. A considerable amount of literature has identified adiabatic shear band as a fundamental mode of failure at high strain rates in metals [77], [96], [97], [98]. Mechanical and metallurgical techniques have been used to examine high strain rate deformations by many researchers. It has been conclusively proved that quasi-static and intermediate strain rates present noticeably different mechanical properties when compared to what is detected from high strain rates. In Quasi-static and intermediate strain rates deformation, the failure mechanisms are identified by twinning and slip modes. However, adiabatic shear band is the failure mechanism observed in high strain rate loading. Adiabatic shear bands occur when strains are localized along narrow bands during deformation. Heat is produced and confined with no heat transfer along these bands to create adiabatic shear bands [99]. The shear bands have sheared material and are highly thin. Shear bands have been described as a factor of thermal softening, strain hardening and adiabatic heating occurring at high strain rate deformation according to Zenner et al, [100].

3. Methodology

3.1. Sample Processing

Table 2. Printing parameters for 316L stainless steel alloy

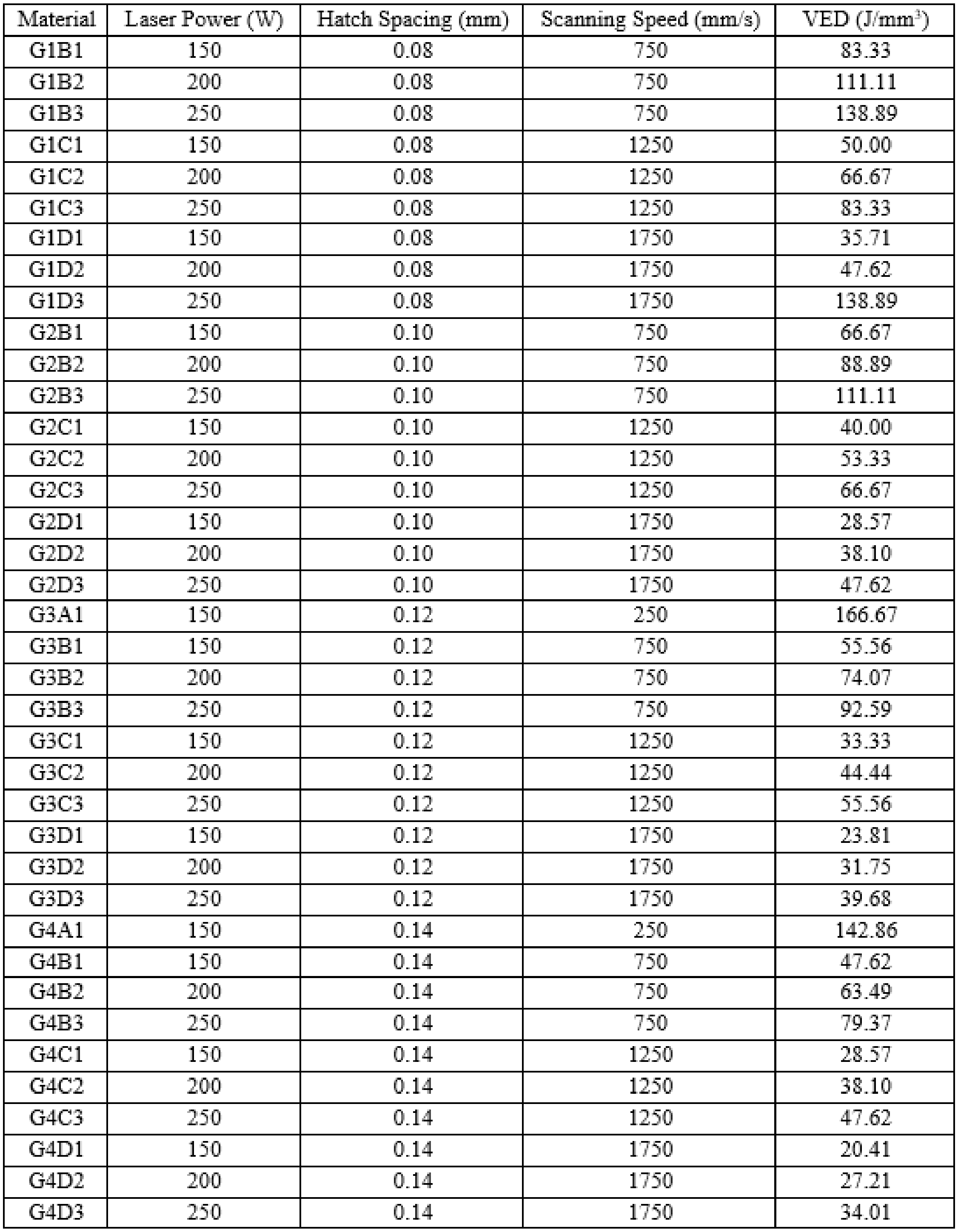

Material	Laser Power (W)	Hatch Spacing (mm)	Scanning Speed (mm/s)	VED (J/mm^3)
G1B1	150	0.08	750	83.33
G1B2	200	0.08	750	111.11
G1B3	250	0.08	750	138.89
G1C1	150	0.08	1250	50.00
G1C2	200	0.08	1250	66.67
G1C3	250	0.08	1250	83.33
G1D1	150	0.08	1750	35.71
G1D2	200	0.08	1750	47.62
G1D3	250	0.08	1750	138.89
G2B1	150	0.10	750	66.67
G2B2	200	0.10	750	88.89
G2B3	250	0.10	750	111.11
G2C1	150	0.10	1250	40.00
G2C2	200	0.10	1250	53.33
G2C3	250	0.10	1250	66.67
G2D1	150	0.10	1750	28.57
G2D2	200	0.10	1750	38.10
G2D3	250	0.10	1750	47.62
G3A1	150	0.12	250	166.67
G3B1	150	0.12	750	55.56
G3B2	200	0.12	750	74.07
G3B3	250	0.12	750	92.59
G3C1	150	0.12	1250	33.33
G3C2	200	0.12	1250	44.44
G3C3	250	0.12	1250	55.56
G3D1	150	0.12	1750	23.81
G3D2	200	0.12	1750	31.75
G3D3	250	0.12	1750	39.68
G4A1	150	0.14	250	142.86
G4B1	150	0.14	750	47.62
G4B2	200	0.14	750	63.49
G4B3	250	0.14	750	79.37
G4C1	150	0.14	1250	28.57
G4C2	200	0.14	1250	38.10
G4C3	250	0.14	1250	47.62
G4D1	150	0.14	1750	20.41
G4D2	200	0.14	1750	27.21
G4D3	250	0.14	1750	34.01

Laser power, Scan speed, hatch spacing were the selected parameters altered in printing the samples. An average particle size of 55µm and layer thickness of 30µm were used in the printing process. Table 2 presents the various parameters for each sample. Samples were grouped according to the hatch spacing and named accordingly. Laser power, laser scan speeds and hatch spacing were chosen and varied based on a range selected in a review by Yakout et al, [60] and Eliasu et al, [101]. The 316L coupons were printed with changing hatch spacing from 0.08, 0.01, 0.12 and 0.14mm, varying laser power from 150W, 200W to 250W as well as scan speeds from 250, 750, 1250 to 1750 mm/s.

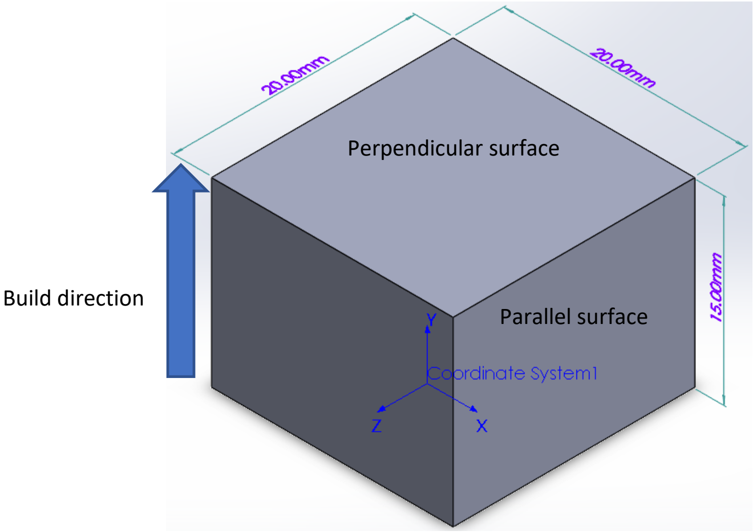

Figure 3-1. Build direction of samples

An EOS M280 Direct Metal Laser Sintering (DMLS) printer was used to process 38 cuboid parts with a geometry of 20mmx20mmx15mm in a nitrogen gas chamber at 375K. Figure [3-2] shows the printed coupons. A layer of 316L stainless steel powder was dispensed by a roller onto the printer platform whilst the printer chamber was heated up. The laser focuses and melts the cross-sectional area of the rectangular samples in the powder. The roller spreads the powder on the platform systematically after each fusing process. The laser melts the powder on each layer until the final layer was sintered to the rest of the specimen. The AISI 316L stainless steel chemical composition used by EOS is shown in Table [3].

Table 3: Chemical composition used by EOS

Element	Composition (%)
Fe	Balance
Cr	17.00 - 19.00
Mo	2.25 - 3.00
Ni	13.00 - 15.00
Mn	2.00
Cu	0.50
C	0.03
P	0.025
Si	0.75
S	0.01
N	0.10

Figure 3-2. Direct metal laser sintering a) schematic of coupons before printing, b) samples after DMLS printing, c-d) sample dimension after printing

3.2. Surface Preparation and Microstructural Characterization

The chemical and atomic structure of the samples were studied using some metallographic techniques. Samples were cold mounted in epoxy to help improve material handling to aid in grinding, polishing and microscopy. Samples were ground with 180, 400, 600, 800 and 1200 silicon carbide paper, to reach a smooth surface and reduce oxide layers present. Polishing with 0.1 and 0.05 µm alumina suspension was used to get a mirror-like finish and remove any surface damage. StarGrind 200-2V grinding and polishing stations were employed to grind and polish the 38 coupons. The grinding and polishing station are shown in Figure [3-3]. All samples were inspected under the optical microscope for different surface discontinuities. Samples were etched in a solution of $CuSO_4$, H_2O and HCl also known as marbles reagent, followed by water and ethanol cleaning to optically enhance microstructural features of the 316L stainless steel specimen. The samples were completely immersed in the reagent for 25 seconds before being washed and enhanced by running water and ethanol, respectively. Optical microscopy (OM) and Scanning electron microscopy (SEM) were used to examine the microstructure and properties of the samples.

Figure 3-3. a) Hot-mounting press b) grinding and polishing station

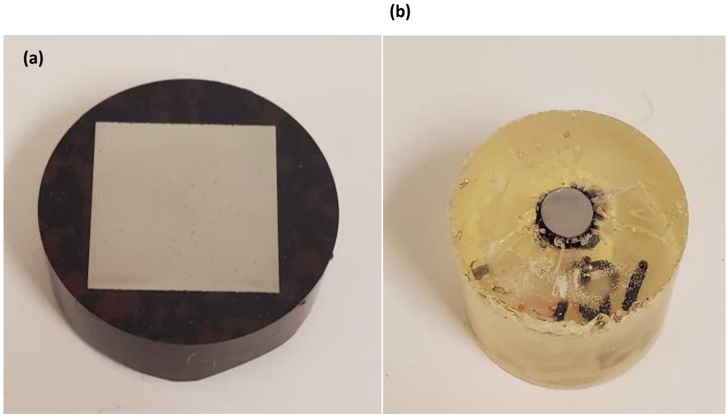

Figure 3-4. a) Mounted samples before impact b) Mounted samples after impact

Samples with less than 1% porosity were selected for impact tests. Four cylindrical samples each with a diameter of 4.75mm and length of 5.25mm were cut from each sample with a wire Electric Discharge Machine (EDM) as shown in Figure [3-5]. These samples were used for high strain rate dynamic impact experiments which will be further discussed in section 3.5. After impact, the surface preparation method was conducted again to enhance microstructural features after impact. All samples were examined with a scanning electron microscope (FE-SEM) to observe the morphology of the 316L coupons. The FE-SEM chamber was kept under vacuum in the presence of nitrogen gas.

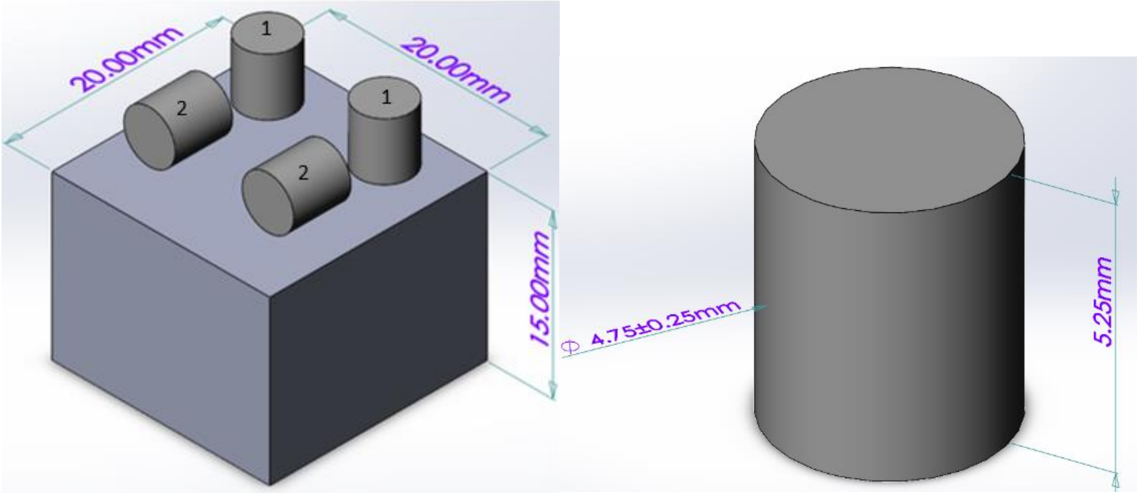

Figure 3-5. Sample Orientation from cut-out. Orientation 1 represents along the build direction and Orientation shows perpendicular to the build direction b) Geometry of Test specimen for Impact Loading

3.3. Porosity and Density Measurement

The amount pores on all samples were measured using optical techniques and image analysis software imagej as shown in Table [4]. Optical microscopes were used to take micrographs of unetched samples at varying magnifications. ImageJ software was employed to threshold each micrograph to establish a colour contrast between the pores and sample surface. For image processing, 15 individual images with one magnification (100x) were used to improve accuracy of results. Sectioned perpendicular and parallel views were chosen for image processing. The mean porosity values were obtained from the percent volume fraction from each of the 15 images per sample.

Bulk densities of all 3D printed samples were determined using the Archimedes principle according to ASTM B962-17. Trapped dirt was removed with soap and further cleaned with deionized water and ethanol to remove surplus soap from the surface in an ultrasonic bath. Distilled water was used as the medium for immersion to determine the densities of all samples. Table [4] presents the densities of 3D printed samples.

Table 4. Porosity, density and hardness measurements for 316L

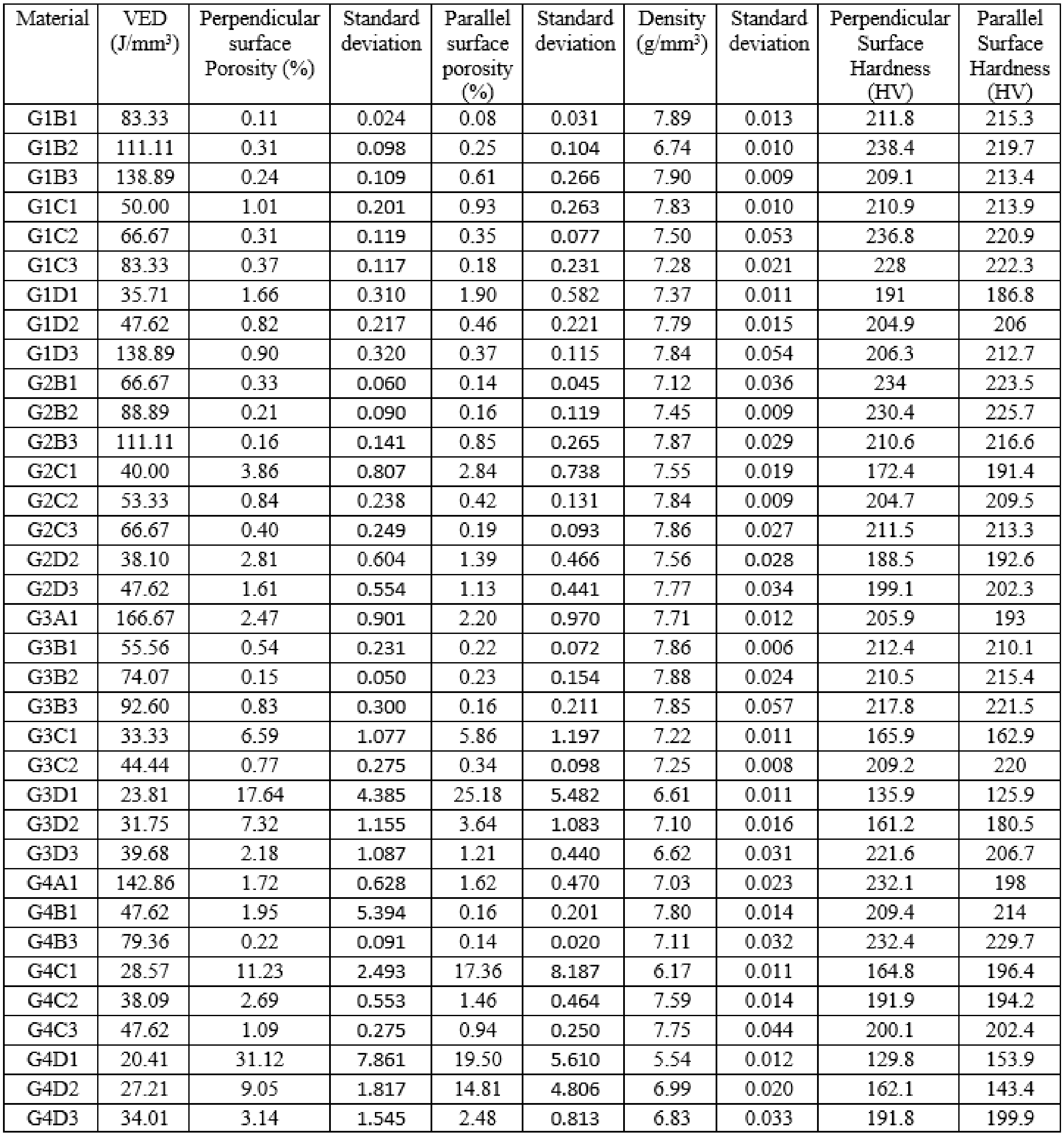

Material	VED (J/mm^3)	Perpendicular surface Porosity (%)	Standard deviation	Parallel surface porosity (%)	Standard deviation	Density (g/mm^3)	Standard deviation	Perpendicular Surface Hardness (HV)	Parallel Surface Hardness (HV)
G1B1	83.33	0.11	0.024	0.08	0.031	7.89	0.013	211.8	215.3
G1B2	111.11	0.31	0.098	0.25	0.104	6.74	0.010	238.4	219.7
G1B3	138.89	0.24	0.109	0.61	0.266	7.90	0.009	209.1	213.4
G1C1	50.00	1.01	0.201	0.93	0.263	7.83	0.010	210.9	213.9
G1C2	66.67	0.31	0.119	0.35	0.077	7.50	0.053	236.8	220.9
G1C3	83.33	0.37	0.117	0.18	0.231	7.28	0.021	228	222.3
G1D1	35.71	1.66	0.310	1.90	0.582	7.37	0.011	191	186.8
G1D2	47.62	0.82	0.217	0.46	0.221	7.79	0.015	204.9	206
G1D3	138.89	0.90	0.320	0.37	0.115	7.84	0.054	206.3	212.7
G2B1	66.67	0.33	0.060	0.14	0.045	7.12	0.036	234	223.5
G2B2	88.89	0.21	0.090	0.16	0.119	7.45	0.009	230.4	225.7
G2B3	111.11	0.16	0.141	0.85	0.265	7.87	0.029	210.6	216.6
G2C1	40.00	3.86	0.807	2.84	0.738	7.55	0.019	172.4	191.4
G2C2	53.33	0.84	0.238	0.42	0.131	7.84	0.009	204.7	209.5
G2C3	66.67	0.40	0.249	0.19	0.093	7.86	0.027	211.5	213.3
G2D2	38.10	2.81	0.604	1.39	0.466	7.56	0.028	188.5	192.6
G2D3	47.62	1.61	0.554	1.13	0.441	7.77	0.034	199.1	202.3
G3A1	166.67	2.47	0.901	2.20	0.970	7.71	0.012	205.9	193
G3B1	55.56	0.54	0.231	0.22	0.072	7.86	0.006	212.4	210.1
G3B2	74.07	0.15	0.050	0.23	0.154	7.88	0.024	210.5	215.4
G3B3	92.60	0.83	0.300	0.16	0.211	7.85	0.057	217.8	221.5
G3C1	33.33	6.59	1.077	5.86	1.197	7.22	0.011	165.9	162.9
G3C2	44.44	0.77	0.275	0.34	0.098	7.25	0.008	209.2	220
G3D1	23.81	17.64	4.385	25.18	5.482	6.61	0.011	135.9	125.9
G3D2	31.75	7.32	1.155	3.64	1.083	7.10	0.016	161.2	180.5
G3D3	39.68	2.18	1.087	1.21	0.440	6.62	0.031	221.6	206.7
G4A1	142.86	1.72	0.628	1.62	0.470	7.03	0.023	232.1	198
G4B1	47.62	1.95	5.394	0.16	0.201	7.80	0.014	209.4	214
G4B3	79.36	0.22	0.091	0.14	0.020	7.11	0.032	232.4	229.7
G4C1	28.57	11.23	2.493	17.36	8.187	6.17	0.011	164.8	196.4
G4C2	38.09	2.69	0.553	1.46	0.464	7.59	0.014	191.9	194.2
G4C3	47.62	1.09	0.275	0.94	0.250	7.75	0.044	200.1	202.4
G4D1	20.41	31.12	7.861	19.50	5.610	5.54	0.012	129.8	153.9
G4D2	27.21	9.05	1.817	14.81	4.806	6.99	0.020	162.1	143.4
G4D3	34.01	3.14	1.545	2.48	0.813	6.83	0.033	191.8	199.9

3.4. Hardness Testing

The Vickers micro-hardness tester was used to measure hardness in accordance with the E92-17 ASTM standard. This equipment is equipped with a pyramidal diamond tip indenter to depress the sample surface with a fixed amount of force. A constant load of 2.94N was applied to the surface of the sample with a dwell time of 15s for each indentation. To achieve more accurate results, 15 different indentations were made per sample. Due to the pyramidal shape of the indent, the diagonal length of each indent was measured to calculate the Vickers hardness value (HV). The average measured lengths were used with the microhardness equipment and the built-in software to obtain the matching hardness. The average of the 15 indentations made was defined as the average hardness of the sample. Table [4] presents the microhardness values of the samples.

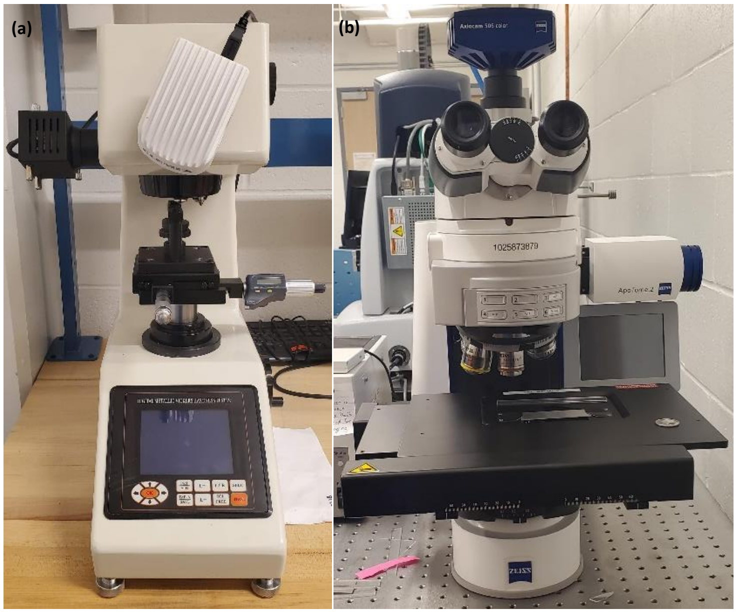

Figure 3-6. a) Vickers hardness tester, b) Optical Microscope

3.5. Impact Testing

To study the influence of process parameters on the high strain rate properties of dense AM 316L stainless steel specimen, a Direct Impact Hopkinson Bar (DIHPB) was employed to simulate impact at high strain rates. Samples with 99% relative density were selected to be impacted at room temperature. Cut coupons were impacted at a pressure of 15kPa. To determine the dynamic compression properties of solid materials, several researchers have used various forms of the Hopkinson Pressure Bar. At York University, a converted version of the Hopkinson Pressure Bar has been established to obtain high compression strains up to $10^4 s^{-1}$. This apparatus was employed in this current study to impact the AM 316L steel samples because of its ability to establish homogeneous compression at high strain rate impacts. The impact at high strain rate with the DIHPB establishes a strain-stress relationship and behaviour of the 316L stainless steel sample.

The DIHPB consists of a cylindrical projectile, transmitter bar, gun barrel, control box, accumulator, strain gauge and the firing chamber. As shown inf Figure [3-7], the accumulator stores compressed air that forces the projectile to move and impact at high speeds. A pressure gauge was used to regulate the firing pressure. The control box was used to switch the DIHPB setup on with the power switch button. To fire the projectile, a second button on the control box was triggered. After firing, the projectile was reset, and the process repeated with another specimen. The projectile and transmitter bar are made of hardened 4340 steel. The projectile was propelled with the pressurized air and directed by the gun barrel to impact the specimen at high strain rates.

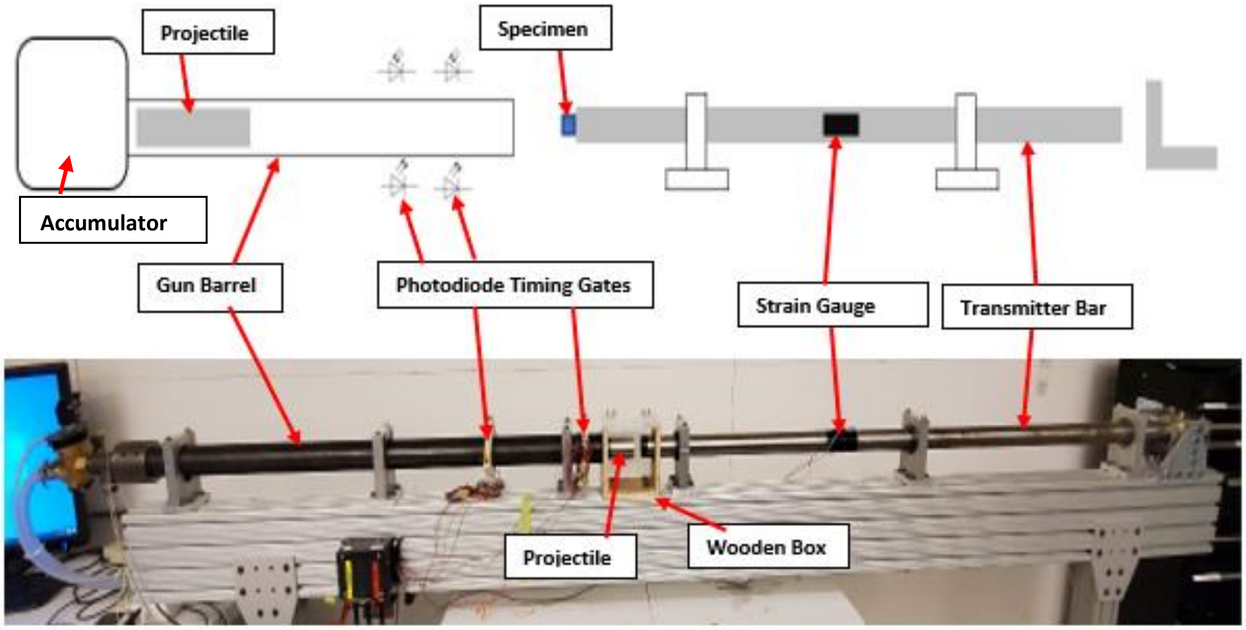

Figure 3-7. Direct Impact Hopkinson Pressure Bar (DIHPB)

A minute amount of petroleum jelly (high viscous gel) was applied on the flat surfaces of the specimen to reduce friction and improve adhesion to the transmitter bar. The reduction of friction ensures homogenous deformation and prevents barreling of the specimen. The specimens are attached on the center-face of the transmitter bar before the projectile was fired. As shown in Figure [3-7], a wooden box was placed around the specimen to prevent flying parts from a fractured specimen and reduce noise during impact. The hardened 4340 steel projectile strikes the specimen fixed to the surface of the transmitter bar and generates a compressive wave which conveys through the specimen to the transmitter bar. The strain gauge attached to the transmitter bar captures the elastic waves generated during the deformation. The signal was transmitted to the LabView software of the connected computer. The LabView software stores and displays the data as Voltage-Time curve. The firing pressure was maintained at 15kPa for all the experiments to produce a strain rate within 6000s^{-1} to 8000s^{-1} range. Components of the Direct Impact Hopkinson Pressure Bar (DIHPB) used for the current study is shown in Figure [3-7].

The transmitter bar with the strain gauge attached and a load cell. With the calibration, the relationship between the measured voltage and load is:

$$P=301V\ldots\ldots(3)$$

Where P is the load in Kilo Newton (kN) and V is the matching voltage in Milli Volt (mV). Assuming a linear change in rate of displacement and constant strain rate, the engineering stress and engineering strain equations are given by

$$\sigma(t) = \frac{P(t)}{Ai}\frac{Li-(Li-Lf)(t/tf)}{Li}\ldots\ldots(4)$$

$$\varepsilon(t) = \ln\frac{Li}{Li-(Li-Lf)(t/tf)}\ldots\ldots(5)$$

where $\sigma(t)$ is the engineering stress, $P(t)$ is the load with respect to time in kilo newtons, Ai is the surface area before deformation in mm^2, tf is the final time in seconds (s), Li and Lf are the initial length and final length in millimeters (mm) respectively. The strain rate, maximum strain and projectile length are linked by the equation:

$$\dot{\varepsilon} = \frac{C}{2l}\varepsilon\ldots\ldots(6)$$

where C is the longitudinal wave propagation velocity in the transmitter bar. The global strain rates were determined after the high strain rate deformation of the specimen were conducted.

4. Results

4.1. Effect of VED and printing parameters on part surface porosity

4.1.1. Effect of VED on porosity

The effect of individual print parameters on the level of pores are studied in this section. The highest porosity is observed in sample G4D1 with a percentage of 31%, whereas sample G1B1 registered the lowest porosity of 0.08%. Generally, the VED has a good correlation to the level of porosity on the surface of the samples. As evident in Figure [4-1(a-b)], increasing the VED shows a progressive reduction in part porosity. However, after a VED threshold of approximately 140 J/mm^3, the pores begin to re-emerge. This is true for porosity levels of both surfaces as seen in Figures [4-2] and [4-3]. The correlation between VED and part porosity created three cases as seen in Table 3. For the first case, samples with VED from 20-40J/mm^3 showed the worst level of porosity (1.2-31.1%). Secondly, samples with VED from 44.44-138 J/mm^3 reported the best porosity levels (below 1%). The final case involves samples with high VED (142.86-166.67 J/mm^3), which showed a re-appearance of pores (1-3%). Also, it is clear from Table 3 that surface porosity on the top surface are more than the porosity on the side surfaces.

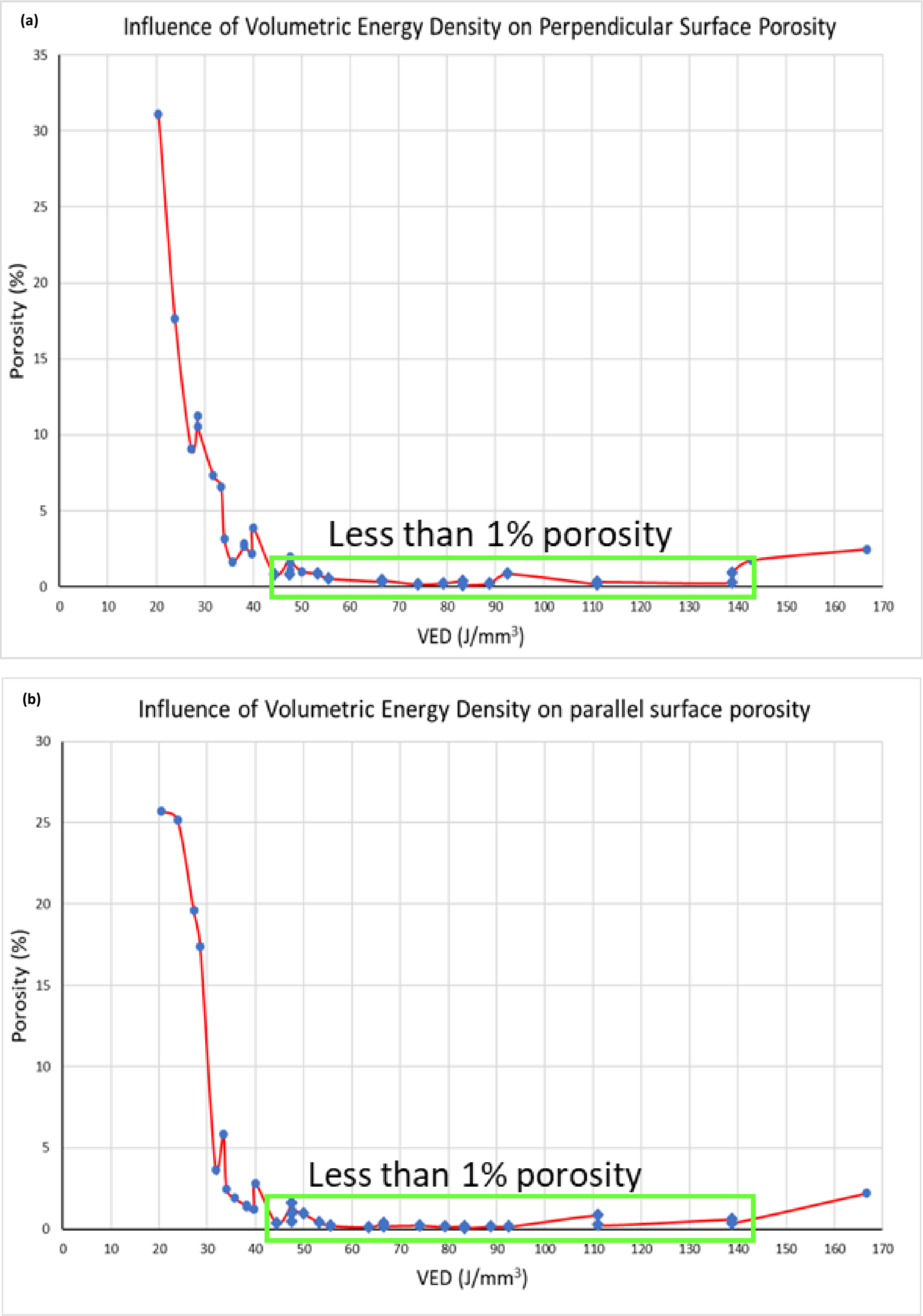

Figure 4-1: Porosity as a function of VED (a)Surface porosity on parallel face, (b) Surface porosity on perpendicular face

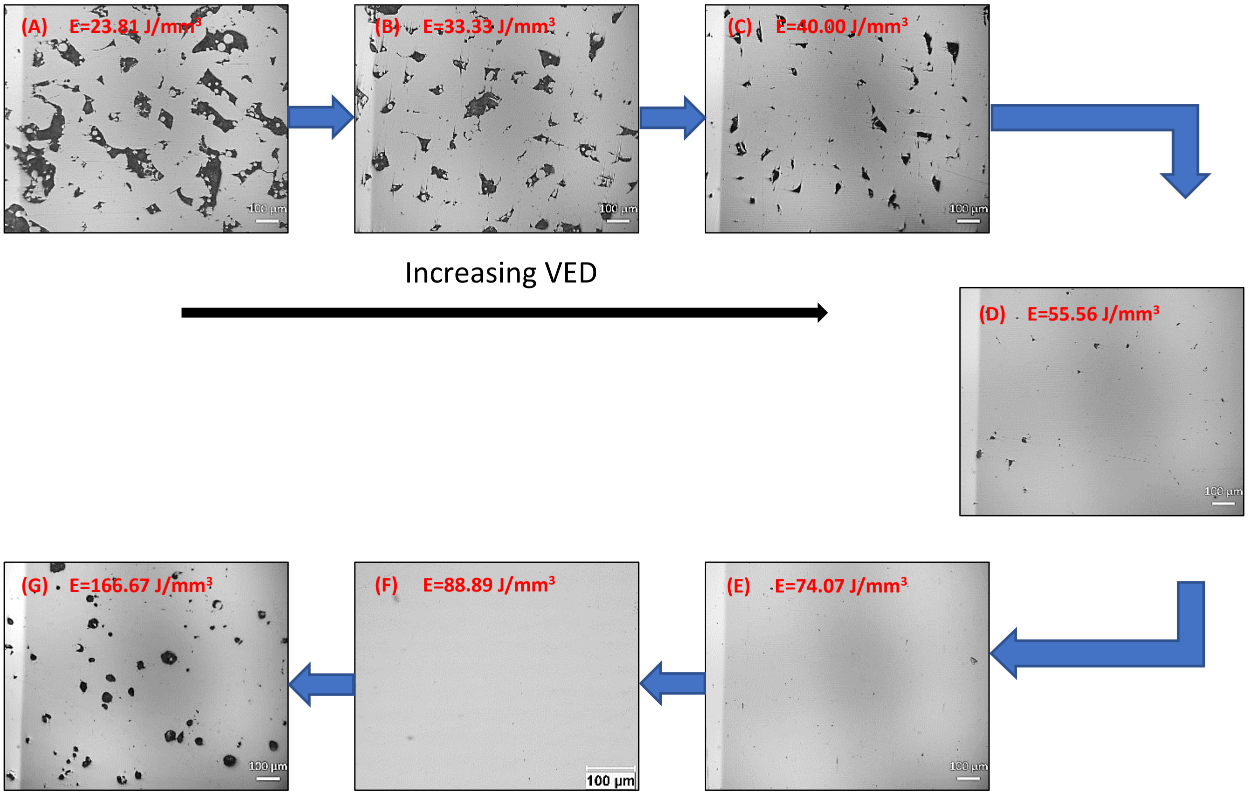

Figure 4-2. Effect of increasing Volumetric Energy Density on parallel surface porosity (A) low VED at 23.81 J/mm^3 with high amount and large sized pores, (C) relatively smaller number of pores at 33.33 J/mm^3, (D) average amount and small sized pores 55.56 J/mm^3, (E-F) low level of pores after 74.07 J/mm^3, (G) resurgence of pores at 166.67 J/mm^3

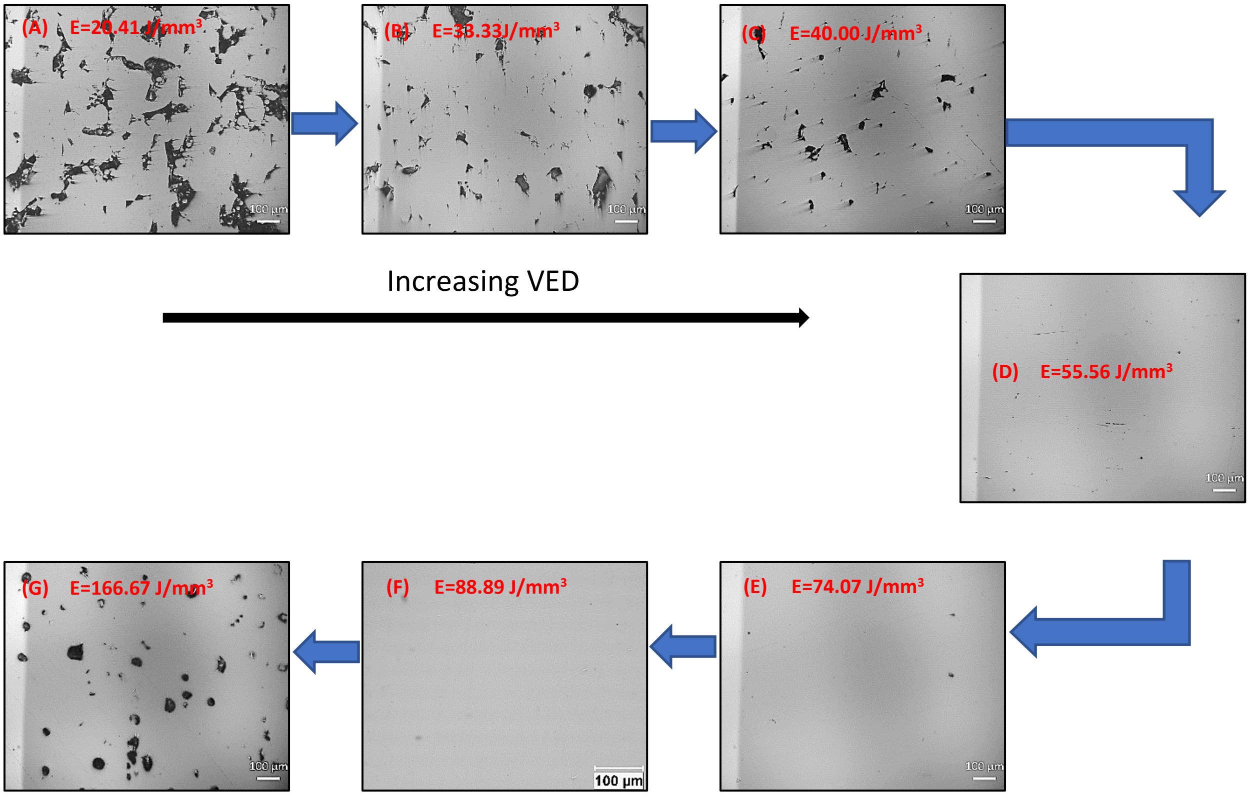

Figure 4-3. Effect of increasing Volumetric Energy Density on perpendicular surface porosity (A) low VED at 20.41 J/mm^3 with high amount and large sized pores, (C) relatively smaller number of pores at 33.33 J/mm^3, (D) average amount and small sized pores 55.56 J/mm^3, (E-F) low level of pores after 74.07 J/mm^3, (G) resurgence of pores at 166.67 J/mm^3

4.1.2. Effect of Laser Power on porosity

The individual parameters affect the level of porosity on the sample surface in different ways. First, the influence of power on the perpendicular surface porosity is assessed. Generally, increasing the laser power leads to decrease in surface porosity as seen in Figure [4-4]. However, when using a hatch spacing of 0.08mm, a direct correlation between laser power and porosity is seen in samples created with a scan speed of 750 mm/s. In this case, increasing the power does not show the same level of correlation as seen when using either 1250 mm/s or 1750 mm/s, in certain instances an inverse relationship between scan speed and porosity is observed as seen in Figure [4-4a]. Furthermore, at hatch spacing of 0.08mm and scan speeds of

750, 1250 and 1750 mm/s, a 33% increase in the laser power produced a 172.3% increase, 69.1% decrease and 50% decrease in porosity, respectively. An opposite trend was observed when the laser power was further increased by 25% to produce a 21.1% decrease, 14.5% increase and 9.9% increase in porosity at 750, 1250, and 1750mm/s scan speed, respectively. At a hatch spacing of 0.10mm a relatable trend was observed, increasing the power led to a decrease in surface porosity as seen in Figure [4-4b]. At hatch spacing of 0.10mm and scan speeds of 750, 1250 and 1750 mm/s, a 33% increase in the laser power produced a 36.2% decrease, 78.2% decrease and 73.3% decrease in porosity, respectively. Similarly, a further increase by 25% produced a 25.2% decrease, 52.2% decrease and 42.7% decrease in perpendicular surface porosity at 750, 1250 and 1750mm/s, respectively. Furthermore, maintaining a hatch spacing of 0.12mm and scan speeds of 750, 1250 and 1750mm/s the laser power is increased by 33% and further increased by 25%. An increase in laser power by 33% produced 72.6% decrease, 88.3% decrease and 58.5% decrease whereas, a further 25% increase in laser power produced a 464.5% increase, 33.7% decrease and a 70.2% decrease in perpendicular surface porosity at 750, 1250 and 1750mm/s scan speeds, respectively. Lastly, an identical downward trajectory was observed with increasing laser power at a maintained hatch spacing of 0.14mm and scan speeds of 750, 1250 and 1750mm/s. The 33% increase in laser power produced a 73.8% decrease, 76.1% decrease and 70.9% decrease in perpendicular surface porosity at 750, 1250, and 1750mm/s respective scan speeds. The additional increase of 25% in laser power at 750, 1250 and 1750mm/s scan speed created a 56.8% decrease, 59.3% decrease and 65.4% decrease in perpendicular surface porosity, respectively. Thus, porosity decreases when laser power increase, however, the percentage of change is dependent on the other parameters as well.

The sensitivity of porosity to laser power on the parallel surface is also studied. Increasing the laser power generally resulted in a drop in parallel surface porosity. However, at a hatch spacing of 0.08mm and scan speeds of 750, 1250 and 1750 mm/s, a 33% increase in the laser power produced a 205.3% increase, 62.2% decrease and 75.9% decrease in porosity, respectively. Also, an additional 25% increase in laser power produced a 145.9% increase, a 49.9% decrease and a 19.2% decrease in parallel surface porosity. At hatch spacing of 0.10mm and scan speeds of 750 and 1250mm/s, a 33% increase in the laser power produced a 19.3% increase and 85.1%% decrease in porosity, respectively. A further increase by 25% produced a 425.1% increase, 54.9% decrease and 19% decrease in parallel surface porosity at 750, 1250 and 1750mm/s, respectively. Maintaining a hatch spacing of 0.12mm and scan speeds of 750, 1250 and 1750mm/s the laser power is increased by 33% and further increased by 25%. An increase in laser power by 33% produced 2.5% increase, 94.2% decrease and 85.5% decrease in parallel surface porosity at the corresponding speeds. A further 25% increase in laser power at 750 and 1750 mm/s produced a 30% decrease and a 66.7% decrease in parallel surface porosity, respectively. Lastly, an identical downward trend was observed with increasing laser power at a fixed hatch spacing of 0.14mm and scan speeds of 750, 1250 and 1750mm/s. The 33% increase in laser power produced a 16.7% decrease, 91.6% decrease and 23.6% decrease in parallel surface porosity at 750, 1250, and 1750mm/s respective scan speeds. The additional increase of 25% in laser power at 750, 1250 and 1750mm/s scan speed created a 9.2% increase, 35.4% decrease and 87.4% decrease in parallel surface porosity, respectively.

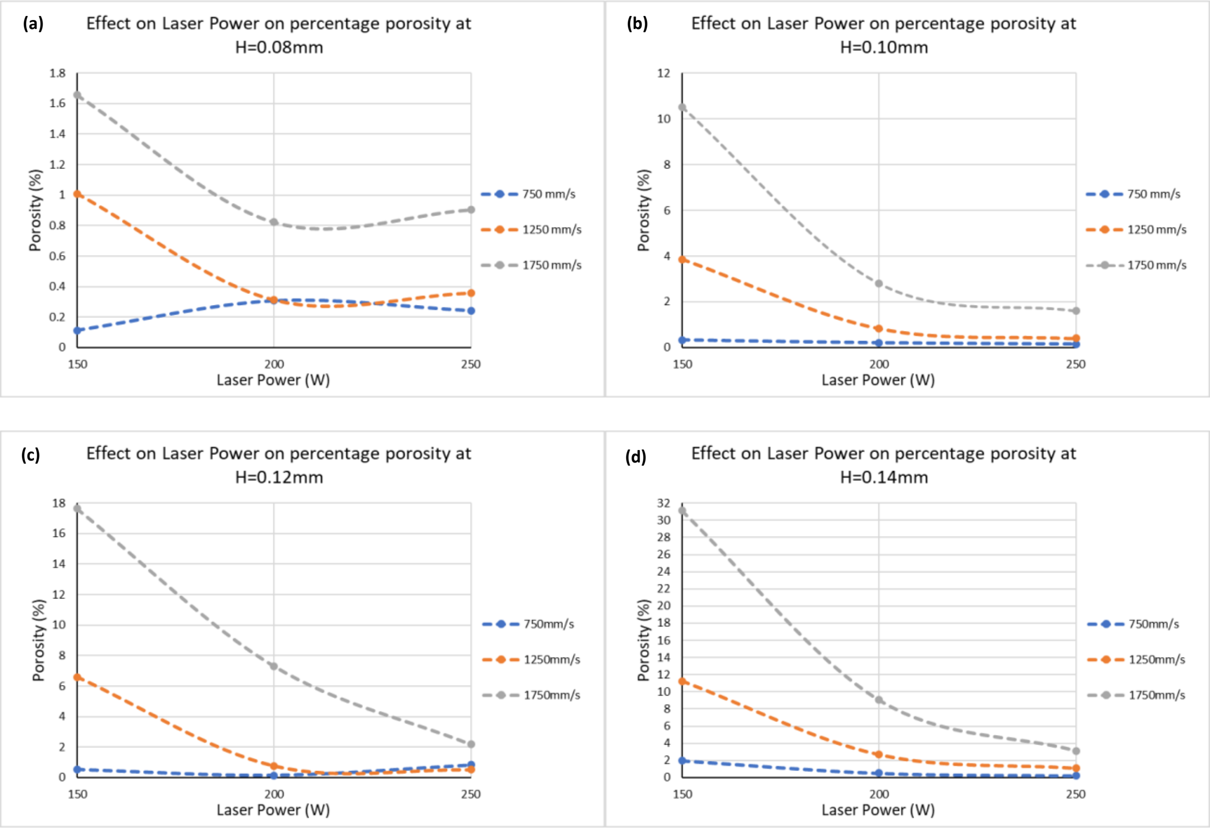

Figure 4-4. Effect of Printing Parameters on porosity

Figure [4-5], shows the SEM micrographs of samples G2C1, G2C2 and G2C3, respectively. As seen in Figures [4-5], a progressive change in the size, shape and number of pores is evident with increasing power. The mean pore area at 150W for the G2C1 sample was 839.6µm^2 whereas, a 33.3% increase in power produced a mean pore area of 143.1µm^2 for the G2C2. The average pore area thereby reduced by 83% with a 33.3% increase in laser power. A further 25% increase in laser power produced a mean pore area of 60.2µm^2. This further presents a 57.9% reduction in average pore area whilst increasing laser power by 25%. Thus, increasing power whilst other parameters are maintained produced a reduction in pore average pore size as presented in Figure [4-4].

In summary, an increase in laser power results in a decline in porosity on both surfaces. However, the percentage of change porosity is dependent on the other parameters as well. At a hatch spacing of 0.08mm and scan speed of 750, the surface porosity is increases with increasing laser power. On the other hand, at scan speeds of 1250 and 1750mm/s, an increase in laser power to 200W results in decrease in surface porosity whereas an increase in laser power from 200W to 250W produced an increase in surface porosity. As shown in Figure [4-4(b-c)], a systematic increase in laser power from 150W, to 200W and 250W resulted in a general decrease in surface porosity. However, the rate of decrease in surface porosity increased at higher scan speeds.

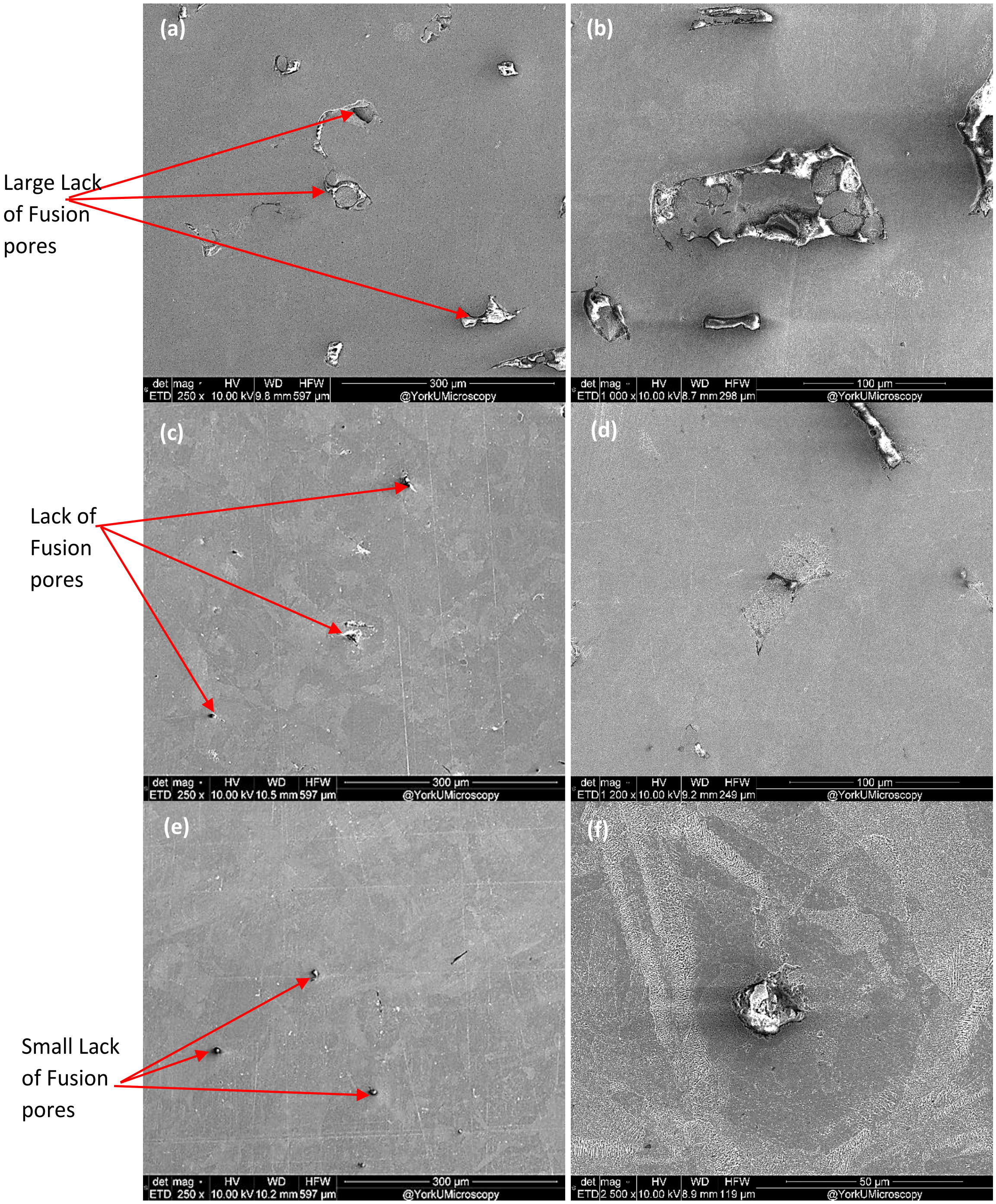

Figure 4-5. Micrographs of effect of Laser Power on Pore shape and size at 0.10mm Hatch Spacing and 1750mm/s Scan Speed a-b) 150W c-d) 200W e-f) 250W

4.1.3. Effect of Hatch Spacing on porosity

The influence of hatch spacing on the surface porosity is evaluated. Generally, increasing the hatch spacing whilst maintaining other parameters leads to an increase in surface porosity as seen in Figure [4-4]. At a maintained power of 150W and scan speeds of 750, 1250 and 1750 mm/s, a 25% increase in the hatch spacing produced a 188.6% increase, 282.7% increase and 534.5% increase in perpendicular surface porosity at the respective scan speeds. A further 20% increase in hatch spacing produced 64.6% 70.6% and 67.8% increases in perpendicular surface porosity at 750, 1250, and 1750 scan speeds, respectively. An additional 16.7% increase in hatch spacing resulted in a further increase in porosity by 264.7%, 70.5% and 76.4% at 750, 1250 and 1750mm/s respective scan speeds. Furthermore, maintaining a laser power of 200W and scan speeds of 750, 1250 and 1750mm/s the hatch spacing is progressively increased by 25%, 20% and a further 16.7% increase. An increase in hatch spacing by 25% produced 32.4% increase, 169.8% increase and 241.6% increase whereas, a further 20% increase in hatch spacing produced a 29.4% increase, 8.4% increase and a 160.5% increase in perpendicular surface porosity at 750, 1250 and 1750mm/s scan speeds, respectively. An additional 16.7% increase in hatch spacing created 249%, 248.5% and 23.7 increases in porosity at respective scan speeds of 750, 1250 and 1750mm/s. At a fixed laser power of 250W and scan speeds of 750, 1250 and 1750mm/s, the hatch spacing was increased progressively to determine the number of pores produced. A 25% increase in hatch spacing resulted in 36% decrease,12.7% increase and 78.2% increase in perpendicular surface porosity at 750, 1250 and 1750 scan speeds, respectively. An additional increase in hatch spacing by 20% produced 433.2% increase, 27.1% increase and 35.3% increase whereas, a further 16.7% increase in hatch spacing produced a 73.3% decrease, 113.7% increase and a 44% increase in perpendicular surface porosity at 750, 1250 and 1750mm/s scan speeds, respectively. It is observed altering the hatch spacing had a significant effect on the creation of pores within the samples.

The influence of porosity to hatch spacing on the parallel surface is also studied. Increasing the hatch spacing generally resulted in a rise in parallel surface porosity. To determine the effect of hatch spacing on the parallel surface porosity, laser power and scan speed was kept constant. At a maintained power of 150W and scan speeds of 750 and 1250mm/s, a 25% increase in the hatch spacing produced a 68.6% increase and 203.6% increase in parallel surface porosity at the corresponding scan speeds. A further 20% increase in hatch spacing produced 63.4% and 106.5% increases in parallel surface porosity at 750 and 1250 scan speeds, respectively. An additional 16.7% increase in hatch spacing resulted in a 28.6% decrease, 196.5% increase and 2% increase at 750, 1250 and 1750mm/s corresponding scan speeds. Furthermore, maintaining a laser power of 200W and scan speeds of 750, 1250 and 1750mm/s the hatch spacing is progressively increased by 25%, 20% and a further 16.7% increase. An increase in hatch spacing by 25% produced 34.1% decrease, 19.6% increase and 203.4% increase whereas, a further 20% increase in hatch spacing produced a 40.3% increase, 20.3% decrease and a 162.1% increase in parallel surface porosity at 750, 1250 and 1750mm/s scan speeds, respectively. An additional 16.7% increase in hatch spacing created 42% drop, 333.3% increase and 439% increase in porosity at respective scan speeds of 750, 1250 and 1750mm/s. At a fixed laser power of 250W and scan speeds of 750, 1250 and 1750mm/s, the hatch spacing was increased progressively to determine the number of pores produced. A 25% increase in hatch spacing resulted in 40.7% increase, 7.7% increase and 204.3% increase in parallel surface porosity at 750, 1250 and 1750 scan speeds, respectively. An additional increase in hatch spacing by 20% produced 81.3% decrease and 7.7% increase at scan speeds of 750mm/s and 1750mm/s, respectively. A further 16.7% increase in hatch spacing produced a 9.5% decrease and 104.4% increase in parallel surface porosity at 750 and 1750mm/s scan speeds, respectively. It is observed altering the hatch spacing had a significant effect on the creation of pores within the samples however, the trend is more observable on the perpendicular surface.

Figure [4-6], shows the SEM micrographs of samples G1D2, G2D2, G3D2 and G4D2, respectively. As seen in Figures [4-6], a progressive change in the size, shape and number of pores is evident with increasing hatch spacing. The mean pore area at 0.08mm for the G1D2 sample was 68.2µm^2 whereas, a 25% increase in hatch spacing produced a mean pore area of 584.2µm^2 for the G2D2. The average pore area thereby increased by 756.6% with a 25% increase in hatch spacing. A further 20% and 16.7% increase in hatch spacing produced a mean pore area of 1634.2µm^2 and 3192.2µm^2 respectively. This presents an increase of the average pore area 179.7% and 95.3% accordingly. Thus, increasing hatch spacing whilst other parameters are maintained produced an increase in pore average pore area as presented in Figure [4-6]. However, the rate of increase reduces drastically with increasing hatch spacing.

In summary, increasing hatch spacing results in higher average surface porosity. An increase in hatch spacing from 0.08mm to 0.10mm, resulted with a higher amount of surface pores at similar laser powers and scan speeds. A similar trend was observed at with an increase in hatch spacing from 0.10mm to 0.12mm and 0.14mm.

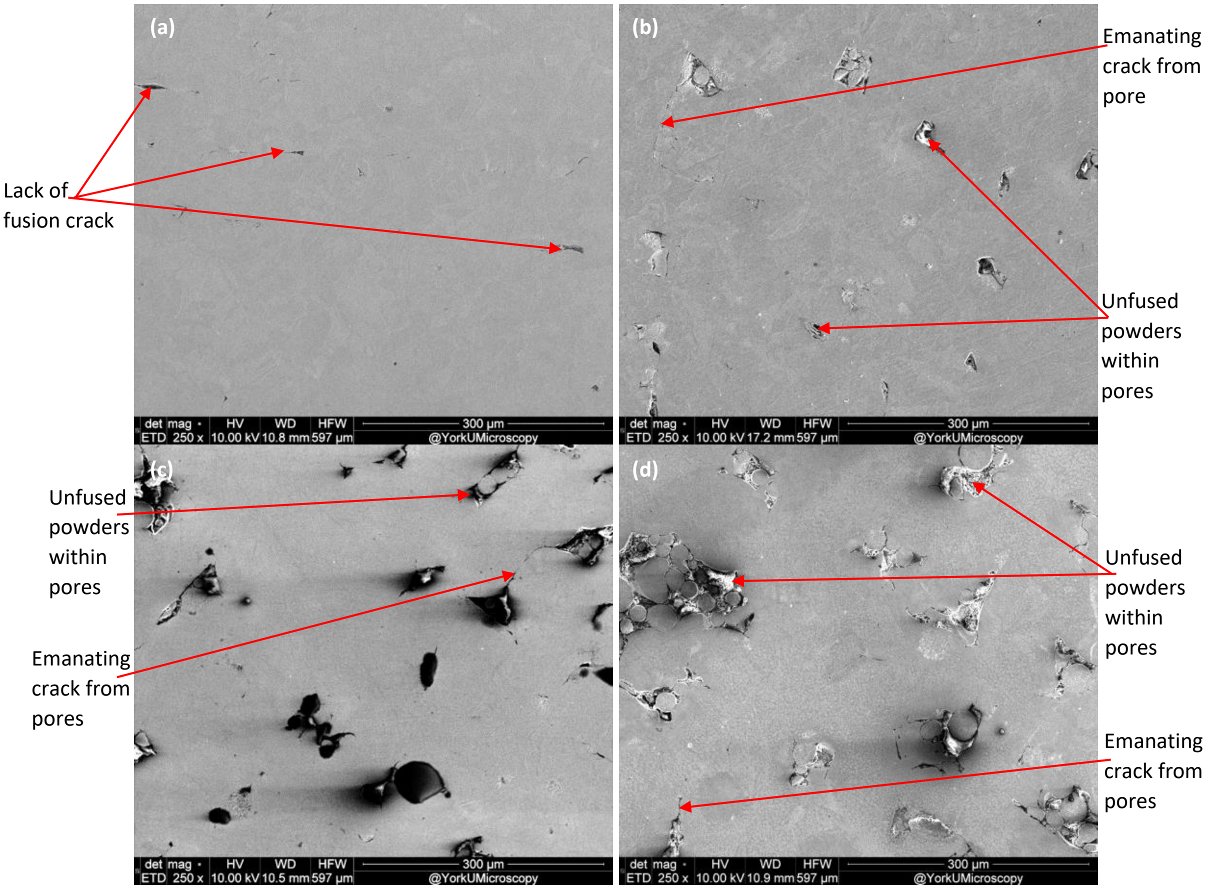

Figure 4-6. Micrographs of effect of Hatch Spacing on Pore shape and size at 200W Laser Power and 1750mm/s Scan Speed a) 0.08 mm b) 0.10 mm c) 0.12 mm d) 0.14 mm

4.1.4. Effect of Scan Speed on surface porosity

Finally, the effect of altering scan speed on the production of pores was explored. Scan speeds from 250mm/s was increased progressively by 200%, 66.7% and 40% to speeds of 750, 1250 and 1750mm/s. To examine the effect of scan speed on the generation of pores, laser power and hatch spacing were kept constant. Generally, increasing the scan speed whilst maintaining other parameters led to an increase in perpendicular surface porosity as seen in Figure [4-4]. At a scan speed of 250mm/s, most samples were completely burnt and did not consolidate. Parts printed at scan speeds of 250mm/s were completely burnt when printed with either low hatch spacing or higher laser power. Figure [4-7] presents samples printed with low scan speeds, low hatch spacing or high laser power. However, at hatch spacing of 0.08mm and laser powers of 150, 200 and 250 W, a 66.7% increase in the scan speed from 750mm/s to 1250mm/s produced a 795.2% increase, 1.6% increase and 47.4% increase in porosity at the respective laser powers. A further 40% increase in scan speed produced 64.2%, 163.6% and 153% increase in perpendicular surface porosity at 150, 200 and 250W laser power. At hatch spacing of 0.10mm and laser powers of 150, 200 and 250 mm/s, a 66.7% increase in the scan speed produced a 1086.8% increase, 305.8% increase and 159.4% increase in porosity, at the respective laser powers. Similarly, a further 40% increase scan speed produced a 172.3% increase, 233.7% increase and 300% increase in perpendicular surface porosity at 150, 200 and 250W, respectively. At a hatch spacing of 0.12mm, a 200% increase in scan speed produced a 78.3% increase in perpendicular surface porosity. Similarly, an additional 66.7% increase in scan speed resulted in a 1130.7%, 426.1% and 38.2% increase in perpendicular surface porosity. Moreover, a 40% increase in scan speed produced 167.7%, 849.3% and 326.1% increase in perpendicular surface porosity are the respective laser powers. Lastly, with a maintained hatch spacing of 0.14mm, a 200% increase in scan speed produced a 13.3% increase in surface porosity at 150W laser power. Furthermore, an increase of 66.7% produced 475.6%, 425.3% and 394.7% in perpendicular surface porosity at 150, 200 and 250W, respectively. An additional 40% increase in scan speed produced an increase of 177%, 237.1% and 187% in perpendicular surface porosity at 150, 200 and 250W laser power, respectively.

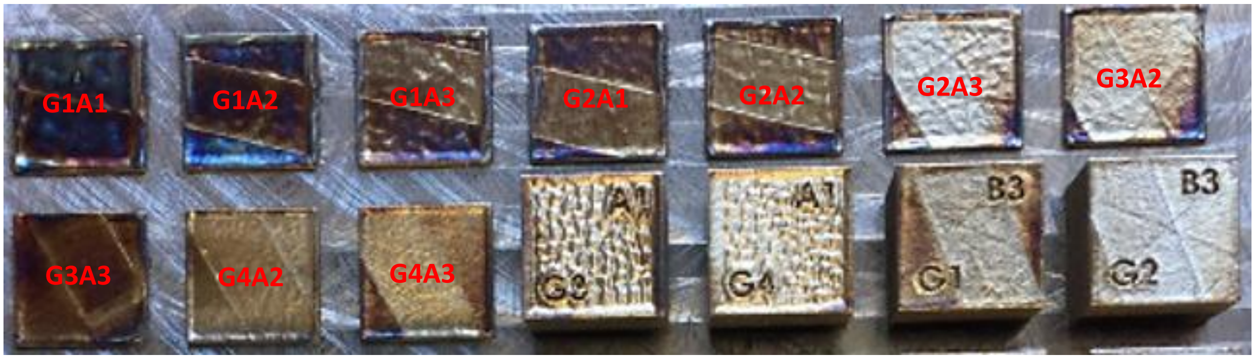

Figure 4-7. Samples in red completely burnt at low speeds

The influence of porosity to scan speed on the parallel surface is also studied. Increasing the scan speed generally resulted in a rise in parallel surface porosity. To determine the effect of scan speed on the parallel surface porosity, laser power and hatch spacing was kept constant. At a hatch spacing of 0.08mm and laser powers of 150, 200 and 250 mm/s, a 66.7% increase in the scan speed from 750mm/s to 1250mm/s produced a 1058.7% increase, 43.5% increase and 70.7% decrease in porosity at the corresponding laser powers. A further 40% increase in scan speed produced 103.3%, 29.7% and 109% increase in parallel surface porosity at 150, 200 and 250W laser power. At hatch spacing of 0.10mm and laser powers of 150, 200 and 250 mm/s, a 66.7% increase in the scan speed produced a 1986.3% increase, 160.5% increase and 77.6% decrease in surface porosity, at the respective laser powers. Similarly, a further 40% increase scan speed produced a 228.9% increase, and a 490.2% increase in parallel surface porosity at 200 and 250W, respectively. At a hatch spacing of 0.12mm, a 200% increase in scan speed from 250 to 750mm/s produced an 89.9% increase in parallel surface porosity. Similarly, an additional 66.7% increase in scan speed resulted in a 2537.8% and 48.1% increase in parallel surface porosity at 150 and 200W laser power. Moreover, a 40% increase in scan speed produced 330%and 981.1% increase in parallel surface porosity at 150 and 200Wlaser powers. Lastly, with a maintained hatch spacing of 0.14mm, an increase of 66.7% produced 10859%, 1006% and 554.3% in parallel surface porosity at 150, 200 and 250W, respectively. An additional 40% increase in scan speed produced an increase of 12.3%, 914.4% and 162.8% in parallel surface porosity at 150, 200 and 250W laser power, respectively.

Figure [4-8], shows the SEM micrographs of samples G3A1, G3B1, G3C1 and G3D1, respectively. As seen in Figure [4-8], a radical change in the size, shape and number of pores is evident with increasing scan speed. The mean pore area at 0.08mm for the G3A1 sample was 607.3µm^2 whereas, a 200% increase in scan speed produced a mean pore area of 154.8µm^2 for the G3B1. The average pore area thereby decreased by 74.5% with a 200% increase in hatch spacing. The morphology of the pore changed from circular large keyhole and gas pores in G3A1 sample to small irregular shaped lack of fusion pores in the G3B1 sample. A further 66.7% and 40% increase in scan speed produced a mean pore area of 2325.2µm^2 and 46707.5µm^2 in samples G3C1 and G3D1, respectively. This presents an increase of the average pore area by 1402.1% and 1908.8% accordingly. Thus, increasing scan speed whilst other parameters are maintained produced a general increase in average pore size as presented in Figure [4-8]. Lack of fusion pores are present at high scan speeds and increase in size as the scan speed increases. However, a drop in average pore size is observed when increasing the scan speed from 250mm/s to 750mm/s producing keyhole and gas pores at low speeds.

In summary, increasing scan speed generally increased the top surface porosity. with hatch spacing and laser power maintained, an increase in laser power resulted in an increase in surface porosity. In a nutshell, increasing laser power prompted a reduction in percent porosity whereas, a rise in scan speed and hatch spacing led to an increase in surface porosity. However, altering the hatch spacing had significant effect on the production of pores within the part.

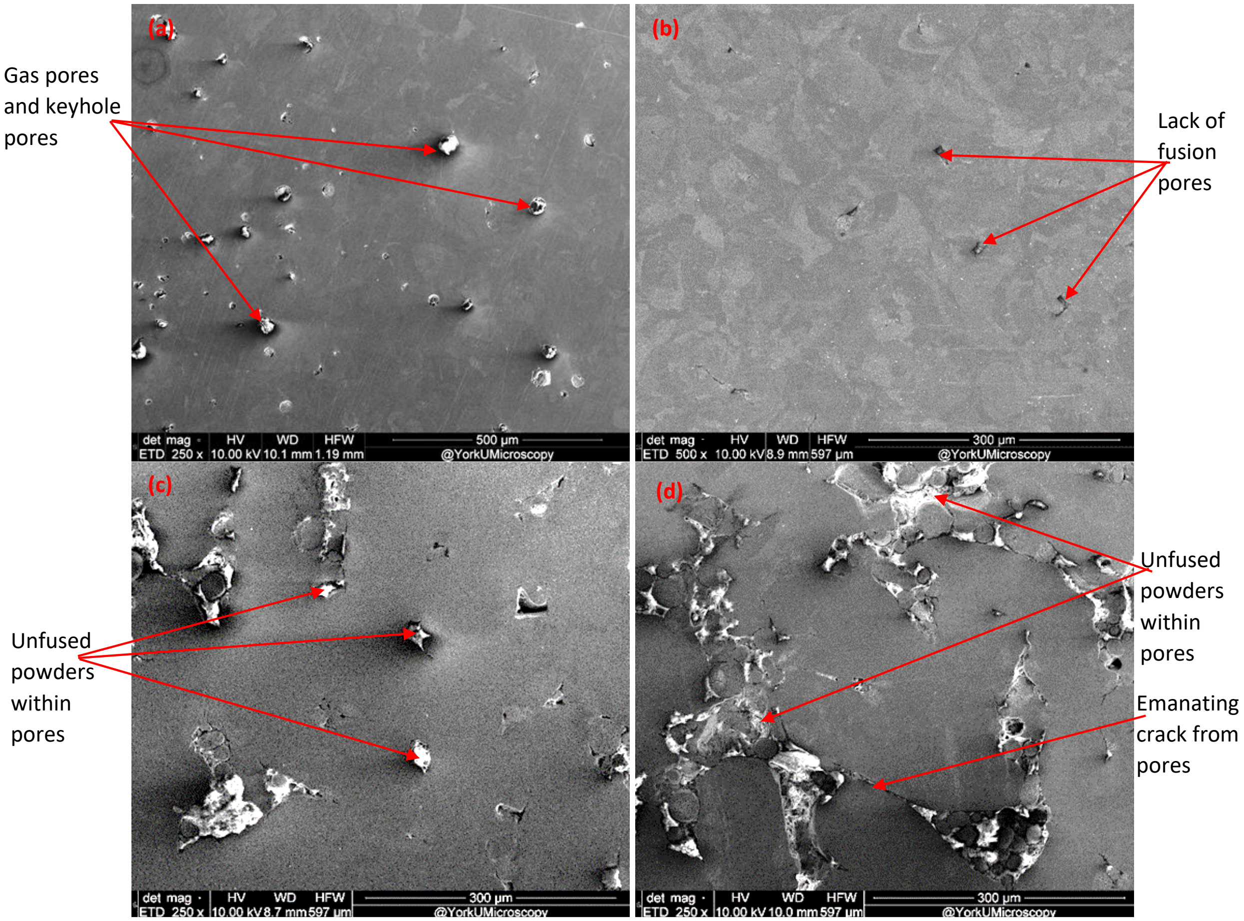

Figure 4-8. Micrographs of effect of Scan Speed on Pore shape and size at 150W Laser Power and 0.12mm Hatch Spacing a) 250 mm/s b) 750 mm/s c) 1250 mm/s d) 1750 mm/s

4.2. Influence of VED on part Density and Hardness

The data in Figure [4-9] indicates that the overall trend of increasing part density was observed with increasing volumetric energy density up to about 40J/mm^3, after which the part density was sustained within a range of 7 to 8g/cm^3. A coherent trend was observed with the percent surface porosity. However, all part densities were below the theoretical value of 7.99g/cm^3. At the lowest volumetric energy density of 20.41J/mm^3, the lowest density of 5.54g/cm^3 was recorded. An increase in volumetric energy density from 20.41 to 40 J/mm^3 resulted in an increase in part density by approximately 36.3%. However, after 40J/mm^3 the densities varied within the density range of 6.73 and 7.90g/cm^3. The highest densities of 7.88, 7.89 and 7.90g/cm^3 which were closest to the theoretical density were recorded at VEDs of 74.07, 83.33 and 138.89

J/mm^3. Hence, there is no significant correlation between part density and volumetric energy density after 40 J/mm^3. However, the densities are highest and correlate with the highly consolidated samples. mm^3

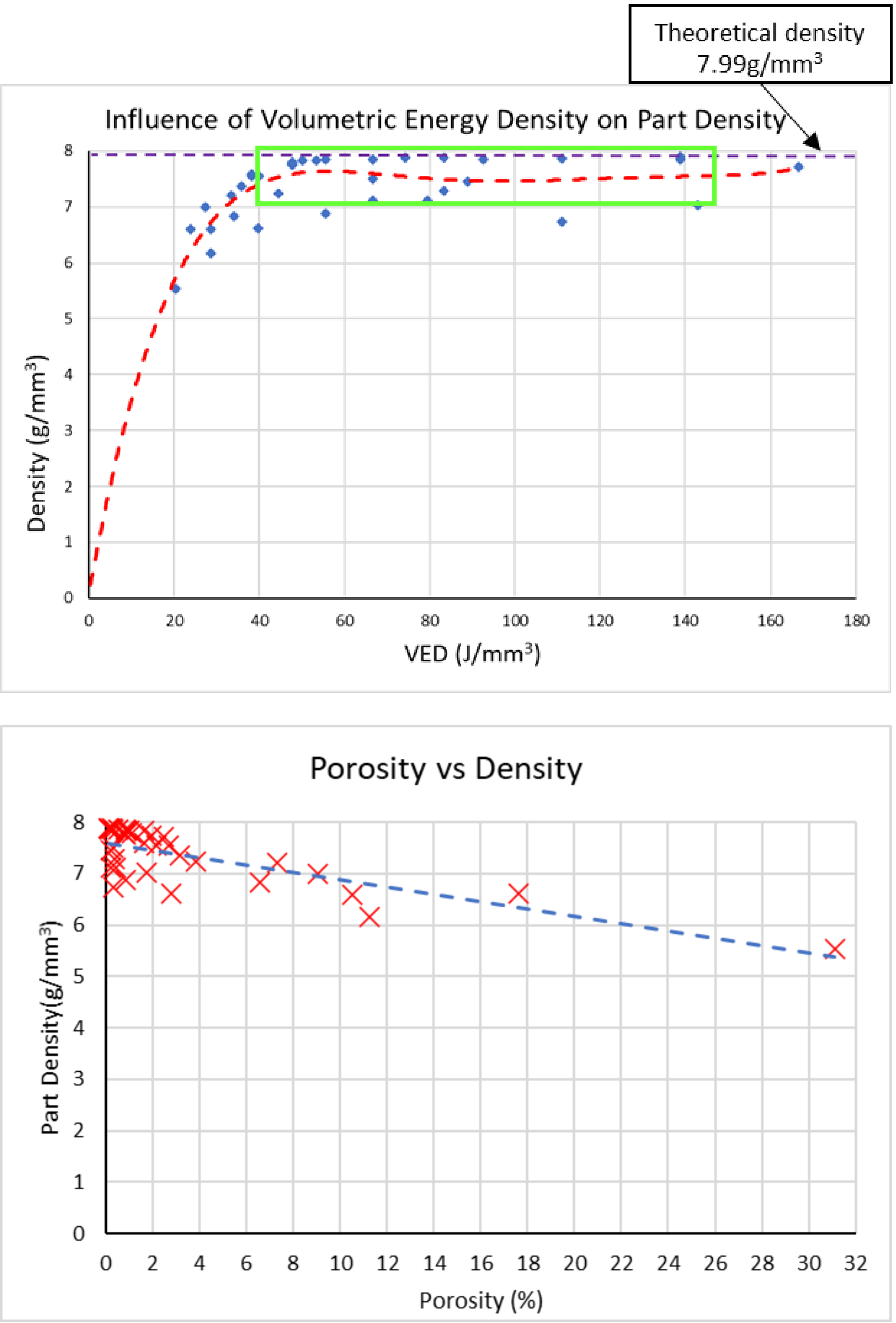

Figure 4-9. (a) Part Density as a function of VED (b) Relationship between part density and part porosity

Micro-hardness testing in additively manufactured parts is regarded as an influential method of determining mechanical isotropy within the part. The surface hardness of the samples was determined using the Vickers hardness micro-indenter. Table 4 presents the micro-hardness values of the top and side surfaces, where each value is the average of 15 measurements. The Vickers hardness of the printed samples ranged from 129.8 to 238.4HV for the top surface and ranged from 125.9 to 229.7HV for the side surface. Generally, increasing the VED leads to an increase in surface hardness as seen in Figure [4-10]. However, for both surfaces the hardness values did not vary significantly. Samples within a VED range of 20.41J/mm^3 and 40J/mm^3 had hardness values below 200HV with exception of sample G3D3. These results were consistent on both surfaces. Majority of the samples fell between 200 and 240HV for both surfaces as shown in Figure [4-10]. Sample G1B2, with a VED of 111.11J/mm^3 had the highest hardness of 238.4HV on the top surface whereas on the side surface samples G4B3 with a VED of 79.36J/mm^3 had the highest surface hardness of 229.7HV. However, sample G2B3 on the top surface with a similar VED of 111.11J/mm^3 had a lower hardness value of 210.6HV. Thus, the highest hardness values were recorded within a VED range of 44.44J/mm^3 and 142.86J/mm^3.

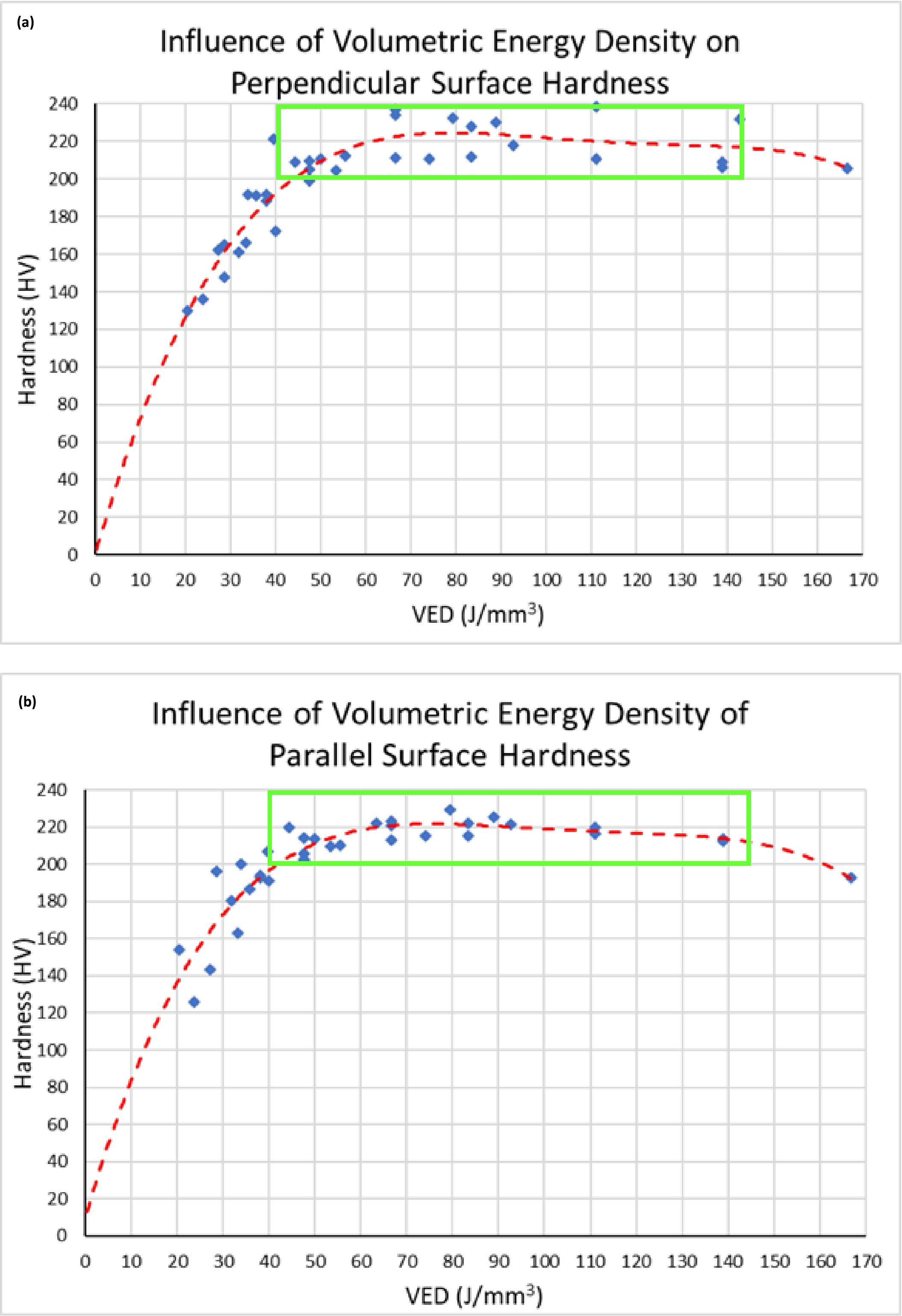

Figure 4-10. Hardness as a function of VED (a) Hardness on parallel face, (b) Hardness on perpendicular face

4.3. Effect of Print Parameters on Microstructure

It is apparent from the micrographs that the transformation of the microstructure and the defects present are because of the various printing parameters implemented. Generally, two explicit forms of microstructural features were observed on the microscale. The different microstructural features comprised of columnar lath structures and cellular structures within the grains. The printing parameters influenced the sizes and morphologies of the microstructural features. When varying the laser power alone, the hatch spacing, and scan speed are maintained. The sub-grain structures became coarser and less developed with increasing laser power as seen in Figure [4-11]. As shown in Figure [4-11a], well defined fine cellular and columnar structures were observed on the sample with parameters of 150W laser power, 0.10mm hatch spacing and 1750mm/s scan speed. However, a 33.3% increase in laser power to 200W produced less developed but thick boundary cellular structures as well as a high spatial distribution. A further 25% increase in laser power to 250W resulted in both coarse and fine cellular sub-grain structures as well as fine columnar sub-structures. The structures for samples at higher laser power were more densely packed compared to samples at lower laser power.

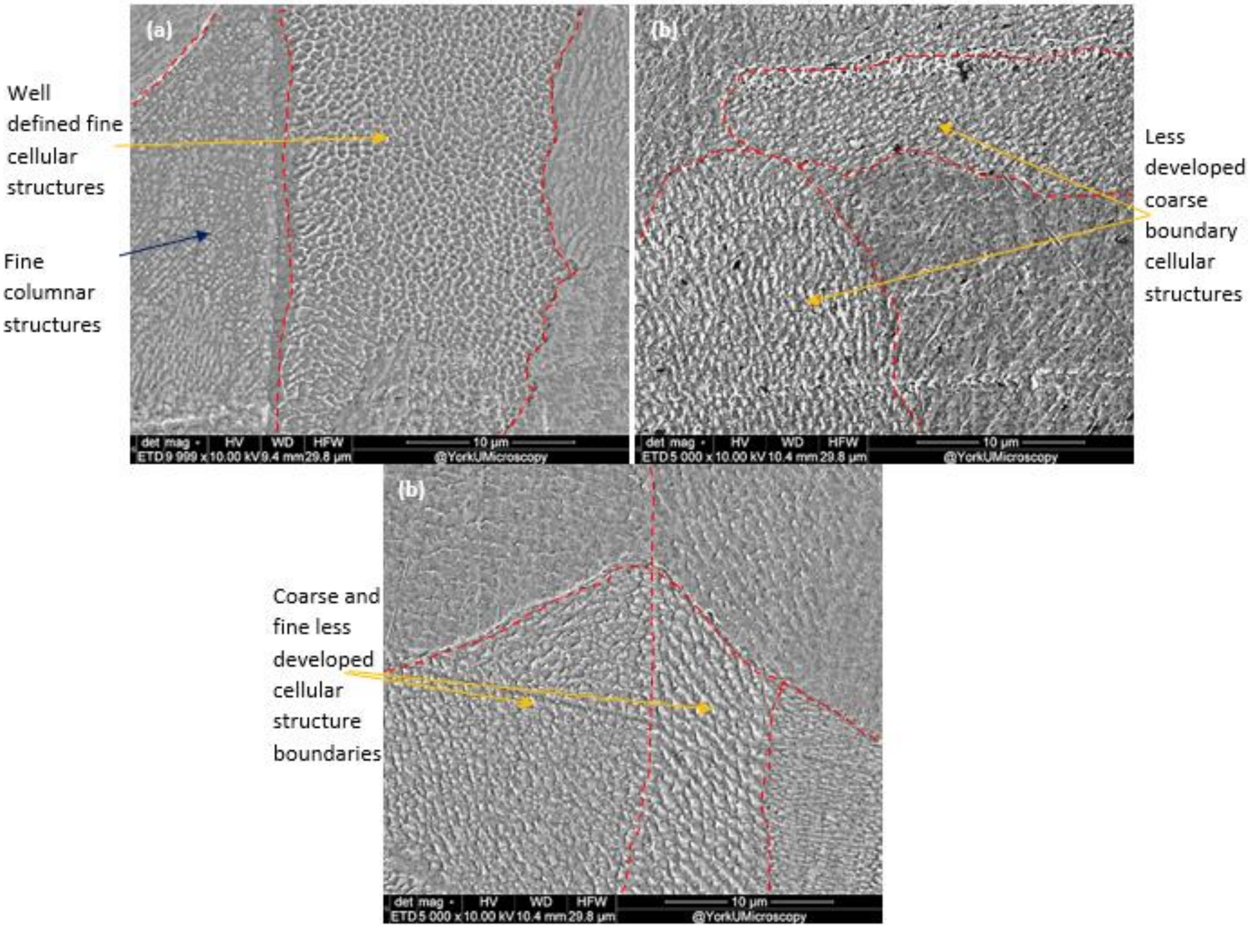

Figure 4-11. Micrographs of effect of Laser Power on Sub-grain structures at 0.10mm Hatch Spacing and 1750mm/s Scan Speed a) 150W b) 200W c) 250W

When increasing the hatch spacing, the laser power and scan speed were maintained to compare the evolved microstructures in those samples. As hatch spacing was increased the sub-grain structures became less dense and tightly packed. The progressive change in evolved microstructure due to increasing hatch spacing is shown in Figure [4-12]. At a hatch spacing of 0.08mm, fine tightly packed cellular and columnar structures were present in the microstructure. At 0.10mm hatch spacing a similar sub-grain structure was observed. There were fine tightly packed cellular sub-grain structures as well as tightly packed columnar structures. However, a higher spatial distribution was observed within the columnar structures. At 0.12mm hatch spacing, loosely packed cellular structures were observed on the sample. Furthermore, at 0.14mm hatch spacing loose and well-defined cellular structures were observed. A high spatial distribution was observed within the sub-grain substructures at high hatch spacing.

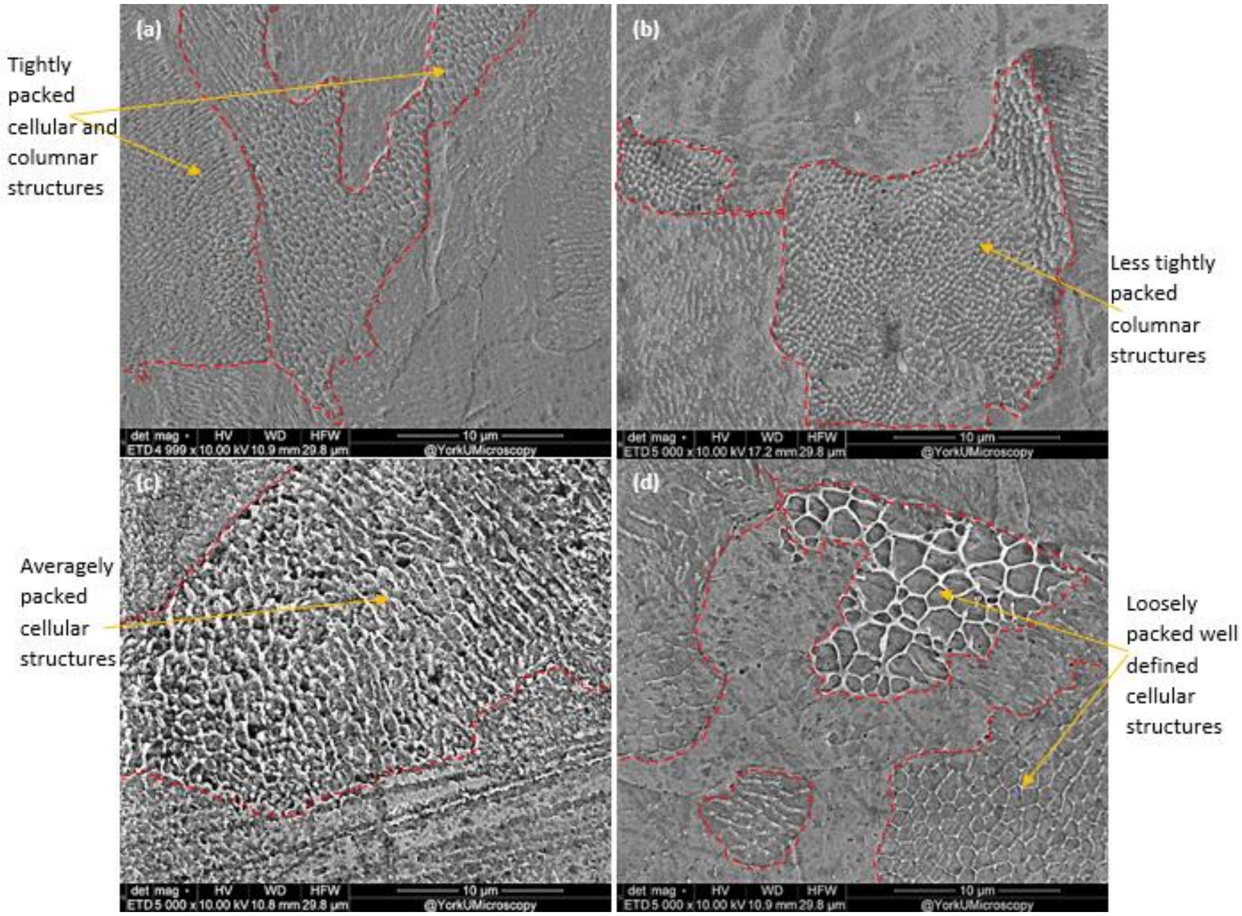

Figure 4-12. Micrographs of effect of Hatch Spacing on Sub-grain structures at 200W Laser Power and 1750mm/s Scan Speed a) 0.08 mm b) 0.10 mm c) 0.12 mm d) 0.14 mm

The scan speed was varied between 250, 750, 1250 and 1750mm/s whereas the laser power and hatch spacing was maintained. The effect of scan speeds on the microstructures are presented on Figure [4-13]. At 250mm/s scan speed, relatively coarse well defined cellular substructures as well as coarse well defined columnar sub-structures with high spatial distribution were observed. After a 200% increase in scan speed to 750mm/s, coarse less defined cellular and columnar structures with high spatial distribution were observed on the sample. However, a 66.7% increase in scan speed to 1250mm/s presented fine sub-grain structures. Densely packed well defined cellular and columnar structures were present as they had a lower spatial distribution between the sub-grain structures. Furthermore, at 1750mm/s which represents a 40% increase in scan speed, a fine less defined cellular sub-grain structures were observed. The boundaries blended into the background of the sample and became arduous to differentiate.

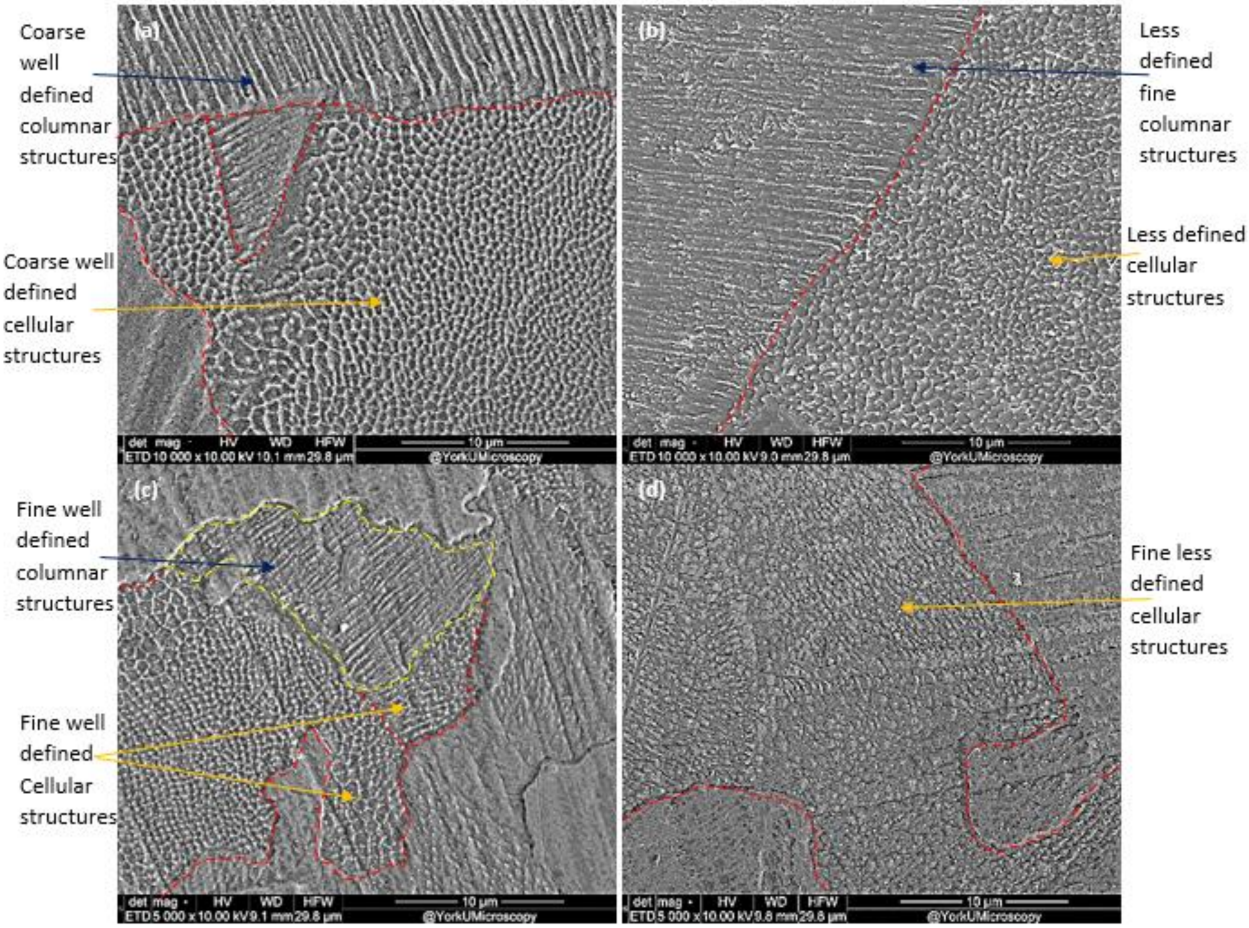

Figure 4-13. Micrographs of effect of Scan Speed on Sub-grain structures at 150W Laser Power and 0.12mm Hatch Spacing a) 250 mm/s b) 750 mm/s c) 1250 mm/s d) 1750 mm/s

4.4. Effect of Print Orientation and Parameters on impact response

4.4.1. Effect of Print Orientation on Impact response

The deformation resistance of the additively manufactured 316L SS was determined from the information presented by the LabView software. The strain gauge data was collected and converted to Voltage-time data by the LabView software and plotted as deformation resistance curves that represent how the specimen behaved during impact. The Voltage-time data was further converted into stress-strain data as shown in Figures [4-14] to [4-17]. The true stress-true strain graphs (impact resistance graphs) of specimen impacted along (perpendicular) and against (parallel) the build the direction is shown in Figure [4-14]. The results demonstrate that altering the build direction and point of impact influence the maximum strains and the maximum stress after impact. Generally, there is an initial sharp increase in flow stress and strain followed by a comparably linear rise in flow stress before reaching the maximum stress. This occurs irrespective of the build direction. Furthermore, specimen impacted in the perpendicular build direction reached a higher maximum flow stress whilst specimen impacted in the parallel build direction exhitbited a lower flow stress. Specimen impacted in the perpendicular direction presented maximum stresses in the perpendicular direction of 1635.54MPa, 1691.96MPa, 1602.58MPa, 1641.68MPa and 1586.71MPa respectively which represented a 34.8%, 30.6%, 23.2%, 22.9% and 27.5% increase when compared to maximum stresses in the perpendicular direction. Additionally, samples impacted in the perpendicular direction exhibited aproximately 33%, 33%, 41% and 20% higher strains respectively when compared to specimen impacted in the perpendicular orientation. However, specimen G1B2 demonstrated approximately 3% lower strain in the perpendicular direction when compared to the perpendicular direction.

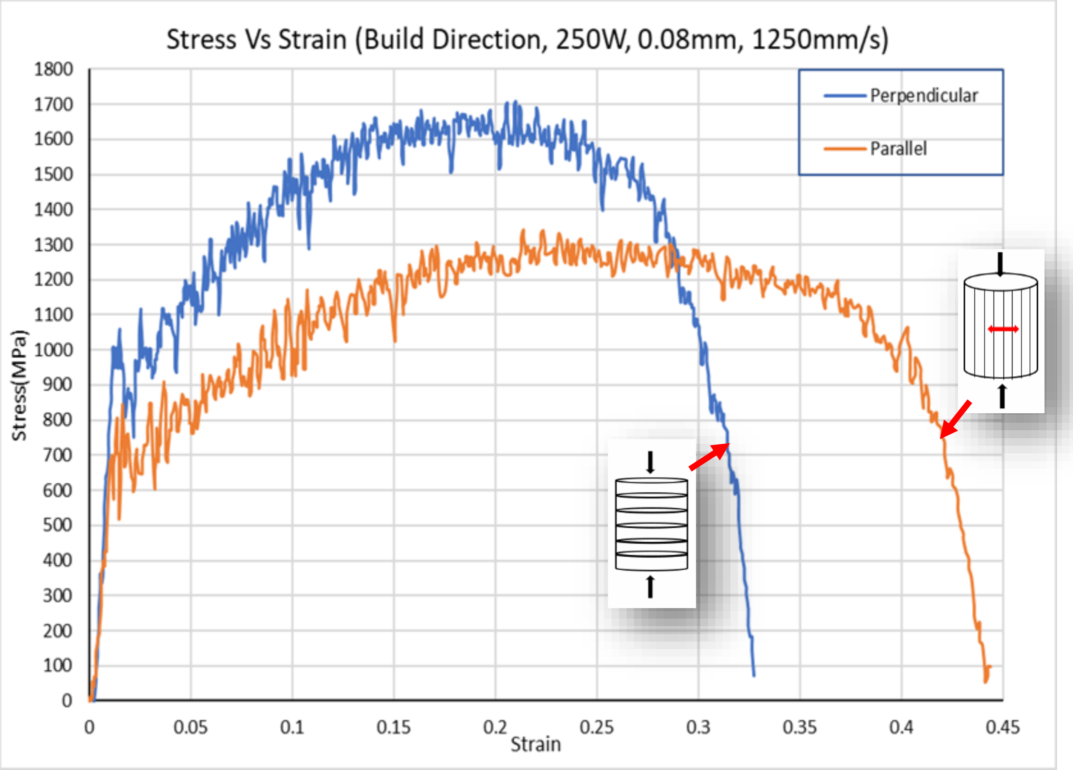
Stress Vs Strain (Build Direction, 250W, 0.08mm, 1250mm/s)
Stress(MPa)
Strain
0
100
200
300
400
500
600
700
800
900
1000
1100
1200
1300
1400
1500
1600
1700
1800
0
0.05
0.1
0.15
0.2
0.25
0.3
0.35
0.4
0.45
Perpendicular
Parallel

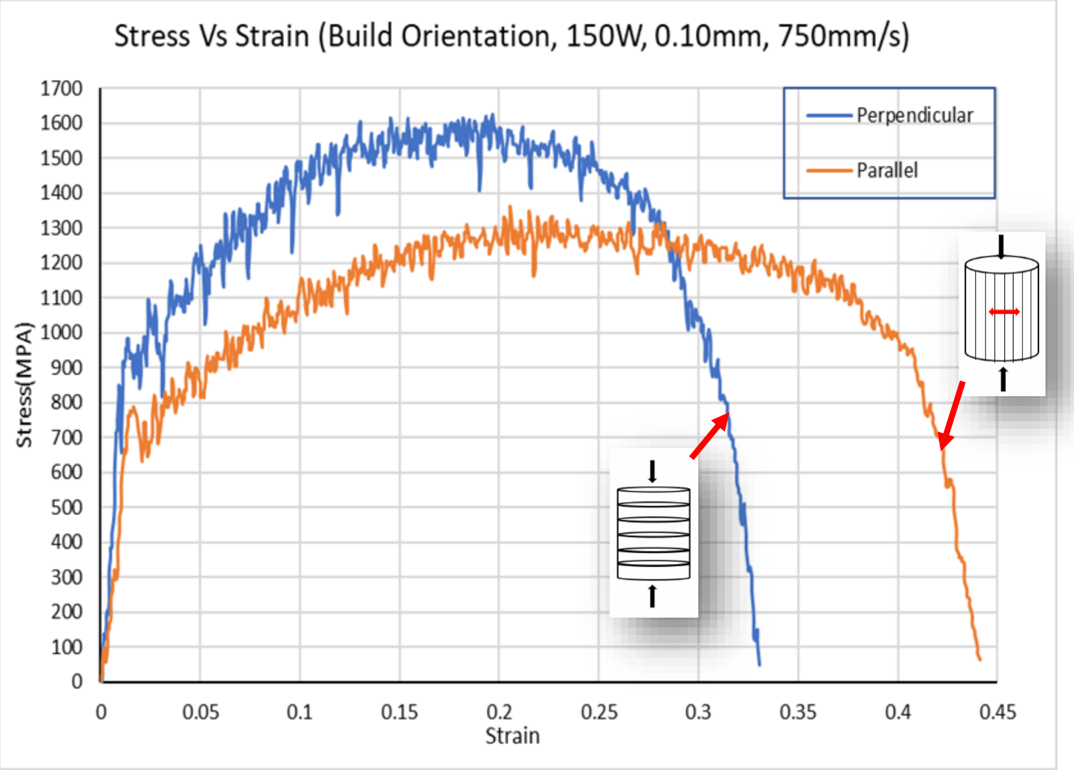
Stress Vs Strain (Build Orientation, 150W, 0.10mm, 750mm/s)
Stress(MPA)
Strain
0
100
200
300
400
500
600
700
800
900
1000
1100
1200
1300
1400
1500
1600
1700
0
0.05
0.1
0.15
0.2
0.25
0.3
0.35
0.4
0.45
Perpendicular
Parallel

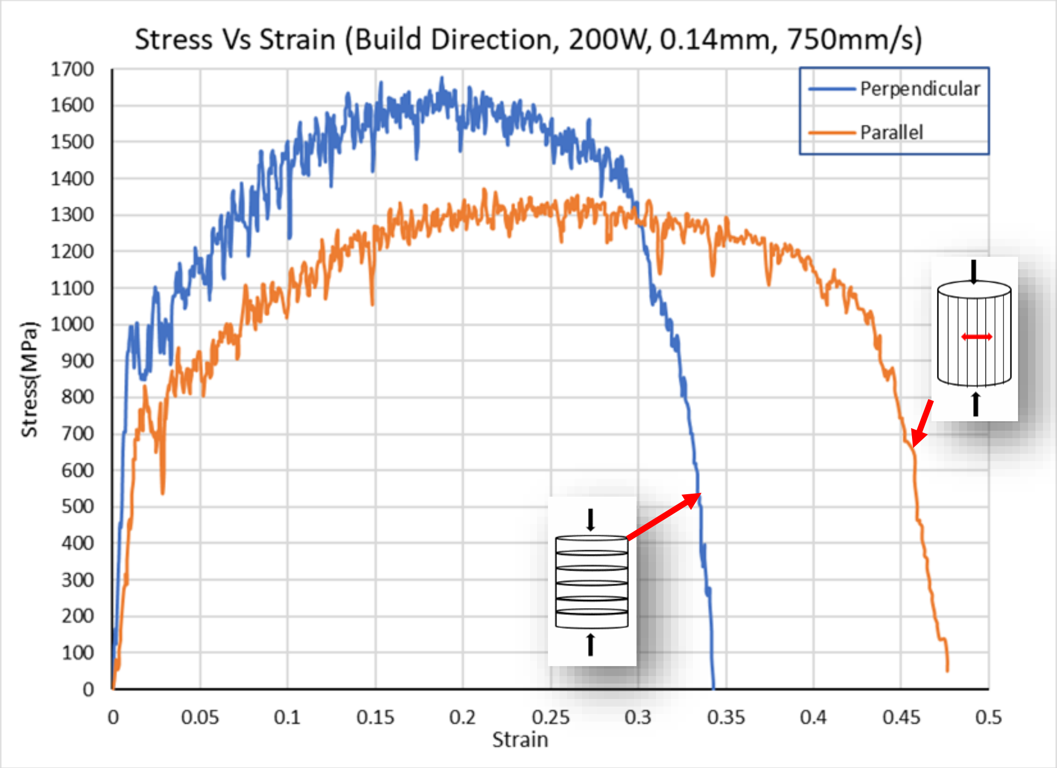

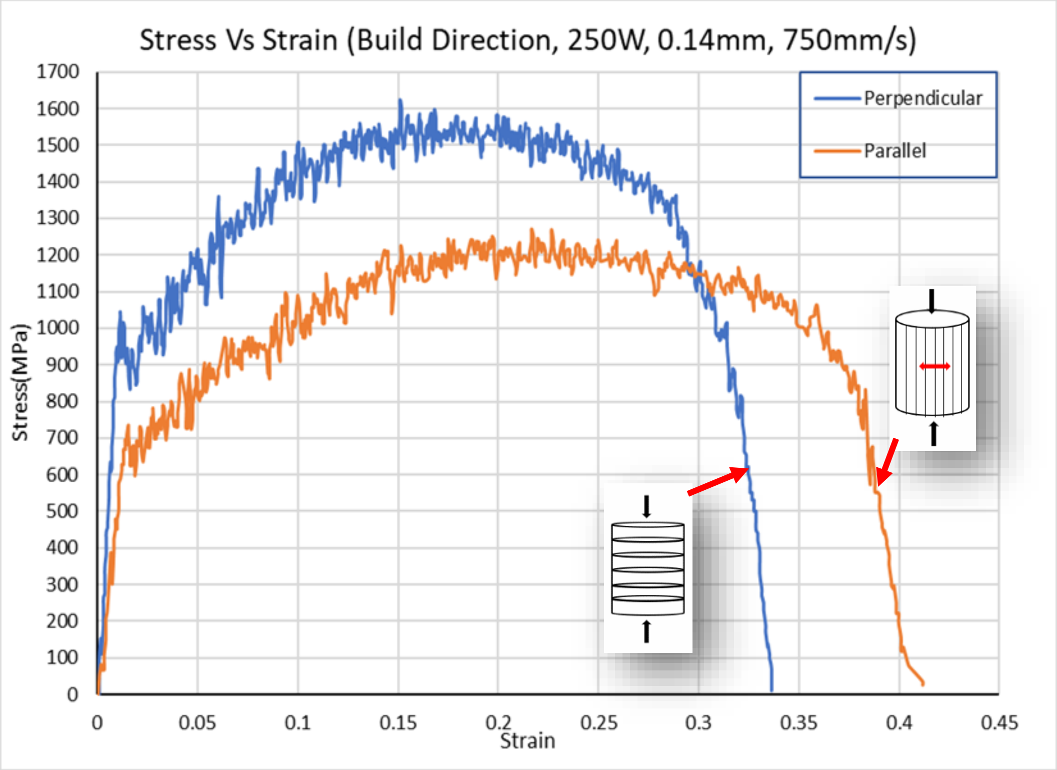

Figure 4-14: True Stress vs True Strain graphs on Orientation

4.4.2. Effect of Print parameters on impact response

The impact resistance curves from the impact assessment test are analysed to ascertain the influence the individual printing parameters have on the deformation behaviour of AM 316L parts. The first parameter to be analysed is the laser power between adjacent melt tracks. Samples fabricated with a 150W laser power showed a maximum flow stress of 1330.7MPa with a strain of 44%. Also, the strain rate recorded for this sample is 8316.6/s. Increasing the laser power by 33.3%, from 150 to 200W, resulted in a 6.3% decrease in maximum flow stress (from 1330.7MPa to 1246.2MPa) and a 9% increase in strain resulting in a more ductile behaviour. On the other hand, increasing the laser power by 25% from 200 to 250W presented a 4.9% decrease in maximum flow stress (from 1637.5MPa to 1557.2MPa). However, a 2% decrease in strain was recorded making the sample more brittle as shown in Figure [4-15].

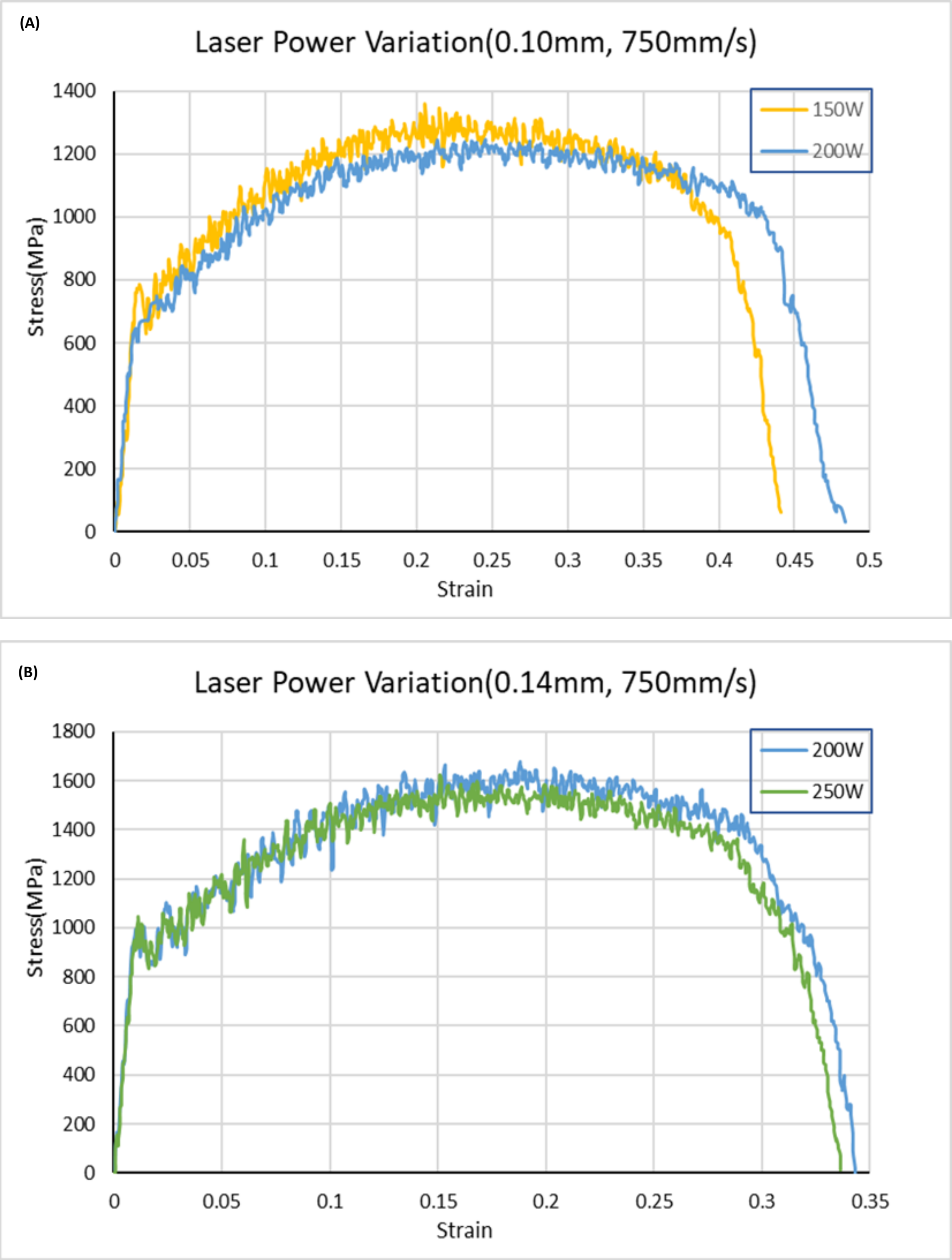

Figure 4-15. True Stress vs True Strain graphs of Laser Power Variation

The next parameter to be analysed is the hatch spacing between adjacent melt tracks. Samples fabricated with a 0.08mm hatch spacing showed a maximum flow stress of 1332.5MPa with a strain of 46%. Also, the strain rate recorded for this sample is 8786.9/s. Increasing the hatch spacing by 25%, from 0.08 to 0.10mm, resulted in a 9% decrease in maximum flow stress (from 1332.5MPa to 1216.6MPa). However, increasing the hatch spacing by 50% from 0.08 to 0.12 presented resulted in a 2.7% decrease in maximum flow stress (from 1681.8MPa to 1636.4MPa). Although, in this case, the strain recorded was a 9% higher as shown in Figure [4-16].

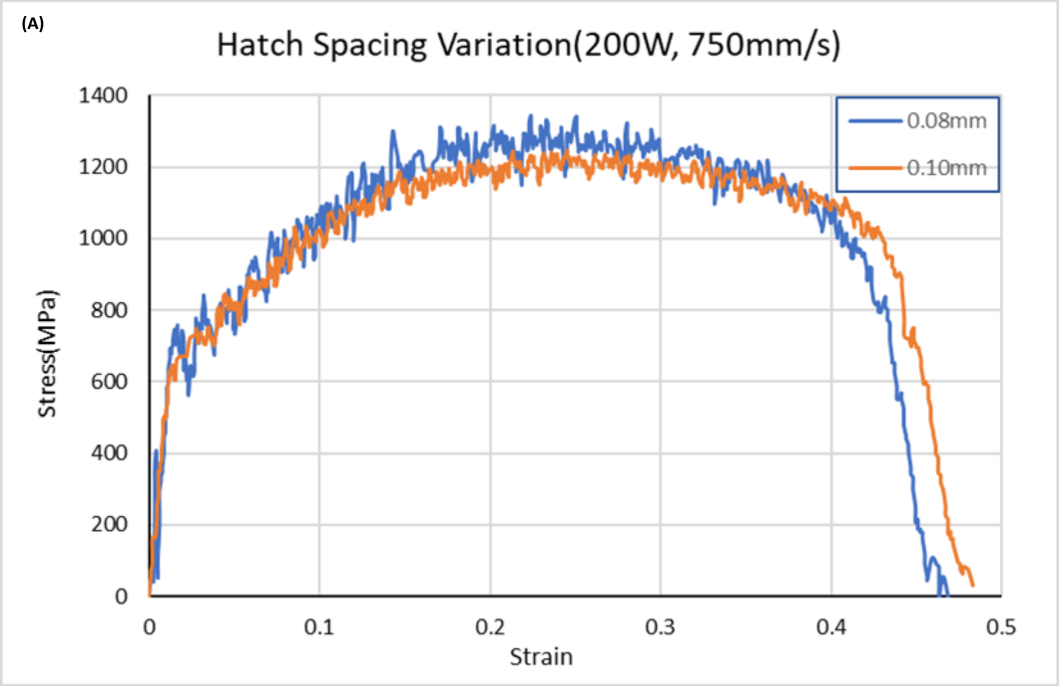

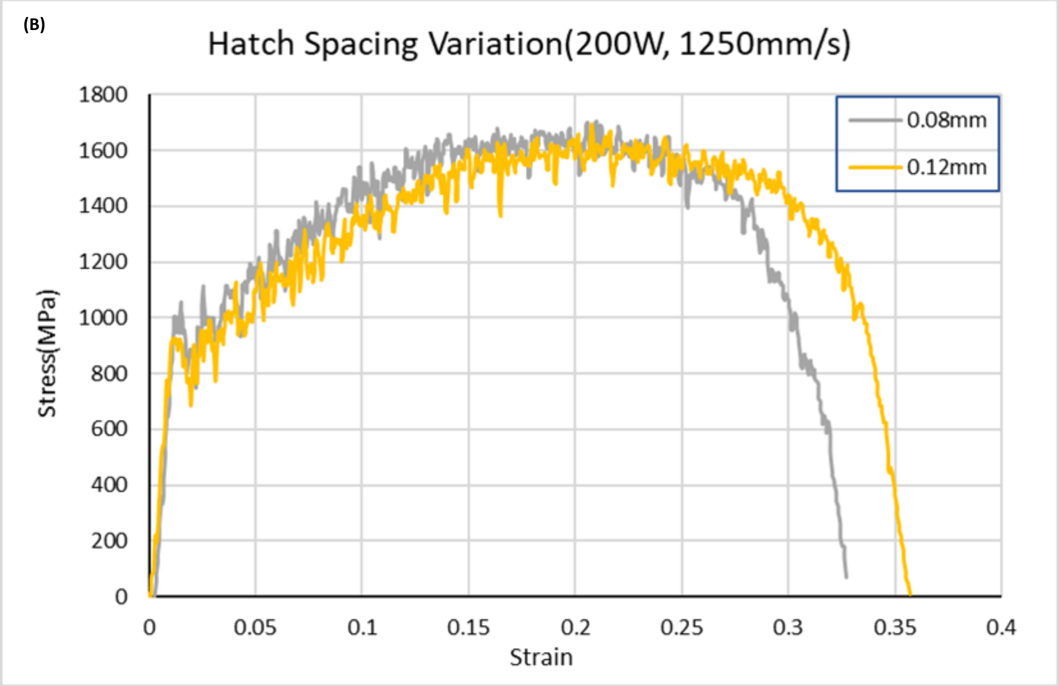

Figure 4-16. True Stress vs True Strain Graphs of Hatch Spacing Variation

Lastly, the scan speed between adjacent melt tracks is the parameter to be analysed. Increasing the scan speed by 66.7%, from 750 to 1250mm/s, resulted in a 4.7% decrease in maximum flow stress (from 1706.1MPa to 1626.5MPa) and a 7.3% increase in strain resulting in a more ductile behaviour as shown in

Figure [4-17]. The strain rates recorded for these samples are 6613.6 and 6171.3/s, respectively. While there are differences in the impact resistance curves, samples presented shear bands on their surfaces regardless of the loading orientation. However, no defects were seen to have caused the shear band failure as shown in Figure [4-18].

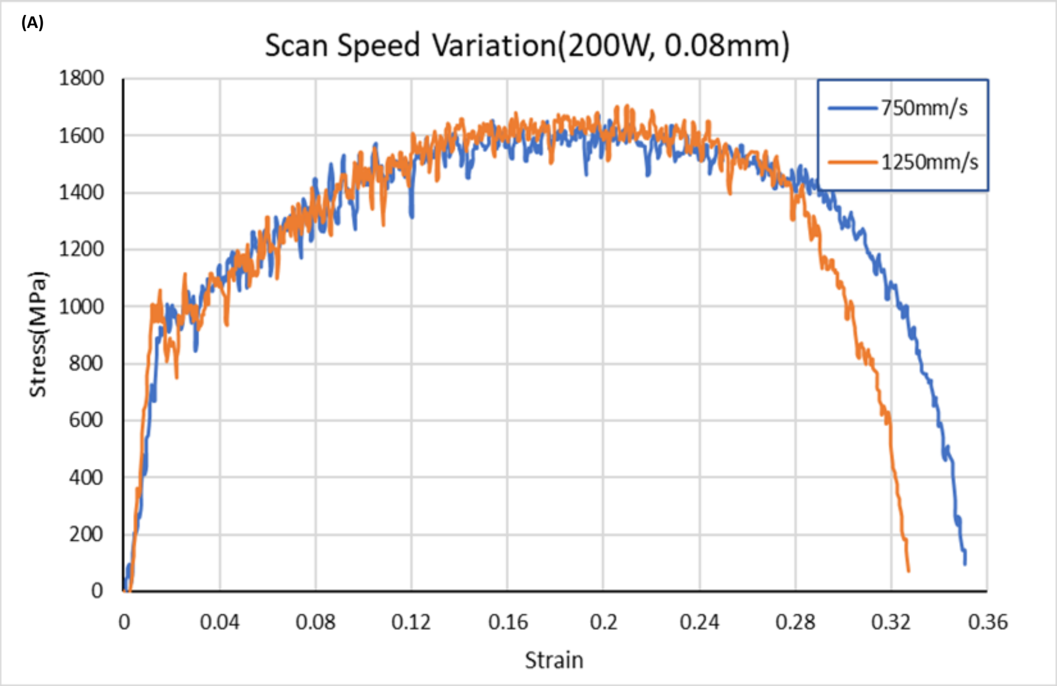

Figure 4-17. True Stress vs True Strain Graphs of Scan Speed Variation

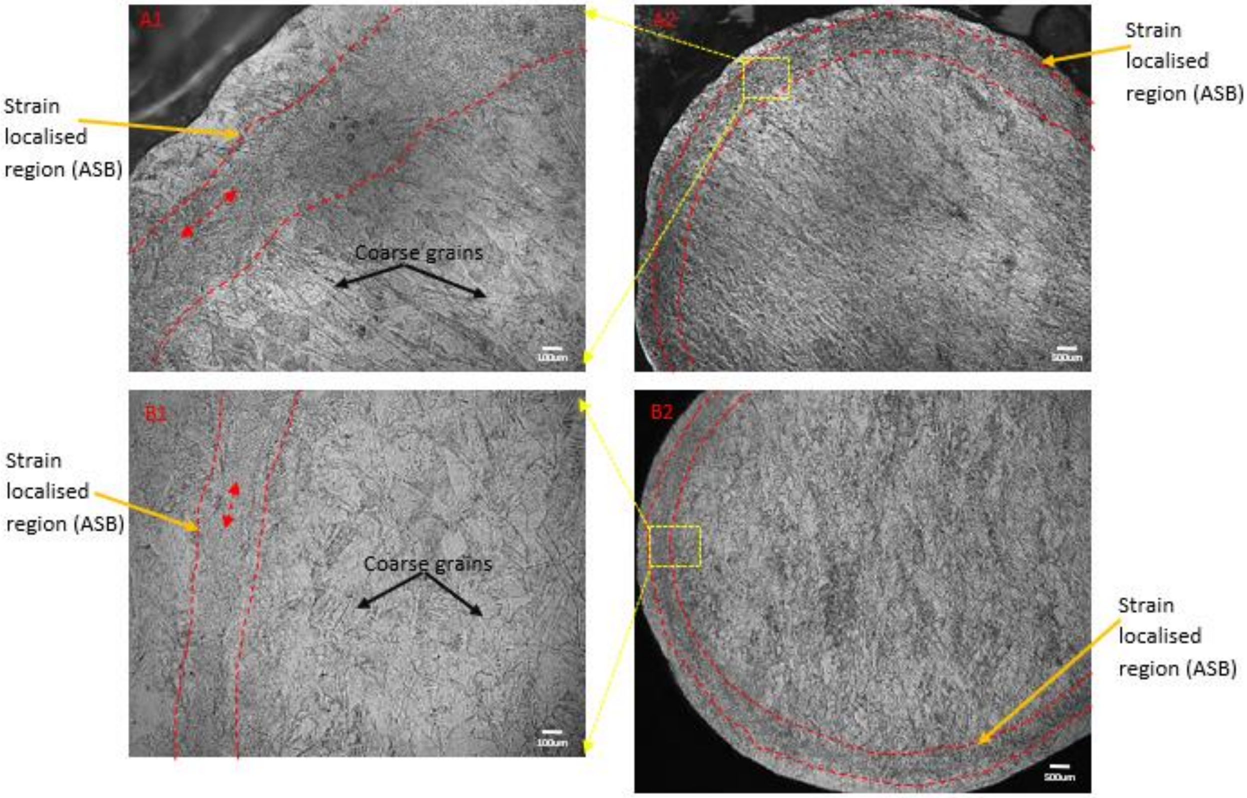

Figure 4-18. Micrographs of perpendicular orientation showing Strain localised region (ASB) with grain refinement A1-A2) G1B2, B1-B2) G2B2

5. Discussion

5.1. Effect of printing parameters on part porosity, density, and hardness

The findings in this study revealed a general trend between VED, the type of pores and the trend in void formation within SLM produced parts. In this study, lack of fusion and circular gas pores were observed in the samples. Lack of fusion pores were mostly present in samples with VED below 55.56J/mm^3 whereas keyhole or gas pores were present in samples with VED above 138J/mm^3. Lack of fusion pores were created in the samples because there was insufficient thermal energy due to low VED which caused incomplete melting of the metal powders. On the other hand, keyhole and gas pores were formed as a result of excess energy input due to high VED in those samples. In this case, vaporization of the powder material during printing created gas pores which were trapped in the melt pool during cooling process. The VED, which is a single expression, used as a fingerprint for the parts can generally be used to predict the range of porosity in the sample. However, the VED is not precise with determining the microstructural evolution. This is because material properties and the interaction between heat source was not considered [108].

Pores were in the samples reduced with increasing laser power or decreasing hatch spacing and scan speed or a combination of both. Increasing laser power resulted in higher temperatures which cause full melting of the powders creating a fully consolidated part.

A slower scan speed excessively melted the metal powder resulting in evaporation to occur, and also resulted in trapped gas which formed keyhole and gas pores within the specimen. This is similar to the observations made by Olivera et al [102]. According to Oliveira et al, [102] controlling the melt pool dynamics or reducing the local dwell times of the laser will result in a faster melt pool flow to cover or close the keyhole pores generated within the final part. Thus, a higher scan speed reduces the interaction time between the laser and the material powder bed as was observed in the current study. It was further observed a high scan speed produced a small melt pool size. A small melt pool size is caused by the low melting temperature resulting a reduction in liquid formation and lower viscosity. Due to the lower viscosity, the melt pool is prohibited from spreading and resulted in pore formation. A threshold was found to be within the 750-1250mm/s range of scan speed. However, a higher laser power input offsets the lack of interaction between the laser spot and substrate when a high hatch spacing, and scan speed is employed [103]. Li et al [103] reported, an increase in scan speed results in a decrease in melt-pool size. With this combination of parameters, a specimen with high consolidation density is possible.

It was further observed that, pores can be reduced by decreasing the hatch spacing which reduces the potential of having un-melted powders. Hatch spacing plays a crucial role in determining the extent of how the other printing parameters affect the level of porosity in the sample. At a low hatch spacing, less lack of fusion pores were produced, and a denser part is created whilst a higher hatch spacing created a less dense sample with a high number of pores. Melt tracks are either offset from each other or overlapped based on the printing conditions employed, and these conditions affected the porosity of the samples. Using a smaller hatch spacing relative to the beam spot size, as seen with a hatch spacing of 0.08mm, lead to an overlapping of melt tracks. When this condition occurs, there is re-melting of material occurring within the overlapping regions. For low hatch spacing, the overlap between adjacent scan tracks created dense specimen with less lack of fusion pores originating. This is in line with ref [104] where lower hatch spacing samples recorded high part densities. However, a high hatch spacing creates wide offsets between adjacent melt tracks which leads to regions not receiving laser radiation. As a result, these areas are filled with un-melted and unfused powders which results in a higher porosity level in the sample. In this case a higher energy input is required to create a better structure. This was confirmed by Eliasu et al, [101] when they realized that a more consolidated part was acquired at a higher hatch spacing by using a higher laser power. Also, gong et al, [105] attributed the creation of the lack of fusion pores to the surface tension effects caused by the surrounding powder in the gap between adjacent scan tracks

This study revealed the amount of pores present influenced the part density and hardness. Presence of pores in the samples resulted in lower measured hardness values because the pores create gaps in the part that easily collapse with an applied load. Consequently, parts with good consolidation and minimum number of pores showed high hardness and higher densities. A higher laser power results in full melting and better overlapping scan tracks. This was evident in this study with samples between the laser power of 200-250W presenting the lowest part porosity and higher part density. This has also been shown by Darvish et al, [106] where they showed that increasing the laser power from 180 to 220W whilst maintaining other parameters constant resulted in an increase in the average track size and also resulted in overlapping scan tracks. The overlap in scan tracks caused the lack of fusion pores to close and create highly consolidated part.

The pores of the perpendicular surface of the sample were mostly larger than the pores measured on the parallel surface of the sample. This can be attributed to weight of the printed part compressing the pores along the parallel surface, thereby creating smaller pores [107]. Also, the measurement technique for the porosity was two dimensional and did not give information on actual pore connectivity. However, the density measurement is 3-dimensional and does not compare exactly with the 2-dimensional porosity measurement.

5.2. Effect of Print Parameters on Microstructure

Lathe(columnar) and cellular structures were the two main prominent microstructural features observed in all printed specimen. The resultant microstructure was a result of the fast melting and solidification process of the manufacturing method. The thermal cycles in metal additive manufacturing led to multiple temperature changes during the printing process and created the distinct microstructure observed. In this study, a correlation between the morphology of the microstructure and the individual printing parameters were observed. It has been observed that with high laser power, slow scan speeds and high hatch spacing there is a higher amount of heat buildup. The heat build-up resulted in coarsening of the cellular and columnar microstructural features as a result of diffusion. Heat was accumulated in the melt track when a higher laser power or a low scanning speed was used. This phenomenon occurred because a fair amount of heat energy from a high laser power or slow scan speed increased the size of the melt pool. An increase in the melt pool size meant an increase in the melted powder quantity and a reduction in solidification rate within the scan track. This resulted in more heat and time to facilitate grain growth during the high temperature solidification process. As observed in Figures [4-11] and [4-13] due to higher heat build up in the sample at high laser power and slow scan speed respectively, bigger and more prominent sub-structures were observed. However, with higher scanning speed, a small melt pool size was created, resulting in fast solidification and smaller structures. This collaborates positively with findings from Zhang et al, [109]. According to Zhang et al, [109] progressively increasing scan speeds from 2, 4, 6, 8 and 10 mm/s alters the dendritic microstructure from long coarse to short fine structures. The small structures were attributed to the reduced interaction time between the laser and the substrate which results in a shallow and narrow molten pool which accelerates solidification. Therefore, there was a continuous heat deficiency producing inadequate sub-grain growth. It was also observed that at high hatch spacing, heat can be accumulated within an isolated melt track which experiences minimum energy losses to its neighbouring tracks [110]. At low hatch spacing leads to overlap between adjacent scan tracks causing heat to be easily lost to previously solidified melt tracks. At low hatch spacing and with high heat loss, fine sub-grain structures were observed. It was further observed that, increasing the hatch spacing resulted in no overlap in scan tracks, thereby reducing the rate of heat dissipation through adjacent tracks and resulting in relatively coarser sub-structures. As observed by Pavlov et al, [110] an increase in hatch spacing results in heat isolation within that scan track whereas at low hatch spacings heat is lost with adjacent scan tracks due to metallurgical contact between the melt pool. The findings of Pavlov et al [110], collaborates the findings in the current study.

5.3. Effect of Print Parameters on impact response

The mechanical properties of steels were highly dependent on the microstructure. This was confirmed in the current study. It was observed, regardless of the printing parameters used, flow stress increases gradually with increasing strain [99]. This is attributed to the dislocation movement and entanglement during the plastic deformation which results in work hardening [111].

Specimen impacted in the perpendicular build direction reached a higher maximum flow stress whilst specimen impacted in the parallel build direction exhibited a lower flow stress irrespective of the print parameters employed. It was observed that the anisotropic behaviour is mainly due to the sizes and shape of pores on the surface along the loading axis. When a surface is under loading, the pores on the surface parallel to the loading axis are compressed, thereby dictating the extent of deformation of the material as shown in Figure [5-1]. The wider the pores on the surface parallel to the loading axis, the higher the part deformations. According to Fadida et al, [93] an important parameter to be considered should be the orientation of the pores with respect to the load direction. This collaborates positively with the findings of the study. It is assumed, another factor that might have caused the anisotropic behaviour is attributed to the phenomenon known as layer band discontinuity. A tensile component of load could be present when the load was applied to the parallel surface, thereby causing layer band opening mode as reported by Waymel et al, [112]. However, the tensile component would be non-existent when the load was applied to the perpendicular surface as shown in the schematic on Figure [5-2].

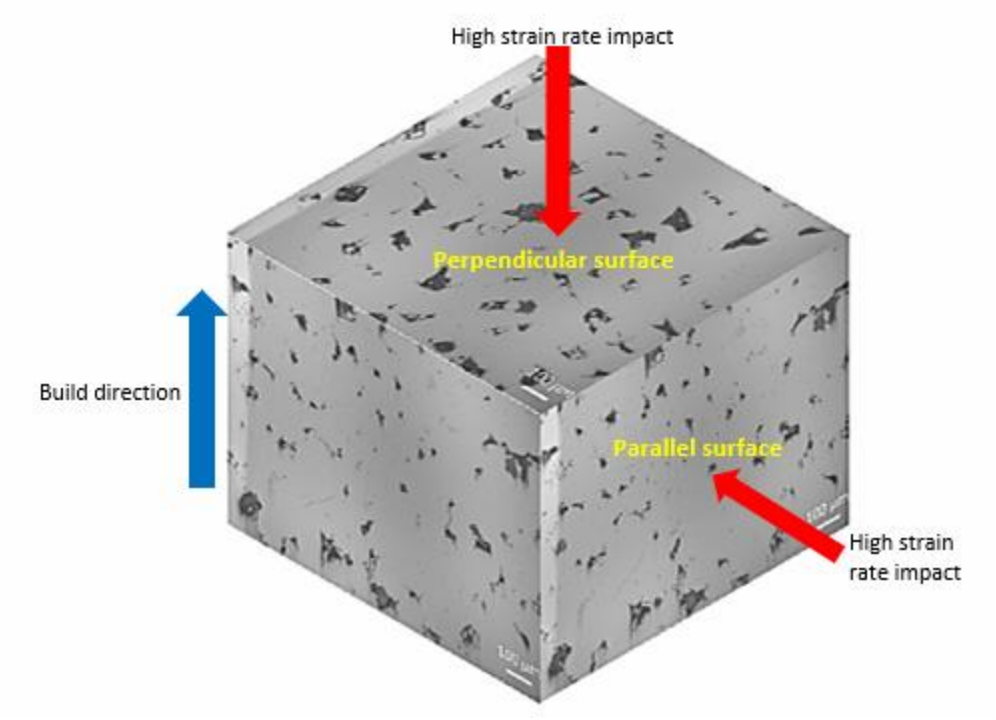

Figure 5-1. Direction of impact on Perpendicular and Parallel surface of 3d printed specimen

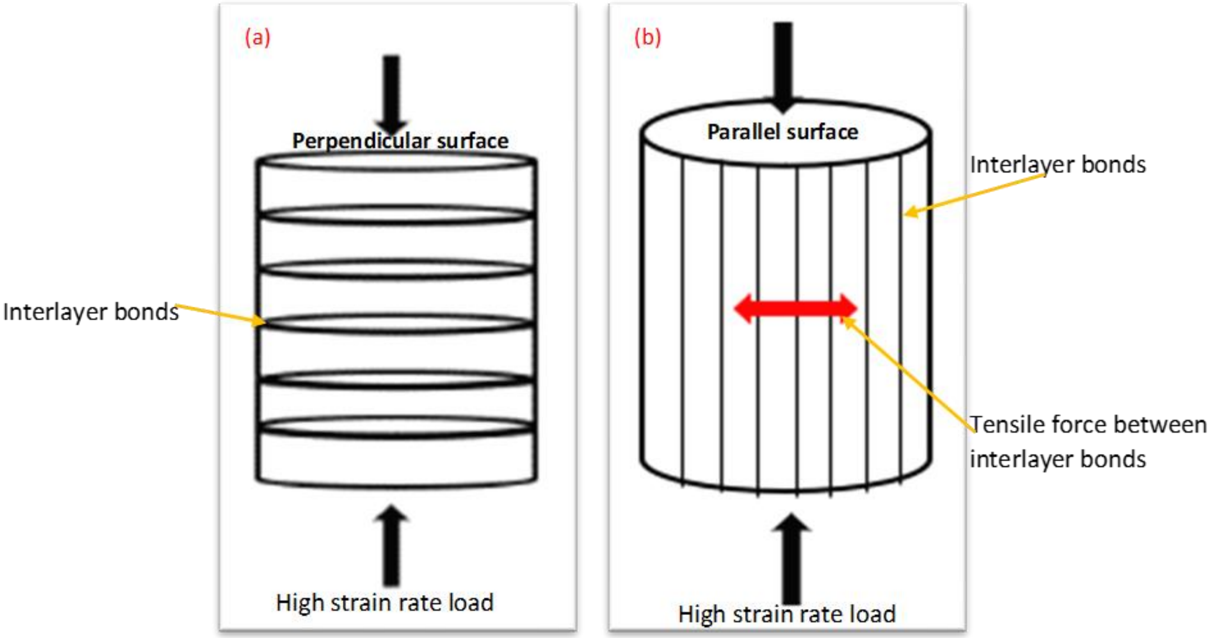

Figure 5-2. Schematic of Load on Build Orientation (a) Load on perpendicular surface, (b) Load on parallel surface

In this study, finer sub-grain structures were observed at low laser power, low hatch spacing and high scan speeds. The finer substructures observed at lower laser power, low hatch spacing and high scan speeds led to a relatively harder material as stated in the Hall-Petch formula [109]. Also, with a finer grain structure, the presence of numerous dislocation loops and entanglements led to rapid strain hardening. The pile up of dislocations and the high viscous drag were the contributing factors for the high peak stresses of the samples. In this instance, a relatively brittle behaviour with a higher peak stress and a lower strain was observed. The opposite, however, was seen with samples with coarser substructure due to the same phenomenon. In this case, the deformation energy is higher than samples with finer and fully consolidated parts [109][113]. Therefore, any printing parameters producing finer microstructures resulted in relatively high flow stress and low strain.

6. Conclusion

The originality of this work lies in the investigation of high strain rate testing on specimens based on their build orientation. The mechanical characteristics of parts produced using the Laser powder bed additive manufacturing technique is dependent on the print parameters and the direction of loading on part. Several microstructural variations are products of the different parameters employed during the production of the final part. From the study of the microstructure as well as the mechanical assessment of the 316L parts, we can conclude that:

1. The VED was a good indicator for selecting bulk physical properties such as high hardness, high density, and low porosity. A range of 44–138 J/mm^3 created good microstructure with minimum defects and enhanced mechanical behaviour.
2. The individual printing parameters gave better insight into the microstructural evolution as well as the resulting mechanical behaviour of the final parts. Increasing laser power or hatch spacing created coarser sub-grain structures whilst increasing scan speeds created fine sub-grain structures. The size of the sub-grain structure affected the mechanical response of the metal part.
3. The hatch spacing created two unique scenarios; melt track offset or melt track overlap. This dictated the range of the other parameters required to achieve a better part consolidation and performance.
4. The impact response was influenced by two factors; sub-grain structures and the number of pores present on the surface along the loading axis. A brittle behaviour, with a lower peak stress and a higher strain, was characterized by a finer substructure. On the other hand, a coarser microstructure showed a tougher resistance with a lower peak stress and a higher strain.
5. There was anisotropy in the dynamic behaviour of the samples. The perpendicular surface exhibited higher stress values than stress values recorded on the parallel surface. This can be attributed to the level of porosity on the surface parallel to the loading axis which determines the impact resistance of the samples. A higher porosity on the surface of interest results in a tougher behaviour, with

lower peak stress and higher strain. Also, interlayer bonding could create regions of high deformation.

6.1. Future Work

The effect of individual print parameters on microstructure and dynamic mechanical performance has been examined extensively in this research work. There is work still to be done to fully determine the mechanical limitations in 3D printed material. The suggested future works are presented below:

- To fully predict the regions of stress concentration during deformation tests a Digital Image Correlation (DIC) and thermal imaging system should be attached to the impact bar. This is to determine the regions of loading and shear banding during impact tests. This will aid in developing a model to determine the specific parameters and microstructures to expect for a dynamic test.
- To support adoption of 3D printing in industry without additional costs to the printing process, the effect of individual parameters and build orientation on the corrosion resistance should be further explored.

6.2. Research Contributions

- **K. Hukpati,** A. Eliasu, F.Tetteh, A.Czekanski, S.Boakye-Yiadom, (2021), Effect of Printing Parameters on the structure and properties of Additively Manufactured 316L stainless steel, *Materials Science and Engineering A (under review)*

- A.Eliasu, S.Duntu, **K.Hukpati**, M.Amegadzie, J.Agyapong, F.Tetteh, A.Czekanski, S.Boakye-Yiadom, (2021), Effect of individual printing parameters on residual stress, tribological and dynamic loading behaviour of 316L stainless steel fabricated with selective laser melting, *Materials Science and Engineering A (under review)*

- **K. Hukpati,** A. Eliasu, S.Boakye-Yiadom, A.Czekanski, (2021), Effect of Printing Parameters on Mechanical Properties of AM 316L Stainless Steel, *Canadian Society of Mechanical Engineers (CSME 2021) conference*

References

[1] S. Liu and Y. C. Shin, “Additive manufacturing of Ti6Al4V alloy: A review,” *Mater. Des.*, vol. 164, p. 107552, 2019, doi: 10.1016/j.matdes.2018.107552.

[2] A. Suárez, M. J. Tobar, A. Yáñez, and I. Pérez, “Modeling of phase transformations of Ti6Al4V during laser metal deposition,” *Phys. Procedia*, vol. 12, pp. 666–673, 2011, doi: 10.1016/j.phpro.2011.03.083.

[3] O. Abdulhameed, A. Al-ahmari, W. Ameen, and S. H. Mian, “Additive manufacturing : Challenges , trends , and applications,” *Adv. Mech. Eng.*, vol. 11(2), no. 1–27, p. 28, 2019, doi: 10.1177/1687814018822880.

[4] K. V Wong and A. Hernandez, “A Review of Additive Manufacturing,” *Int. Sch. Res. Netw.*, vol. 2012, p. 10, 2012, doi: 10.5402/2012/208760.

[5] D. Herzog, V. Seyda, E. Wycisk, and C. Emmelmann, “Acta Materialia Additive manufacturing of metals,” *Acta Mater.*, vol. 117, pp. 371–392, 2016, doi: 10.1016/j.actamat.2016.07.019.

[6] Y. Zhang, L. Wu, X. Guo, and S. Kane, “Additive manufacturing of metallic materials – a review,” *J. Mater. Eng. Perform.*, vol. 27, pp. 1–13, 2017, doi: https://doi.org/10.1007/s11665-017-2747-y.

[7] A. Eliasu, “Microstructural and Mechanical Integrity of 3D printed 316L stainless steel,” York University, 2019.

[8] D. A. D. E. Moraes, “Thermal fe analysis of powder bed fusion process: power input evaluation and parameter sensitivity,” York University, 2018.

[9] C. Weingarten, D. Buchbinder, N. Pirch, W. Meiners, K. Wissenbach, and R. Poprawe, “Journal of Materials Processing Technology Formation and reduction of hydrogen porosity during selective laser melting of AlSi10Mg,” *J. Mater. Process. Tech.*, vol. 221, pp. 112–120, 2015, doi: 10.1016/j.jmatprotec.2015.02.013.

[10] C. K. B. El-dasher, G. F. Gallegos, W. E. King, and A. Sisto, “Density of additively-manufactured , 316L SS parts using laser powder-bed fusion at powers up to 400 W,” pp. 65–78, 2014, doi: 10.1007/s00170-014-5954-9.

[11] I. Yadroitsev and I. Yadroitsau, “Selective laser melting: Direct manufacturing of 3D-objects by selective laser melting of metal powders,” *Appl. Catal. B Environ.*, vol. 75, pp. 229–238, 2009, doi: 10.1016/j.apcatb.2007.04.014.

[12] C. Kusuma, “The Effect of Laser Power and Scan Speed on Melt Pool Characteristics of Pure Titanium and Ti-6Al-4V alloy for Selective Laser Melting,” Wright State University, 2016.

[13] A. Cooke and J. Slotwinski, “Properties of Metal Powders for Additive Manufacturing: A Review of the State of the Art of Metal Powder Property Testing,” *Natl. Inst. Stand. Technol.*, vol. 1, no. IR 7873, p. 22, 2012, doi: dx.doi.org/10.6028/NIST.IR.7873.

[14] A. Mertens, *Additive manufacturing of metallic materials: an Introduction*. Elsevier Inc., 2016.

[15] W. J. Sames, F. A. List, S. Pannala, R. R. Dehoff, and S. S. Babu, “The metallurgy and processing science of metal additive manufacturing The metallurgy and processing science of metal additive manufacturing,” *Int. Mater. Rev. ISSN*, vol. 6608, p. 47, 2016, doi: 10.1080/09506608.2015.1116649.

[16] P. Jan, *UNITED STATES PATENT*. 1943.

[17] “30 years of EOS Passion for 3D Printing.” .

[18] M. Attaran, “The rise of 3-D printing : The advantages of additive manufacturing over traditional manufacturing,” *Bus. Horiz.*, vol. 1399, p. 12, 2017, doi: 10.1016/j.bushor.2017.05.011.

[19] R. E. Schafrik, D. D. Ward, and J. R. Groh, “Application of Alloy 718 in GE Aircraft Engines : Past , Present and Next Five Years,” *Mater. Sci.*, vol. 1, p. 11, 2001, doi: 10.7449/2001/SUPERALLOYS_2001_1_11.

[20] W. E. Frazier, “Metal additive manufacturing: A review,” *J. Mater. Eng. Perform.*, vol. 23, no. 6, pp. 1917–1928, 2014, doi: 10.1007/s11665-014-0958-z.

[21] J. Kranz, D. Herzog, and C. Emmelmann, “Design guidelines for laser additive manufacturing of lightweight structures in,” *J. Laser Appl.*, vol. 14001, no. 27, p. 17, 2014, doi: 10.2351/1.4885235.

[22] A. Glad and C. Gustafson, “Efficient cooling with tool inserts manufactured by electron beam melting,” *Rapid Prototyp. J.*, vol. 3, pp. 128–135, 2007, doi: 10.1108/13552540710750870.

[23] T. Duda and L. V. Raghavan, “3D Metal Printing Technology,” *IFAC-PapersOnLine*, 2016, doi: 10.1016/j.ifacol.2016.11.111.

[24] R. P. Mudge and N. R. Wald, “Laser engineered net shaping advances additive manufacturing and repair,” *Weld. J. (Miami, Fla)*, vol. 86, no. 1, pp. 44–48, 2007, doi: 137938367.

[25] M. Ziętala, T. Durejko, M. Polański, I. Kunce, and T. Płociński, “The microstructure, mechanical properties and corrosion resistance of 316 L stainless steel fabricated using laser engineered net shaping,” *Mater. Sci. Eng. A*, vol. 677, pp. 1–10, 2016, doi: 10.1016/j.msea.2016.09.028.

[26] G. N. Levy, R. Schindel, and J. P. Kruth, “Rapid manufacturing and rapid tooling with layer manufacturing (LM) technologies, state of the art and future perspectives,” *CIRP Ann. - Manuf. Technol.*, 2003, doi: 10.1016/S0007-8506(07)60206-6.

[27] A. Hehr, J. Wenning, K. Terrani, S. S. Babu, and M. Norfolk, “Five-Axis Ultrasonic Additive Manufacturing for Nuclear Component Manufacture,” *Jom*, vol. 69, no. 3, pp. 485–490, 2017, doi: 10.1007/s11837-016-2205-6.

[28] T. Debroy, H. L. Wei, J. S. Zuback, T. Mukherjee, and J. W. Elmer, “Progress in Materials Science Additive manufacturing of metallic components – Process , structure and properties,” *Prog. Mater. Sci.*, vol. 92, pp. 112–224, 2018, doi: doi.org/10.1016/j.pmatsci.2017.10.001.

[29] T. Kurzynowski, K. Gruber, W. Stopyra, and E. Chlebus, “A Correlation between process parameters , microstructure and properties of 316 L stainless steel processed by selective laser melting,” *Mater. Sci. Eng. A*, vol. 718, no. December 2017, pp. 64–73, 2018, doi: 10.1016/j.msea.2018.01.103.

[30] Y. Zhang *et al.*, “Additive Manufacturing of Metallic Materials: A Review,” *J. Mater. Eng. Perform.*, vol. 27, no. 1, pp. 1–13, 2017, doi: 10.1007/s11665-017-2747.

[31] S. M. Yusuf, S. Cutler, and N. Gao, “Review : The Impact of Metal Additive Manufacturing on the Aerospace Industry,” *Metals (Basel).*, vol. 9, no. 12, p. 35, 2019, doi: 10.3390/met9121286.

[32] S. Masurtschak, R. J. Friel, A. Gillner, J. Ryll, and R. A. Harris, “Fiber laser induced surface modification/manipulation of an ultrasonically consolidated metal matrix,” *J. Mater. Process. Technol.*, vol. 213, no. 10, pp. 1792–1800, 2013, doi: 10.1016/j.jmatprotec.2013.04.008.

[33] F. Jose, M. Rivera, A. Jose, and R. Arciniegas, “Additive manufacturing methods : techniques , materials , and closed-loop control applications,” *Int. J. Adv. Manuf. Technol.*, vol. 109, pp. 17–31, 2020, doi: doi.org/10.1007/s00170-020-05663-6.

[34] J. Agyapong, “Additive manufacturing of novel cemented carbides with self lubricating properties,” York University, 2019.

[35] I. Yadroitsev, *Selective laser melting : Direct manufacturing of 3D-objects by selective laser melting of metal powders*. 2009.

[36] D. Gu, Y. C. Hagedorn, W. Meiners, G. Meng, and R. J. S. Batista, “Densification behavior, microstructure evolution, and wear performance of selective laser melting processed commercially pure titanium,” *Acta Mater.*, vol. 60, no. 9, pp. 3849–3860, 2012, doi: 10.1016/j.actamat.2012.04.006.

[37] R. Li, Y. Shi, Z. Wang, L. Wang, J. Liu, and W. Jiang, “Densification behavior of gas and water atomized 316L stainless steel powder during selective laser melting,” *Appl. Surf. Sci.*, vol. 256, no. 13, pp. 4350–4356, 2010, doi: 10.1016/j.apsusc.2010.02.030.

[38] L. Chen, Y. He, Y. Yang, S. Niu, and H. Ren, “The research status and development trend of additive manufacturing technology,” *Int J Adv Manuf Technol*, vol. 89, pp. 3651–3660, 2016, doi: 10.1007/s00170-016-9335-4.

[39] R. Faullant, “3D printing for incumbent firms and entrepreneurs,” 2016.

[40] W. E. King, H. D. Barth, V. M. Castillo, G. F. Gallegos, and J. W. Gibbs, “Observation of keyhole-mode laser melting in laser powder-bed fusion additive manufacturing,” *J. Mater. Process. Tech.*, vol. 214, no. 12, pp. 2915–2925, 2014, doi: 10.1016/j.jmatprotec.2014.06.005.

[41] Z. Y. Liu, P. Stief, J. Dantan, A. Etienne, and A. Siadat, “Residual Stress in Metal Additive Manufacturing,” 2018, pp. 348–353, doi: 10.1016/j.procir.2018.05.039.

[42] P. J. Withers and H. K. D. H. Bhadeshia, “Residual stress Part 1 – Measurement techniques,” *Mater. Sci. Technol.*, vol. 17, pp. 355–365, 2001.

[43] A. S. Wu, D. W. Brown, M. Kumar, G. F. Gallegos, and W. E. King, “An Experimental Investigation into Additive Manufacturing- Induced Residual Stresses in 316L Stainless Steel,” *Miner. Met. Mater. Soc. ASM Int.*, vol. 6260, p. 11, 2014, doi: 10.1007/s11661-014-2549-x.

[44] J. Kruth, J. Deckers, E. Yasa, and R. Wauthle, “Assessing and comparing influencing factors of residual stresses in selective laser melting using a novel analysis method,” *SAGE Journals*, vol. 226, no. 6, pp. 980–991, 2012, doi: 10.1177/0954405412437085.

[45] I. Yadroitsev and I. Yadroitsava, “Evaluation of residual stress in stainless steel 316L and Ti6Al4V samples produced by selective laser melting,” *Virtual Phys. Prototyp.*, vol. 10, no. 2, pp. 67–76, 2015, doi: 10.1080/17452759.2015.1026045.

[46] B. Song, X. Zhao, S. Li, C. Han, and Q. Wei, “Differences in microstructure and properties between selective laser melting and traditional manufacturing for fabrication of metal parts : A review,” *Front. Mech. Eng.*, vol. 10, no. 2, pp. 111–125, 2015, doi: 10.1007/s11465-015-0341-2.

[47] L. Facchini, N. V. Jr, I. Lonardelli, E. Magalini, P. Robotti, and A. Molinari, “Metastable Austenite in 17–4 Precipitation-Hardening Stainless Steel Produced by Selective Laser Melting,” *Adv. Eng. Mater.*, vol. 12, pp. 184–188, 2010, doi: 10.1002/adem.200900259 Metastable.

[48] P. G. E. Jerrard, L. Hao, K. E. Evans, and A. Technologies, “Experimental investigation into

selective laser melting of austenitic and martensitic stainless steel powder mixtures," *Adv. Technol. Res. Inst.*, vol. 223, pp. 1409–1416, 2009, doi: 10.1243/09544054JEM1574.

[49] R. Saluja, "The emphasis of phase transformations and alloying constituents on hot cracking susceptibility of type 304L and 316L stainless steel welds," *Int. J. Eng. Sci. Technol.*, vol. 4, no. 05, pp. 2206–2216, 2012, doi: 38846836.

[50] Z. Wang, T. A. Palmer, and A. M. Beese, "Acta Materialia Effect of processing parameters on microstructure and tensile properties of austenitic stainless steel 304L made by directed energy deposition additive manufacturing," *Acta Mater.*, vol. 110, pp. 226–235, 2016, doi: 10.1016/j.actamat.2016.03.019.

[51] J. S. Zuback and T. Debroy, "The Hardness of Additively Manufactured Alloys," *Materials (Basel).*, vol. 11, p. 2070, 2018, doi: 10.3390/ma11112070.

[52] X. Chen, J. Li, X. Cheng, B. He, H. Wang, and Z. Huang, "A Microstructure and mechanical properties of the austenitic stainless steel 316L fabricated by gas metal arc additive manufacturing," *Mater. Sci. Eng. A*, vol. 703, pp. 567–577, 2017, doi: 10.1016/j.msea.2017.05.024.

[53] L. Thijs, K. Kempen, J. Kruth, and J. Van Humbeeck, "Fine-structured aluminium products with controllable texture by selective laser melting of pre-alloyed AlSi10Mg powder," *Acta Mater.*, vol. 61, no. 5, pp. 1809–1819, 2013, doi: 10.1016/j.actamat.2012.11.052.

[54] X. Chen, J. Li, X. Cheng, H. Wang, and Z. Huang, "Effect of heat treatment on microstructure , mechanical and corrosion properties of austenitic stainless steel 316L using arc additive manufacturing," *Mater. Sci. Eng.*, vol. 715, no. 2017, pp. 307–314, 2018, doi: doi.org/10.1016/j.msea.2017.10.002.

[55] S. Singh, S. Ramakrishna, and R. Singh, "Material issues in additive manufacturing: A review," *J. Manuf. Process.*, vol. 25, pp. 185–200, 2017, doi: 10.1016/j.jmapro.2016.11.006.

[56] S. M. Yusuf and N. Gao, "Influence of energy density on metallurgy and properties in metal additive manufacturing," *Mater. Sci. Technol.*, vol. 0836, p. 22, 2017, doi: 10.1080/02670836.2017.1289444.

[57] T. De Terris, O. Castelnau, Z. Hadjem-hamouche, H. Haddadi, V. Michel, and P. Peyre, "Analysis of As-Built Microstructures and Recrystallization Phenomena on Inconel 625 Alloy Obtained via Laser Powder Bed Fusion (L-PBF)," *Metals (Basel).*, vol. 11, p. 619, 2021, doi: 10.3390/met11040619.

[58] S. A. Khairallah, A. T. Anderson, A. Rubenchik, and W. E. King, "Laser powder-bed fusion additive manufacturing : Physics of complex melt flow and formation mechanisms of pores , spatter , and denudation zones," *Acta Mater.*, vol. 108, pp. 36–45, 2016, doi: 10.1016/j.actamat.2016.02.014.

[59] E. Yasa and J. Kruth, "Microstructural investigation of Selective Laser Melting 316L stainless steel parts exposed to laser re-melting," *Procedia Eng.*, vol. 19, pp. 389–395, 2012, doi: 10.1016/j.proeng.2011.11.130.

[60] M. Yakout, M. A. Elbestawi, and S. C. Veldhuis, "Density and mechanical properties in selective laser melting of Invar 36 and stainless steel 316L," *J. Mater. Process. Tech.*, vol. 266, pp. 397–420, 2019, doi: 10.1016/j.jmatprotec.2018.11.006.

[61] Z. Sun, X. Tan, S. Tor, and W. Y. Yeong, "Selective laser melting of stainless steel 316L with low porosity and high build rates," *JMADE*, vol. 104, pp. 197–204, 2016, doi:

10.1016/j.matdes.2016.05.035.

[62] C. Qiu, C. Panwisawas, M. Ward, H. C. Basoalto, J. W. Brooks, and M. M. Attallah, “On the role of melt flow into the surface structure and porosity development during selective laser melting,” *Acta Mater.*, vol. 96, pp. 72–79, 2015, doi: 10.1016/j.actamat.2015.06.004.

[63] R. Penn, “3D printing of 316L stainless steel and its effect on microstructure and mechanical properties,” Montana Tech, 2017.

[64] J. A. Cherry, H. M. Davies, S. Mehmood, and N. P. Lavery, “Investigation into the effect of process parameters on microstructural and physical properties of 316L stainless steel parts by selective laser melting,” *Int. J. Adv. Manuf. Technol.*, pp. 869–879, 2015, doi: 10.1007/s00170-014-6297-2.

[65] AZoM, *Stainless Steel - Grade 316L - Properties , Fabrication and Applications (UNS S31603)*. 2004.

[66] E. Liverani, S. Toschi, L. Ceschini, and A. Fortunato, “E ff ect of selective laser melting (SLM) process parameters on microstructure and mechanical properties of 316L austenitic stainless steel,” *J. Mater. Process. Tech.*, vol. 249, no. June, pp. 255–263, 2017, doi: 10.1016/j.jmatprotec.2017.05.042.

[67] J. Yamamoto, “Design-relevant mechanical properties of 3164ype steels for superconducting magnets,” *Elsevier Sci.*, vol. 37, pp. 533–550, 1997, doi: SOOll-2275(97)00071-4.

[68] W. Callister and D. Rethwisch, *Materials Science and Engineering*. 2013.

[69] C.-C. Hsieh and W. Wu, “Overview of Intermetallic Sigma (σ) Phase Precipitation in Stainless Steels.pdf,” *Int. Sch. Res. Netw.*, vol. 2012, p. 16, 2012, doi: 10.5402/2012/732471.

[70] M. A. Belsvik, “Specification of resulting microstructure from additive manufacturing by Direct Laser Deposition of SS316L-Si on stainless steel base materials,” Universiteteti Stavanger, 2018.

[71] O. K. von Goldbeck, *Iron-Chromium Fe-Cr IRON—Binary Phase Diagrams*. 1982.

[72] J. H. Potgieter, P. A. Olubambi, L. Cornish, C. N. Machio, and E. M. Sherif, “Influence of nickel additions on the corrosion behaviour of low nitrogen 22 % Cr series duplex stainless steels,” *Corros. Sci. 50*, vol. 50, pp. 2572–2579, 2008, doi: 10.1016/j.corsci.2008.05.023.

[73] Outokumpu, *Handbook of Stainless Steel*. 2013.

[74] H. B. Pereira, Z. Panossian, I. P. Baptista, C. Roberto, D. F. Azevedo, and R. De Janeiro, “Investigation of Stress Corrosion Cracking of Austenitic , Duplex and Super Duplex Stainless Steels under Drop Evaporation Test using Synthetic Seawater,” *Mater. Res.*, vol. 22, pp. 5–8, 2019, doi: 10.1590/1980-5373-MR-2018-0211.

[75] L. W. Meyer, “Material Behaviour at High Strain Rates,” 2004.

[76] R. F. Laubscher, “An Evaluation of strain rate sensitivity of certain stainless steels,” Rand Afrikaans University, 1997.

[77] S. Boakye-yiadom, “Effect of Heat Treatment on Stability of Adiabatic Shear Bands in 4340 Steel,” University of Manitoba, 2010.

[78] H. Couque, “The use of the direct impact Hopkinson pressure bar technique to describe thermally activated and viscous regimes of metallic materials Subject Areas :,” *Philos. Trans. R. Soc. A Math. Phys. Eng. Sci.*, vol. 372, p. 10, 2014, doi: 10.1098/rsta.2013.0218.

[79] K. Kuelper, “Dynamic mechanical response of additively manufactured 316L and AlSi10Mg,” Montana Tech, 2019.

[80] F. L. Pellet, V. K. Dang, C. Baumont, M. Dusseux, and G. J. Huang, “Determination of dynamic rock strength to assess blasting efficiency,” 2013, p. 7.

[81] U. F. Kocks, “Kinetics of solution hardening,” *Metall. Trans. A*, vol. 16, pp. 2109–2129, 1985, doi: 10.1007/BF02670415.

[82] G. T. (Rusty) Gray, “High-Strain-Rate Deformation: Mechanical Behavior and Deformation Substructures Induced,” *Annu. Rev. Mater. Res.*, vol. 42, no. 1, pp. 285–303, 2012, doi: 10.1146/annurev-matsci-070511-155034.

[83] S. R. Chen and G. T. Gray, “Constitutive behavior of tantalum and tantalum-tungsten alloys,” *Metall. Mater. Trans. A Phys. Metall. Mater. Sci.*, vol. 27 A, no. 10, pp. 2994–3006, 1996, doi: 10.1007/BF02663849.

[84] R. Yu, T. Cheng-wen, Z. Jing, and W. Fu-chi, “Dynamic fracture of Ti-6Al-4V alloy in Taylor impact test,” *Trans. Nonferrous Met. Soc. China*, vol. 21, no. 2, pp. 223–235, 2010, doi: 10.1016/S1003-6326(11)60703-6.

[85] Q. Zhao, G. Wu, and W. Sha, “Deformation of titanium alloy Ti – 6Al – 4V under dynamic compression,” *Comput. Mater. Sci.*, vol. 50, no. 2, pp. 516–526, 2010, doi: 10.1016/j.commatsci.2010.09.014.

[86] T. Sourmail and H. K. D. H. Bhadeshia, “Stainless Steels,” 1991. .

[87] W. Lee and C. Chiu, “Deformation and Fracture Behavior of 316L Sintered Stainless Steel under Various Strain Rate and Relative Sintered Density Conditions,” *Metall. Mater. Trans.*, vol. 37A, pp. 2006–3685, 2005, doi: 10.1007/s11661-006-1062-2.

[88] T. J. Kneen, C. Barrett, and B. P. Conner, “Mechanical behaviour and high strain rate deformation of stainless steel 316L processed by selective laser melting Mechanical behaviour and high strain rate deformation of stainless steel 316L processed by selective laser melting,” *Int. J. Rapid Manuf.*, vol. 9, p. 21, 2020, doi: 10.1504/IJRAPIDM.2020.10026158.

[89] D. Wedberg and L. Lindgren, “Mechanics of Materials Modelling flow stress of AISI 316L at high strain rates,” *Int. J. Mech. Mater.*, vol. 91, pp. 194–207, 2015, doi: 10.1016/j.mechmat.2015.07.005.

[90] J. Kluczynski, L. Sniezek, K. Grzelak, J. Janiszewski, and P. Płatek, “Influence of Selective Laser Melting Technological Parameters on the Mechanical Properties of Additively Manufactured Elements Using 316L Austenitic steel,” *Materials (Basel).*, vol. 13, p. 19, 2020, doi: 10.3390/ma13061449.

[91] W. Lee and C. Lin, “Plastic deformation and fracture behaviour of Ti – 6Al – 4V alloy loaded with high strain rate under various temperatures,” *Mater. Sci. Eng.*, vol. 241, pp. 48–59, 1998, doi: S0921-5093(97)00471-1.

[92] N. Biswas, J. L. Ding, V. K. Balla, D. P. Field, and A. Bandyopadhyay, “Deformation and fracture behavior of laser processed dense and porous Ti6Al4V alloy under static and dynamic loading,” *Mater. Sci. Eng. A*, vol. 549, pp. 213–221, 2012, doi: 10.1016/j.msea.2012.04.036.

[93] R. Fadida and D. Rittel, “Dynamic Mechanical Behavior of Additively Manufactured Ti6Al4V With Controlled Voids,” *J. Appl. Mech.*, vol. 82, p. 9, 2015, doi: 10.1115/1.4029745.

[94] A. M. S. H. Masood and D. F. M. Jahedi, “Dynamic compressive behaviour of Ti-6Al-4V alloy processed by electron beam melting under high strain rate loading,” *Adv. Manuf.*, vol. 3, no. 3, pp. 232–243, 2015, doi: 10.1007/s40436-015-0119-0.

[95] A. Mostafa, D. Shahriari, I. P. Rubio, V. Brailovski, and M. Jahazi, “Hot compression behavior and microstructure of selectively laser-melted IN718 alloy,” *Int. J. Adv. Manuf. Technol.*, vol. 96, pp. 371–385, 2018, doi: 10.1007/s00170-017-1522-4.

[96] Q. Xue and G. T. Gray, “Development of Adiabatic Shear Bands in Annealed 316L Stainless Steel : Part I . Correlation between Evolving Microstructure and Mechanical Behavior,” *Metall. Mater. Trans.*, vol. 37, p. 2006—2435, 2005, doi: 10.1007/BF02586218.

[97] M. A. (university of C. Meyers and K. K. (University of A. Chawla, *Mechanical behaviour of materials*. 1994.

[98] A. A. Tiamiyu, A. G. Odeshi, and J. A. Szpunar, “Materials Science & Engineering A Multiple strengthening sources and adiabatic shear banding during high strain-rate deformation of AISI 321 austenitic stainless steel : E ff ects of grain size and strain rate,” *Mater. Sci. Eng. A*, vol. 711, pp. 233–249, 2018, doi: 10.1016/j.msea.2017.11.045.

[99] S. Boakye-yiadom and M. N. Bassim, “Effect of prior heat treatment on the dynamic impact behavior of 4340 steel and formation of adiabatic shear bands,” *Mater. Sci. Eng. A*, vol. 528, pp. 8700–8708, 2011, doi: 10.1016/j.msea.2011.08.036.

[100] C. Zenner and J. H. Hollomon, “Effect of Strain Rate Upon Plastic Flow of Steel Contributed Original Research,” *J. Appl. Phys.*, vol. 22, p. 12, 2004, doi: 10.1063/1.1707363.

[101] A. Eliasu, “Effect of laser powder bed fusion parameters on the microstructural evolution and hardness of 316L stainless steel,” *Int. J. Adv. Manuf. Technol.*, vol. 113, pp. 2651–2669, 2021, doi: 10.1007/s00170-021-06818-9.

[102] J. P. Oliveira, A. D. Lalonde, and J. Ma, “Processing parameters in laser powder bed fusion metal additive manufacturing,” *Mater. Des.*, vol. 193, pp. 1–12, 2020, doi: 10.1016/j.matdes.2020.108762.

[103] R. Li, J. Liu, Y. Shi, M. Du, and Z. Xie, “316L Stainless Steel with Gradient Porosity Fabricated by Selective Laser Melting,” *Mater. Eng. Perform.*, vol. 19, pp. 666–671, 2010, doi: 10.1007/s11665-009-9535-2.

[104] N. T. Aboulkhair, N. M. Everitt, I. Ashcroft, and C. Tuck, “Reducing porosity in AlSi10Mg parts processed by selective laser melting ☆,” *Addit. Manuf.*, vol. 1–4, pp. 77–86, 2014, doi: 10.1016/j.addma.2014.08.001.

[105] H. Gong, K. Rafi, H. Gu, T. Starr, and B. Stucker, “Analysis of defect generation in Ti – 6Al – 4V parts made using powder bed fusion additive manufacturing processes ☆,” *Addit. Manuf.*, vol. 1–4, pp. 87–98, 2014, doi: 10.1016/j.addma.2014.08.002.

[106] K. Darvish, Z. W. Chen, and T. Pasang, “Reducing lack of fusion during selective laser melting of CoCrMo alloy : Effect of laser power on geometrical features of tracks,” *JMADE*, vol. 112, pp. 357–366, 2016, doi: 10.1016/j.matdes.2016.09.086.

[107] J. Riedelbauch, D. Rietzel, and G. Witt, “Analysis of material aging and the influence on the mechanical properties of,” *Addit. Manuf.*, vol. 27, pp. 259–266, 2019, doi: 10.1016/j.addma.2019.03.002.

[108] P. Ferro, R. Meneghello, G. Savio, and F. Berto, “A modified volumetric energy density – based

approach for porosity assessment in additive manufacturing process design," *Int. J. Adv. Manuf. Technol.*, vol. 110, pp. 1911–1921, 2020, doi: 10.1007/s00170-020-05949-9.

[109] K. Zhang, S. Wang, W. Liu, and X. Shang, "Characterization of stainless steel parts by Laser Metal Deposition Shaping," *J. Mater.*, vol. 55, pp. 104–119, 2014, doi: 10.1016/j.matdes.2013.09.006.

[110] M. Pavlov, M. Doubenskaia, and I. Smurov, "Pyrometric analysis of thermal processes in SLM technology," vol. 5, no. 2, pp. 523–531, 2010, doi: 10.1016/j.phpro.2010.08.080.

[111] W. S. Lee, T. H. Chen, C. F. Lin, and W. Z. Luo, "Dynamic mechanical response of biomedical 316L stainless steel as function of strain rate and temperature," *Bioinorg. Chem. Appl.*, vol. 2011, p. 13, 2011, doi: 10.1155/2011/173782.

[112] R. F. Waymel, H. B. Chew, and J. Lambros, "Loading Orientation Effects on the Strength Anisotropy of Additively-Manufactured Ti-6Al-4V Alloys under Dynamic Compression," *Exp. Mech.*, vol. 59, pp. 829–841, 2019, doi: 10.1007/s11340-019-00506-2.

[113] X. Feaugas and H. Haddou, "Grain-size effects on tensile behavior of nickel and AISI 316L stainless steel," *Metall. Mater. Trans. A*, vol. 34, no. 10, pp. 2329–2340, 2003, doi: 10.1007/s11661-003-0296-5.